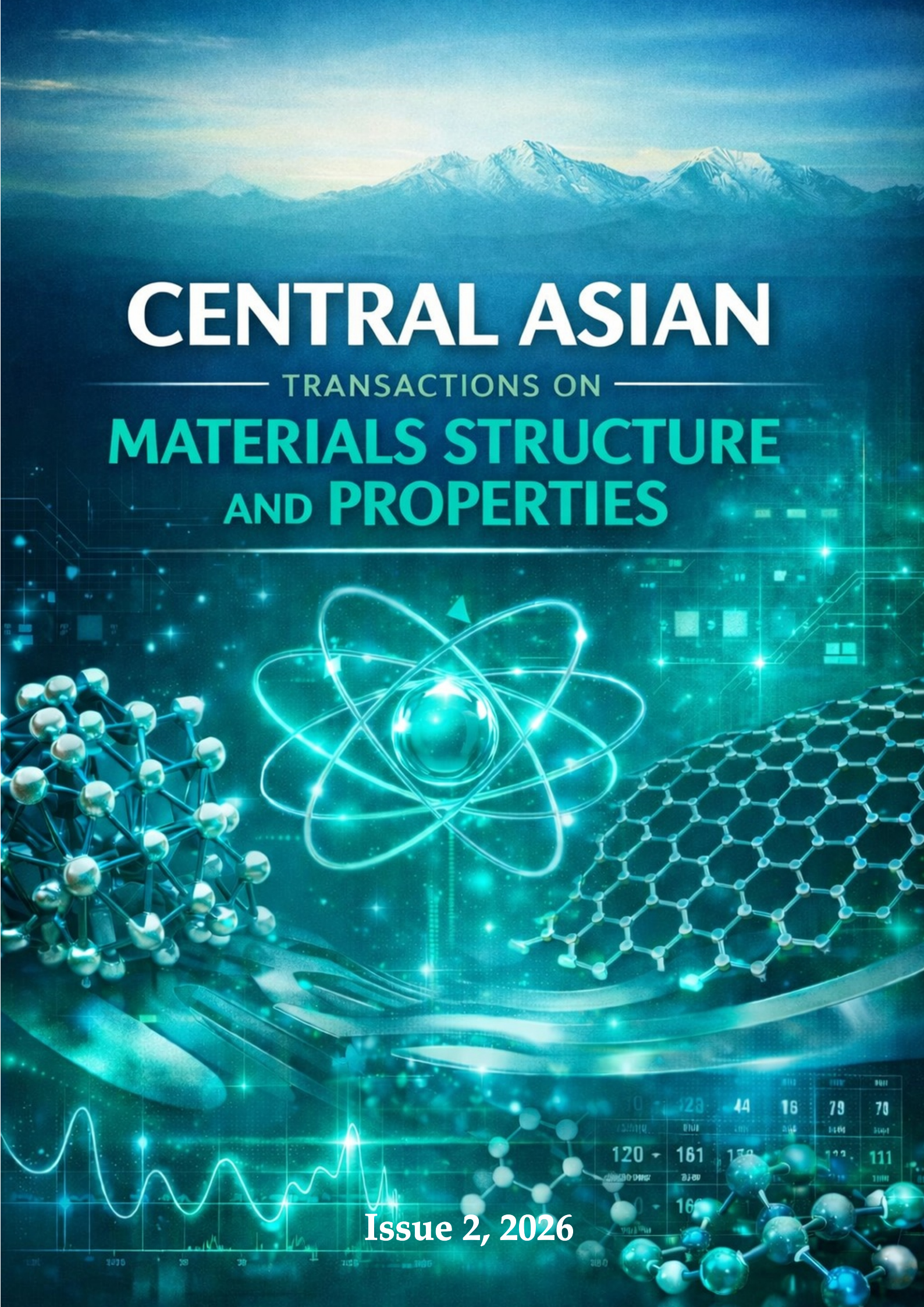
CENTRAL ASIAN
TRANSACTIONS ON
MATERIALS STRUCTURE
AND PROPERTIES
Issue 2, 2026

ISSN (Print): 3134-7983
ISSN (Online): 3134-7991 Vol. 1, Issue 2, June 2026.

CENTRAL ASIAN TRANSACTIONS ON MATERIALS STRUCTURE AND PROPERTIES

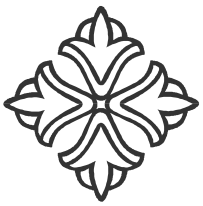

Published 4 times a year

Ust-Kamenogorsk, 2026

Vol. 1, Issue 2, June 2026.

CENTRAL ASIAN TRANSACTIONS ON MATERIALS STRUCTURE AND PROPERTIES

https://doi.org/10.51885/3134-7983_CATMSP_2026_2_1
SRSTI 53.49.01

STRUCTURE FORMATION PROCESSES IN THE PRODUCTION OF A LAMINATED STEEL-COPPER-BRASS COMPOSITE BY EXPLOSION WELDING

Riza Abylkalikova[1], Lyudmila Kveglis[1], Dametyk Kurmanova[2], Zukhra Espolova[2]*, Zhuldyz Uazyrhanova[2], Gulmira Baizakova[2]

[1]S. Amanzholov East Kazakhstan University, Ust-Kamenogorsk, Republic of Kazakhstan
[2]D. Serikbaev East Kazakhstan Technical University, Ust-Kamenogorsk, Republic of Kazakhstan
*Corresponding-author Espolova Zuhra Ablkasymovna, e-mail: ZEspolova@edu.ektu.kz

Keywords:
Explosive welding, laminated composite, steel-copper-brass, nonequilibrium phase, abnormally rapid mass transfer

ABSTRACT

A layered composite material consisting of 20-grade steel, M1 copper, and L80 brass produced by explosive welding was studied. Under explosive welding conditions, complex mechanochemical transformations occur within the contact region of the multilayer composite material, resulting in the formation of phases that are absent in the equilibrium state of the original constituents. In particular, the emergence of the Cu_5Zn_8 intermetallic phase and metastable γ-iron has been identified. The development of this microstructure is associated with high-rate interdiffusion processes, including the penetration of copper into iron and the migration of zinc from the brass layer into copper. The evolution of these phenomena is governed by the wave-like dynamics of material interaction in the welded interface zone. The microhardness of the layers of the resulting composite material was also studied.

INTRODUCTION

The study of structural transformations of nonequilibrium excited states in metals and alloys is a key problem in condensed matter physics, the scope of which is constantly evolving as experimental techniques and theoretical concepts develop.

The processes of structural self-organization during phase transformations in metals were first described in the works of D.K. Chernov. The formation of structural states arising in deformation localization zones in metallic alloys has been extensively studied.

According to Prigogine, new nonequilibrium structures are created in a system of excited atoms with decreasing entropy. An arbitrary nonequilibrium system tends toward a local equilibrium state at extreme speed (with maximum entropy production). Experimental data show that technological processes generally occur under conditions significantly removed from equilibrium. Consequently, minor changes in the system's parameters can lead to significant changes in its physical and mechanical properties.

One area of practical application that utilizes fast processes in metal alloys is the creation of materials with high strength, ductility, impact toughness, wear resistance, and other properties. Understanding the structural formation patterns of such materials allows us to predict their new properties.

Under conditions of structural instability, as well as in internal stress fields created by plastic deformation, nanostructured formations can arise, the properties of which determine the macroscopic properties of the material. Therefore, new experimental studies are needed to identify and explain the general patterns and nature of structural and phase transformations in such materials for the subsequent use of their unique properties in engineering and industry.

Investigations into the properties of composite materials and the physicochemical phenomena associated with explosive welding contribute to the development of materials exhibiting unique performance characteristics, thereby creating new opportunities for addressing contemporary engineering challenges. Metal matrix composites (MMCs) composed of dissimilar metals with limited mutual solubility are of particular interest due to their ability to combine the advantageous properties of individual constituents within a single material system. As a result, such composites demonstrate significant potential for a wide range of applications. For instance, copper-based composites reinforced with refractory metals are characterized by high mechanical strength and excellent thermal stability. Previous studies have shown that increasing the volume fraction of the refractory phase leads to enhanced hardness in copper–molybdenum composites. These advanced materials are therefore considered promising candidates for applications such as the manufacture of resistance welding electrodes and other high-performance electrical components.

The cluster modeling approach is based on representing each structural state as a combination of elementary crystalline clusters. Cluster aggregates are formed by the assembly of these elementary clusters, which may consist of simple atomic configurations, such as octahedra and tetrahedra, or more complex structural units. The fundamental concept of the method is that polymorphic transformations are described not in terms of the relative displacement of atomic planes, but rather as a reconstruction of three-dimensional coordination polyhedra that constitute the crystal structures of the phases involved in the phase transformation.

Structures composed entirely of tetrahedra exhibit an exceptionally high packing efficiency, reaching approximately 89%, which is significantly greater than that of the closest-packed crystalline arrangements, namely face-centered cubic (FCC) and hexagonal close-packed (HCP) lattices, whose packing density is about 74%. The presence of such structural units in liquid or amorphous metals may account for their relatively high atomic packing density, typically ranging from 71% to 73% in amorphous alloys, whereas the calculated density of random close packing does not exceed 64–66%. Since the packing density of amorphous alloys containing icosahedral phases is somewhat lower than that of densely packed FCC, HCP, and body-centered cubic (BCC) structures, these materials can be regarded as having a comparatively more open atomic arrangement. A systematic analysis of icosahedral configurations in metallic systems was first presented by Frank and Kasper, who demonstrated the feasibility of their formation and identified four principal cluster types, including the simple icosahedron. To date, numerous structures classified as tetrahedrally close-packed phases have been reported, particularly in structurally unstable states associated with plastic deformation. Furthermore, several studies have shown that icosahedral phases can be produced through mechanochemical processing. Our investigations have likewise revealed the formation of tetrahedrally close-packed structures during plastic deformation in nickel–titanium alloys, Hadfield steel, and cast iron.

Solid-state phase transformations induced by plastic deformation have become a subject of considerable research interest in recent years. Under mechanical loading, mechanochemical reaction products may form at the interfaces between dissimilar metals. The exceptionally high rates of physicochemical transformations observed in such systems are associated with the propagation of plastic deformation waves, which act as carriers of both energy and mass. Under conventional static conditions, the formation of new phases typically requires relatively long periods of time, ranging from seconds and minutes to hours or even longer. In contrast, when

transformations occur within plastic deformation waves, they can be completed within extremely short time intervals on the order of 10^{-5}–10^{-7} s. The resulting phase particles may reach sizes of several tenths of a millimeter or larger. Moreover, the newly formed phases are generally characterized by a nonequilibrium nature.

Nonlinear mass-transfer waves propagate through a relay-like mechanism in which atoms are successively transferred from regular lattice sites to bifurcation sites. Each bifurcation site, in turn, displaces an atom from the neighboring lattice position into the nearest bifurcation interstitial state, thereby enabling the continued propagation of mass transport through the crystal structure. This mechanism differs fundamentally from conventional diffusion. In diffusion processes, the same atoms migrate along the entire transport path through regular lattice sites, without the involvement of intermediate bifurcation states. Consequently, nonlinear wave-driven mass transfer represents a distinct transport mode characterized by the participation of transient bifurcation configurations that are absent in classical diffusion mechanisms. One elementary act in a nonlinear wave consists of an atom transitioning from a main site to an interstitial bifurcation state and pushing the next atom from its main site to the nearest interstitial bifurcation state. This relay-type mass transport mechanism is characterized by an anomalously high propagation rate compared with conventional diffusion processes. Owing to the successive transfer of atomic displacements rather than the long-range migration of individual atoms, mass transport can occur over extremely short timescales and with significantly greater efficiency than diffusion-driven atomic motion.

In a crystal containing a substitutional solid solution, impurity atoms subjected to a nonuniform mechanical stress field experience a driving force proportional to the local stress gradient. As a result, stress-induced atomic migration may occur, contributing to enhanced mass transfer and promoting structural and phase transformations within the material:

$$f_v = \Omega_0 \nabla P \quad f_i = -\Omega_0 \nabla P \tag{1}$$

Ω_0 - volume of a point defect;

∇P - local pressure change.

The flux density of the substance J creates a concentration gradient and leads to the stratification of the alloy, as occurs with ascending diffusion:

$$J = D \nabla C \tag{2}$$

D- mass transfer coefficient, similar to the diffusion coefficient.

Estimates based on the proposed model indicate that this mode of atomic displacement proceeds at an average velocity of approximately 4.5×103 m/s. The model provides a framework for explaining the phenomena of anomalously rapid mass transport and ion segregation observed in metallic alloys subjected to plastic deformation. Furthermore, it offers insight into the underlying mechanisms responsible for the accelerated redistribution of chemical species under nonequilibrium deformation conditions.

Layered composite materials are currently attracting significant attention because they offer the possibility of achieving unique combinations of mechanical and physical properties. Composites incorporating copper- and steel-based layers are particularly valuable for the manufacture of components used in electrothermal systems, heat-exchange equipment, and other engineering applications. However, producing composites from materials with limited weldability remains a considerable technological challenge (Vainerman & Pichuzhkin, 2002). These difficulties can be overcome through the application of high-energy material-processing techniques, such as explosive welding (Kveglis et al., 2016). Nevertheless, the physicochemical processes occurring at the interface of dissimilar materials during explosive welding have not yet been fully understood and continue to be the subject of ongoing investigation (Mashimo & Huang, 1999; Kan, Son & Hon, 2017). The ability of plastic deformation waves to propagate both

through grain interiors and along grain boundaries, as well as across the interfaces of dissimilar metals, may contribute to the enhancement of the mechanical properties of composite materials (Deribas, 1980). The mechanisms and characteristics of plastic deformation wave propagation have been extensively analyzed in the works of V. E. Panin, who demonstrated their important role in the evolution of material structure and deformation behavior under nonequilibrium loading conditions (Panin, Egorushkin & Panin, 2012; Panin & Egorushkin, 2013).

The objective of the present work was to investigate the structural features of deformation localization regions in a steel 20–M1 copper–L80 brass multilayer composite produced by explosive welding.

The study focused on the analysis of microstructural evolution, phase and chemical composition, and microhardness variations throughout the cross-section of the multilayer material, with the aim of elucidating the relationships among these characteristics.

MATERIALS AND METHODS

The initial materials used for the fabrication of the layered composite were plates of 20 steel, M1 copper, and L80 brass with thicknesses of 18 mm, 6 mm, and 4 mm, respectively. Ammonite 6ZhV was employed as the explosive material. During the welding process, the copper and brass plates were bonded to a horizontally positioned steel plate using an angular explosive welding configuration. This arrangement enabled the formation of a multilayer steel–copper–brass composite through high-velocity impact and subsequent metallurgical bonding at the interfaces between the dissimilar materials (Mali & Teslenko, 2002; Mali et al., 2017). The impact angle was $\gamma = 6°$. The estimated velocity of explosive welding is Vk = 2500 m/s (contact velocity) and V_s = 260 m/s (impact velocity).

After fabrication of the layered composite specimens, metallographic, X-ray diffraction, and electron microprobe analyses were performed to characterize their microstructure, phase composition, and elemental distribution. These investigations were conducted to identify the structural features and phase constituents formed within the composite during the explosive welding process.

RESULTS AND DISCUSSION

Explosive welding of brass, copper, and steel was found to produce characteristic wavy interfacial boundaries between the bonded layers (Fig. 1).

Scanning electron microscopy (SEM) combined with microanalytical investigations revealed the formation of concentration-transition zones at the interfaces. Localized fluctuations in zinc concentration were detected in regions adjacent to the brass–copper interface, indicating the occurrence of intensive elemental redistribution during the welding process. These concentration gradients suggest enhanced mass transport and interfacial mixing under the extreme conditions generated by explosive welding.

Periodic row-like structures elongated in a direction perpendicular to the deformation axis were observed within the brass layer (Fig. 1,b). These features may be associated with the formation of newly developed phases. As demonstrated below by X-ray diffraction analysis, a nonequilibrium γ-brass phase enriched in zinc was detected in the L80 alloy despite being absent from its equilibrium phase composition. This observation suggests that plastic deformation was accompanied by anomalously rapid mass transport of copper from the brass layer toward the adjacent copper layer of the composite.

The spatial distribution of structural heterogeneities in the brass region directly adjacent to the copper layer indicates that mass transport occurred in a wave-like manner. This process manifested itself through the formation of successive transverse rows of structural features regularly arranged along the transition zone. Notably, the spacing between these structures

decreases with decreasing distance to the copper–brass interface. Such behavior is consistent with the concept of wave-driven mass transfer and supports the existence of localized deformation waves governing material redistribution in the interfacial region (Panin & Egorushkin, 2013).

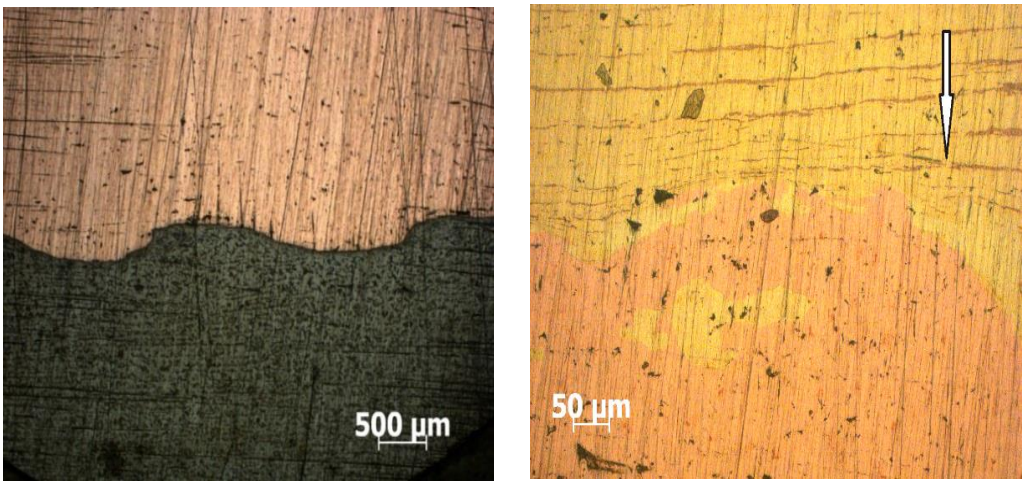

a *b*

Figure 1. Microstructure of the contact zones of the composite material:
a – steel 20 – copper M1; b – copper M1 – brass L80
Note – compiled by the authors based on the authors' experimental data.

The observed string-like structure appears to be a product of self-organization processes occurring during the propagation of shock waves. In irreversible systems, self-organization manifests through the spontaneous formation of ordered structures when the system reaches critical conditions. At these critical parameters, the initially stable state becomes structurally unstable, leading to the emergence of bifurcations and the development of new structural configurations. Under the extreme nonequilibrium conditions generated by shock-wave loading, such bifurcation phenomena can promote the formation of periodically arranged string-like structures and other dissipative patterns within the material (see arrow in Fig. 1, b) (Mali & Teslenko, 2002).

The observed string-like structure is likely a consequence of self-organization processes occurring during shock-wave propagation. In nonequilibrium systems, self-organization is manifested through the spontaneous emergence of ordered patterns when critical conditions are reached. At these critical thresholds, the initially stable state loses its stability, giving rise to bifurcation phenomena and the formation of new structural configurations. Under the extreme nonequilibrium conditions associated with shock-wave loading, such bifurcation processes may facilitate the development of periodically arranged string-like structures and other dissipative patterns within the material. These features can be regarded as manifestations of the system's tendency toward structural ordering during its evolution far from thermodynamic equilibrium.

During X-ray diffraction measurements, the incident beam was initially focused on the steel–copper interface and, after acquisition of the diffraction pattern, was subsequently shifted to the copper–brass interface region (Fig. 2). The presence of peaks corresponding to a zinc-containing phase in the diffraction pattern obtained from the steel–copper interaction zone may be attributed to limited accuracy in beam positioning, resulting in partial overlap with the adjacent copper–brass interface.

The occurrence of a nonequilibrium iron phase with a face-centered cubic (FCC) crystal structure in the copper–steel contact region has also been reported in previous studies involving severe joint plastic deformation of these metals (Kveglis et al., 2016). The stabilization of this

phase under ambient pressure and room-temperature conditions is believed to result from the partial dissolution of copper in iron, which alters the phase stability and promotes the retention of the FCC structure.

A notable finding of the present study is the detection of the nonequilibrium Cu_5Zn_8 phase (γ-phase) (Fig. 2). According to the Cu–Zn phase diagram, L80 brass is expected to contain only the α-phase under equilibrium conditions. However, following explosive welding, the γ-phase—typically characteristic of brasses with a substantially higher zinc content—was also identified. The appearance of this phase as a result of intense plastic deformation provides evidence for anomalously rapid mass transport of alloying elements during the explosive welding process. The formation of the Cu_5Zn_8 phase indicates that local compositional redistribution occurred under highly nonequilibrium conditions, leading to the stabilization of phase constituents that would not be expected in the initial alloy system under equilibrium thermodynamic conditions.

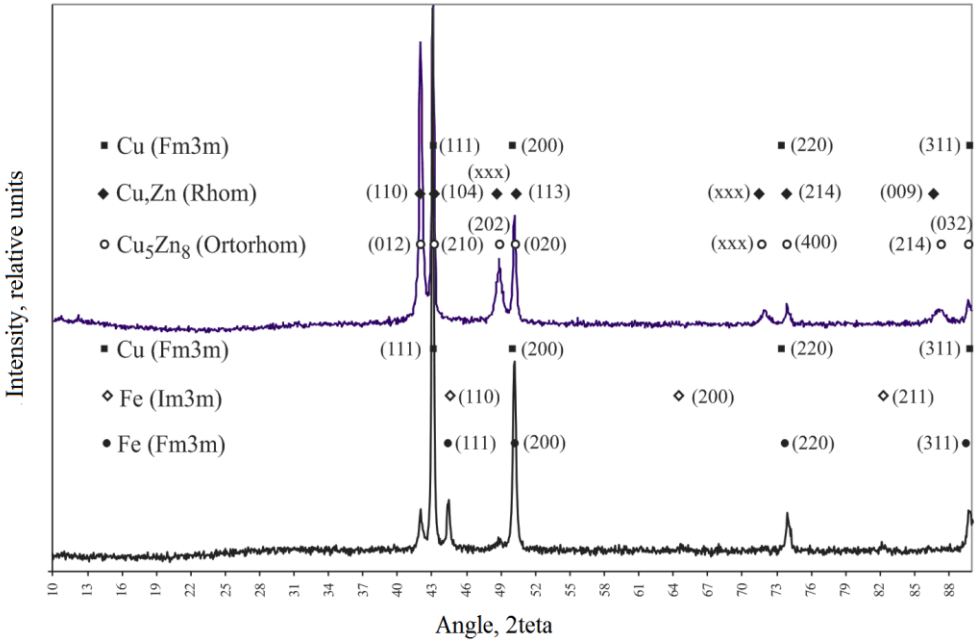

Figure 2. X-ray diffraction spectra recorded from the steel–copper contact zone (bottom) and the copper–brass contact zone (top).

Note – compiled by the authors based on the authors' experimental data.

The anomalous mass transport observed in the present experiments can be explained by the formation of interstitial bifurcation structural states generated during plastic deformation (Panin & Egorushkin, 2015). Distortion of the crystal lattice under deformation leads to the creation of excess free volume and to a redistribution of the electron density within localized regions of the material. These nonequilibrium conditions facilitate the formation of metastable phases that are not expected under equilibrium thermodynamic conditions. In particular, plastic deformation may promote the formation of the Hume–Rothery electronic phase Cu_5Zn_8, which is characterized by increased hardness. The appearance of this phase provides additional evidence for the significant structural and compositional rearrangements occurring during explosive welding and supports the proposed mechanism of deformation-induced anomalous mass transport (Safari, Khosroshahi & Zolriasatein, 2017; Degtyareva, 2005).

A PMT-3M microhardness tester (Fig. 3) was used to study the microhardness of the original sample. Microhardness measurements were performed using a Vickers diamond indenter. Indentations were made across the entire cross-section of the specimen at intervals of

100 μm under a load of 20 g, beginning in the brass layer and extending through the copper layer to the steel substrate.

As shown in Fig. 3, copper exhibited the lowest microhardness among the three constituent materials. Following explosive welding, its hardness remained nearly unchanged, and X-ray phase analysis did not reveal the formation of any new phases within the copper layer. This observation suggests that strengthening mechanisms unrelated to phase transformations, including deformation-induced relaxation processes, contributed only marginally to the hardening of this region. In contrast, the average hardness of the steel layer increased by approximately 27% relative to its undeformed state. The abrupt fluctuations observed in the microhardness profile may be attributed to the indenter penetrating locally harder microstructural constituents. In 20 steel, such regions are likely associated with cementite-containing areas. The overall increase in the average microhardness of the steel section may be explained by the formation of localized microvolumes possessing an austenitic structure within the matrix. Considering the observed changes in phase composition, it can be concluded that explosive deformation has a pronounced effect on the microstructural evolution and mechanical properties of the composite constituents. The formation of nonequilibrium phases and associated structural transformations plays a significant role in the strengthening behavior of the multilayer steel–copper–brass composite.

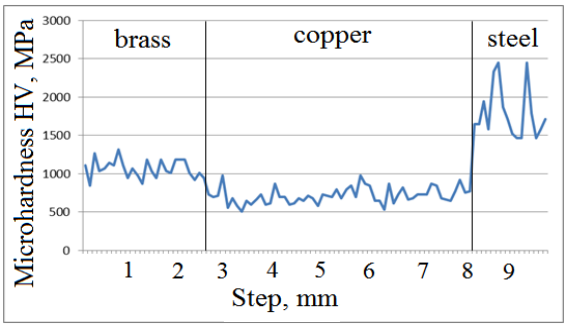

Figure 3. Variation of microhardness across the cross-section of the L80 brass–M1 copper–20 steel multilayer composite

Note – compiled by the authors based on the authors' experimental data.

According to Gilman (Gilman, 2003), the general mechanism of mechanochemical reactions can be interpreted within the framework of molecular orbital theory. Mechanical deformation increases the energy of bonding orbitals while simultaneously lowering the energy of antibonding orbitals. As a result, the energy gap between these states decreases, leading to destabilization of the atomic bonding system. When this energy gap approaches zero, bonding electrons become delocalized because occupation of antibonding states no longer requires additional energy. Under such conditions, the activation energy of a chemical reaction may effectively vanish. However, the nature of the reaction products is determined not only by the activation energy but also by geometric factors. These factors are governed by interatomic distances and the spatial orientation of chemical bonds, including the angles between bond directions. Consequently, the structural outcome of a mechanochemical transformation depends on both the energetic state of the system and the geometrical arrangement of atoms during deformation.

> It is now well established (Boldyrev, 2002) that a characteristic feature of solid-state reaction mechanisms is the increase in crystal lattice energy associated with the generation of excess free volume. Mechanical alloying has been shown to promote the redistribution and enhancement of electron density between atoms of the constituent elements, thereby increasing

their chemical reactivity. A similar mechanism, proposed by (Guzev & Dmitriev, 2013), is closely related to the development of crystal lattice curvature during plastic deformation. Such lattice distortions create nonequilibrium structural states that facilitate atomic rearrangement, enhance mass transport processes, and promote the formation of new phases under deformation-induced conditions.

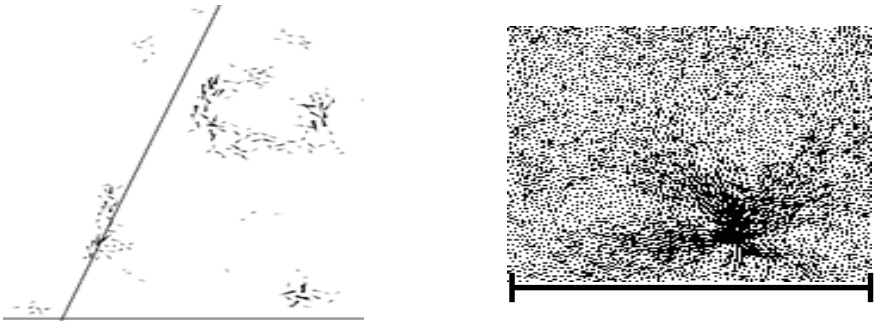

a **b**

Figure 4. The "spindle" model

Note – compiled by the authors based on the authors' experimental data.

Figure 4 illustrates the stress field distribution obtained from molecular dynamics calculations. (Langer & Lemaitre, 2004).

a) The line indicates the direction of the applied load axis and the displacement of atoms around this axis,

b) Schematic representation of the elastic stress field distribution obtained by molecular dynamics simulation (Langer & Lemaitre, 2004).

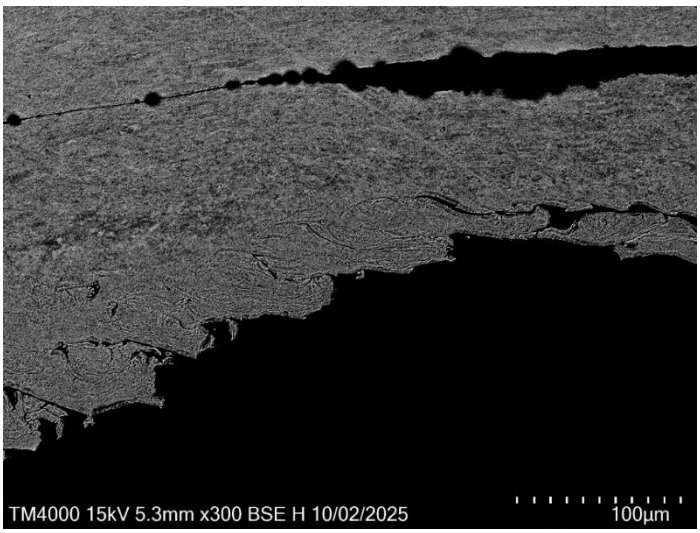

Figure 5. Electron microscopic image of a fragment of the flaring zone of a copper sample subjected to impact loading during explosion welding; a dark track and a cavity formed by the shock wave are visible

Note – compiled by the authors based on the authors' experimental data

Figure 5 shows an electron microscopic image of a fragment of the flaring zone of a copper sample subjected to impact loading during explosion welding; a dark track and a cavity formed by the shock wave are visible.

In addition to the large cavity, small round cavities located at different distances from each other are visible along the track. Under explosive welding conditions, high pressure develops in localized areas. Evolution of the structural and phase states of a condensed medium subjected to external mechanical loading. In Fig. 6, labels 1 and 1′ indicate gas-filled pores, whereas 2 and 2′ correspond to liquid-filled pores. T_3 denotes the triple equilibrium point of the solid sol, liquid (L), and gaseous phases, and $T_{(C)}$ is the critical temperature.

In Figure 5, the edge shape of the samples subjected to explosive deformation has the appearance of a fractal structure or viscous fingers. Figure 7 shows the calculated pattern of the chaotic growth of "viscous fingers" in Hele-Shaw cells as a function of time from top to bottom and left to right. The width of the "viscous fingers" is along the x-axis, and the length along the y-axis.

Figure 8 shows a Hele-Shaw experiment illustrating the formation and evolution of the hydrodynamic structure (Mironova, 2008).

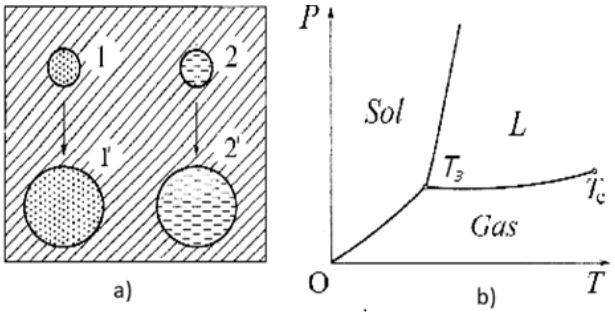

Figure 6. Evolution of structural and phase states in a condensed medium subjected to external mechanical loading: a – correlation between the development of continuity defects and transformations of the material's aggregate state; b – equilibrium phase diagram of the material under compressive stress conditions.

Note – compiled by the authors based on the authors' experimental data

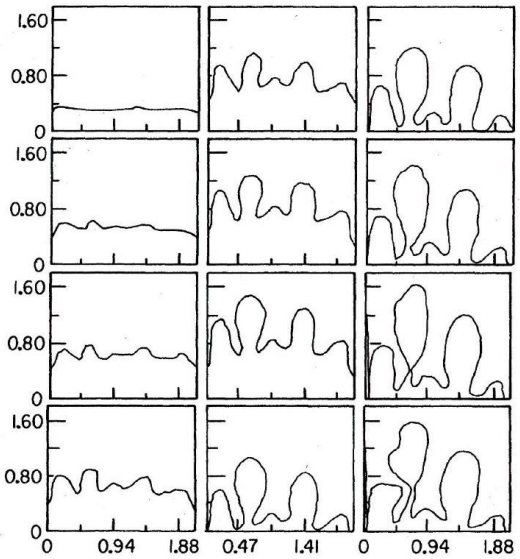

Figure 7. Pattern of chaotic growth of "viscous fingers" in Hele-Shau cells depending on time from top to bottom and from left to right. Along the x-axis is the width, along the y-axis is the length of the "viscous fingers", expressed in inches (Mironova, 2008).

Note – compiled by the authors based on the authors' experimental data.

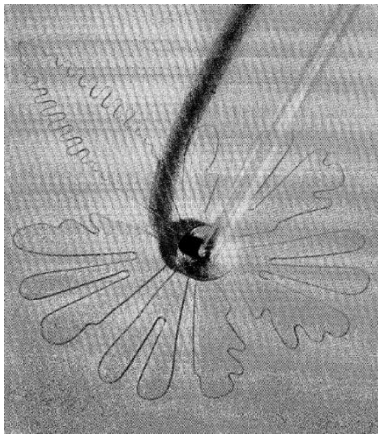

Figure 8. Hele-Shaw experiment illustrating the formation and evolution of a hydrodynamic structure (Mironova, 2008).
Note – compiled by the authors based on the authors' experimental data.

DISCUSSION OF RESULTS

The effect of displacement of atoms in solids over macroscopic distances in an extremely short time is well known, if we compare this phenomenon with diffusion (Noskov, 2018). It was called anomalous mass transfer due to the ultra-high migration rates of atoms, sometimes exceeding the mobility in liquid metals. It has been established that this effect can occur under various types of external loading, including both elastic and plastic deformation. Under conditions of nonlinear plastic deformation, particularly when deformation becomes localized within specific regions of a specimen, the resulting nonequilibrium state provides the necessary thermodynamic driving force for accelerated mass transport (Boldyrev, 2006). In deformation-induced mass transfer processes, a key role is played by the curvature of the crystal lattice and the emergence of new admissible structural states. These deformation-generated configurations facilitate atomic redistribution and contribute to the enhanced mobility of matter observed under intense mechanical loading conditions (Noskov, 2018).

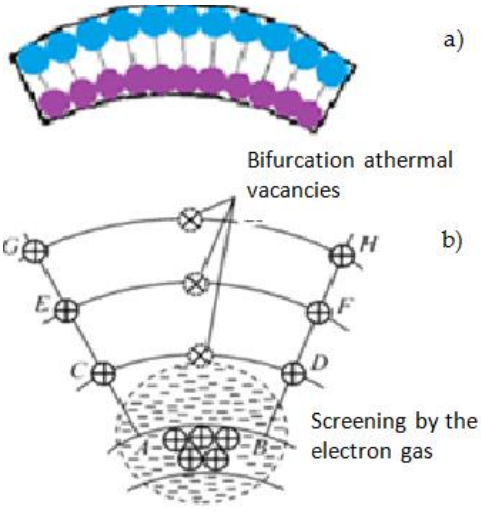

Figure 9. Schematic illustration of metastable bifurcation structural states (MBSS) in locally curved crystal lattices: a – lattice curvature generated by external mechanical loading at the interface of dissimilar metals; b – formation of interstitial bifurcation vacancy states within regions of lattice curvature, promoting increased atomic solubility and mass transport
Note – compiled by the authors based on the authors' experimental data

The mutual penetration of dissimilar atoms can lead both to changes in deformation behavior, known as the Rebinder effect, and to the initiation of chemical reactions followed by the formation of reaction products and new phases (Panin & Egorushkin, 2015).

Unlike conventional diffusion, which is driven primarily by concentration gradients, this transport mechanism is commonly referred to as deformation-induced atomic mixing or ballistic diffusion. In such processes, atomic redistribution is governed by intense mechanical deformation and the generation of nonequilibrium structural states rather than by thermally activated diffusion alone. Despite extensive research, there is still no universally accepted explanation of the underlying mechanism responsible for deformation-induced atomic mixing. Various models have been proposed, emphasizing the roles of lattice defects, localized plastic flow, crystal lattice curvature, and nonequilibrium atomic configurations in facilitating the accelerated transport of atoms under severe deformation conditions (Panin & Egorushkin, 2015).

According to the model proposed by (Panin & Egorushkin, 2015), the application of an external load to the interface between two dissimilar materials results in the modulation of normal and shear stresses, producing alternating regions of tension and compression (Fig. 9). This stress modulation generates zones of crystal lattice curvature at the interface, where regions with increased and decreased interatomic spacings become coupled.

Anomalous mass transport may be facilitated by interstitial bifurcation structural states (IBSS), which can be regarded as athermal vacancy-like defects formed within regions of localized crystal lattice curvature. The IBSS concept was introduced by (Panin & Egorushkin, 2015) to explain accelerated atomic transport under deformation conditions. Mechanical stresses create lattice-curvature zones in which enlarged interatomic distances are coupled, leading to a redistribution of the electron density. Within these regions, increased interionic spacings give rise to athermal vacancy states that are absent in an equilibrium crystal structure. The presence of IBSS significantly enhances the mutual solubility of dissimilar metals and promotes the rapid formation of metastable phases and atomically ordered structures. As a result, structural and phase transformations that would normally require prolonged diffusion times can occur within extremely short time intervals under severe deformation conditions.

CONCLUSIONS

The occurrence of abnormally rapid mass transfer and the formation of these phases during plastic deformation is confirmed by studies conducted using optical and electron microscopes and microhardness measurements.

Under the nonequilibrium conditions associated with composite fabrication, metastable phases and solid solutions can form that are absent from the equilibrium phase diagram. Crystal lattice distortion occurs over multiple length scales: at the macroscopic level, it is manifested by the wavy morphology of the copper–molybdenum interface; at the mesoscale, by the distortion of individual grain shapes; and at the atomic-crystalline level, by the distortion of atomic planes.At the atomic scale, the high energy-density gradients generated within localized regions give rise to bifurcation structural states. These nonequilibrium states facilitate the local formation of solid solutions between components that are mutually insoluble under equilibrium conditions. They may also promote the emergence of complex atomic arrangements, including icosahedral configurations, which are characteristic of metastable structural states. The formation of such structures provides further evidence of the profound influence of severe deformation and nonequilibrium processes on phase evolution and atomic redistribution in composite materials.

1. A layered composite material consisting of 20 steel, M1 copper, and L80 brass was successfully fabricated by explosive welding. The results demonstrate that mechanochemical interactions occurring during the explosive welding process lead to the formation of reaction products in the contact regions in the form of both equilibrium and nonequilibrium phases. These

phase transformations are associated with the extreme nonequilibrium conditions generated during high-velocity impact and play a significant role in determining the structural and mechanical properties of the resulting multilayer composite.

2. Analysis of the X-ray diffraction patterns revealed the presence of both equilibrium and nonequilibrium phases in the interfacial regions. At the copper–brass interface, equilibrium phases were identified together with the nonequilibrium Cu_5Zn_8 electronic phase, which is not expected in L80 brass under equilibrium conditions. At the copper–steel interface, equilibrium copper and α-iron phases were detected, along with the nonequilibrium γ-iron phase.

3. The structural transformations observed in the contact zones of the composite layers are attributed to anomalously rapid mass transport of copper into iron and zinc from brass into copper. This process is associated with the formation of interstitial bifurcation structural states in regions of crystal lattice curvature. The observed microstructural features further indicate that the mechanochemical processes proceed in a wave-like manner.

4. The results demonstrate that the increase in microhardness induced by explosive plastic deformation is primarily associated with changes in phase composition rather than with purely deformation-related structural effects. The contribution of deformation strengthening appears to be reduced due to relaxation processes, whereas phase transformations play the dominant role in the hardening of the composite material.

CONFLICT OF INTEREST: The authors declare no conflict of interest.

FUNDING: This research received no external funding.

INSTITUTIONAL REVIEW BOARD STATEMENT: Not applicable.

INFORMED CONSENT STATEMENT: Oral informed consent was obtained from all participants prior to their involvement in the study.

DATA AVAILABILITY STATEMENT: The data supporting the findings of this technical study are available from the corresponding author upon reasonable request; alternatively.

ACKNOWLEDGEMENTS: The authors gratefully acknowledge their colleagues for their methodological assistance and insightful discussions. They also wish to thank the anonymous reviewers for their valuable comments and recommendations, which helped to improve the quality and clarity of the manuscript.

STATEMENT ON THE USE OF ARTIFICIAL INTELLIGENCE TECHNOLOGIES: The authors declare that no artificial intelligence (AI) technologies, including generative AI and large language models, were used in the preparation of this manuscript. All written content, data processing, analysis, and scientific conclusions were developed independently by the authors.

REFERENCES

Degtyareva, V., Degtyareva, O., Sakharov, M., & Przemyslaw, D. (2005). Stability of Hume-Rothery phases in Cu-Zn alloys at pressures up to 50 GPa. Journal of Physics: Condensed Matter, 17, 7955–7962. https://surl.li/lsdcyh

Gilman, J. J. (2003). Electronic basis of the strength of materials. Cambridge University Press. https://doi.org/10.1063/1.1801871

Kaloshkin, S. D., Tomilin, I. A., Andrianov, G. A., Baldokhin, U. V., & Shelekhov, E. V. (1997). Phase transformations and hyperfine interactions in mechanically alloyed Fe-Cu solid solutions. Materials Science Forum, 235–238, 565–570. https://www.scientific.net/MSF.235-238.565

Langer, J. S., & Lemaitre, A. (2004). Dynamic model of super-Arrhenius relaxation in glassy materials. arXiv: cond-mat/0411038v1. https://doi.org/10.1103/physrevlett.94.175701

Mali, V. I., Kurguzov, V. D., Esikov, M. A., Bataev, A. A., Maliutina, I. N., Bataev, I. A., & Lozhkin, V. S. (2017). Microstructure and mechanical properties of Ti/Ta/Cu/Ni alloy laminate

composite materials produced by explosive welding. The International Journal of Advanced Manufacturing Technology, 93(9–12), 4285–4294. https://link.springer.com/article/10.1007/s00170-017-0887-8

Mashimo, T., & Huang, X. S. (1999). Metastable BCC and FCC alloy bulk bodies in Fe-Cu system prepared by mechanical alloying and shock compression. Journal of Alloys and Compounds, 288, 299–305. https://doi.org/10.1016/S0925-8388(99)00108-5

Safari, F., Khosroshahi, R., & Zolriasatein, A. (2017). Wear behavior of copper matrix composites reinforced by γ-Cu5Zn8 nanoparticles. Powder Technology, 547–559. https://doi.org/10.1016/j.powtec.2017.06.032

Болдырев, В. В. (2002). Об истории развития механохимии в Сибири. Химия в интересах устойчивого развития, 10, 3–12. https://www.sibran.ru/upload/iblock/bd8/bd874ec08851b6fcaab332bf52b2c237.pdf // Boldyrev, V. V. (2002). Ob istorii razvitiya mekhanokhimii v Sibiri [On the history of the development of mechanochemistry in Siberia]. Khimiya v interesakh ustoichivogo razvitiya [Chemistry for Sustainable Development], 10, 3–12. https://www.sibran.ru/upload/iblock/bd8/bd874ec08851b6fcaab332bf52b2c237.pdf (In Russ.)

Болдырев, В. В. (2006). Механохимия и механическая активация твёрдых веществ. Успехи химии, 75(3), 203–216. https://www.uspkhim.ru/RCR1205pdf // Boldyrev, V. V. (2006). Mekhanokhimiya i mekhanicheskaya aktivatsiya tverdykh veshchestv [Mechanochemistry and mechanical activation of solids]. Uspekhi khimii [Russian Chemical Reviews], 75(3), 203–216. https://www.uspkhim.ru/RCR1205pdf (In Russ.)

Бутягин, П. Ю. (1991). Физические и химические пути релаксации упругой энергии в твердых телах. Механохимические реакции в двухкомпонентных системах. В Механохимический синтез в неорганической химии (с. 32–52). Новосибирск: Наука. https://www.uspkhim.ru/RCR3138pdf // Butyagin, P. Yu. (1991). Fizicheskie i khimicheskie puti relaksatsii uprugoi energii v tverdykh telakh. Mekhanokhimicheskie reaktsii v dvukhkomponentnykh sistemakh [Physical and chemical pathways of elastic energy relaxation in solids. Mechanochemical reactions in two-component systems]. In Mekhanokhimicheskii sintez v neorganicheskoi khimii [Mechanochemical synthesis in inorganic chemistry] (pp. 32–52). Nauka. https://www.uspkhim.ru/RCR3138pdf (In Russ.)

Вайнерман, А. Е., & Пичужкин, С. А. (2002). Сварка меди и сплавов на ее основе со сталями: обзор литературы. Вопросы материаловедения, 4(32), 52–65. https://surl.lu/yxvlin // Vainerman, A. E., & Pichuzhkin, S. A. (2002). Svarka medi i splavov na ee osnove so stalyami: obzor literatury [Welding of copper and copper-based alloys with steels: A literature review]. Voprosy materialovedeniya [Materials Science Issues], 4(32), 52–65. https://surl.lu/yxvlin (In Russ.)

Гузев, М. А., & Дмитриев, А. А. (2013). Бифуркационное поведение потенциальной энергии системы частиц. Физическая мезомеханика, 16(3), 27–33. https://cyberleninka.ru/article/n/bifurkatsionnoe-povedenie-potentsialnoy-energii-sistemy-chastits/pdf // Guzev, M. A., & Dmitriev, A. A. (2013). Bifurkatsionnoe povedenie potentsialnoi energii sistemy chastits [Bifurcation behavior of the potential energy of a particle system]. Fizicheskaya mezomekhanika [Physical Mesomechanics], 16(3), 27–33. https://cyberleninka.ru/article/n/bifurkatsionnoe-povedenie-potentsialnoy-energii-sistemy-chastits/pdf (In Russ.)

Кан, К. Т., Сон, Ч. С., & Хон, С. И. (2017). Влияние температуры процесса соединения прокаткой на прочность и удельную электропроводимость получаемого композита α-латунь/сплав Cu-1 вес. % Cr/α-латунь. Физика металлов и металловедение, 118(2), 200–208. https://dokumen.pub/9785763842258.html // Kan, K. T., Son, Ch. S., & Khon, S. I.

(2017). Vliyanie temperatury protsessa soedineniya prokatkoi na prochnost i udelnuyu elektroprovodimost poluchaemogo kompozita α-latun/splav Cu-1 ves. % Cr/α-latun [Influence of the roll-bonding process temperature on the strength and specific electrical conductivity of the α-brass/Cu-1 wt.% Cr alloy/α-brass composite]. Fizika metallov i metallovedenie [Physics of Metals and Metallography], 118(2), 200–208. https://dokumen.pub/9785763842258.html (In Russ.)

Квеглис, Л. И., Носков, Ф. М., Калитова, А. А., & Абкарян, А. А. (2016). Структурообразование в системе сталь-медь. Химия в интересах устойчивого развития, 24(2), 229–237. https://doi.org/10.15372/khur20160216 // Kveglis, L. I., Noskov, F. M., Kalitova, A. A., & Abkaryan, A. A. (2016). Strukturoobrazovanie v sisteme stal-med [Structure formation in the steel-copper system]. Khimiya v interesakh ustoichivogo razvitiya [Chemistry for Sustainable Development], 24(2), 229–237. https://doi.org/10.15372/khur20160216 (In Russ.)

Мали, В.И., & Тесленко, Т.С. (2002). Структура и свойства взрывных компактов медь-молибден. Физика горения и взрыва, 38(4), 106–111. https://www.dissercat.com/content/zakonomernosti-formirovaniya-fazovogo-sostava-i-struktury-kompozitsionnykh-materialov-i-pokr // Mali, V. I., & Teslenko, T. S. (2002). Struktura i svoistva vzryvnykh kompaktov med-molibden [Structure and properties of explosive copper-molybdenum compacts]. Fizika goreniya i vzryva [Combustion, Explosion, and Shock Waves], 38(4), 106–111. https://www.dissercat.com/content/zakonomernosti-formirovaniya-fazovogo-sostava-i-struktury-kompozitsionnykh-materialov-i-pokr (In Russ.)

Миронова, О. А. (2008). Характеристики ускоренного массопереноса при ударном сжатии металлов с кубической решеткой [Диссертация на соискание ученой степени кандидата физико-математических наук, Москва]. https://www.dissercat.com/content/-kharakteristiki-uskorennogo-massoperenosa-pri-udarnom-szhatii-metallov-s-kubicheskoi-reshetk // Mironova, O. A. (2008). Kharakteristiki uskorennogo massoperenosa pri udarnom szhatii metallov s kubicheskoi reshetkoi [Characteristics of accelerated mass transfer during shock compression of metals with a cubic lattice] [Dissertation for the degree of Candidate of Physical and Mathematical Sciences, Moscow]. https://www.dissercat.com/content/kharakteristiki-uskorennogo-massoperenosa-pri-udarnom-szhatii-metallov-s-kubicheskoi-reshetk (In Russ.)

Носков, Ф.М. (2018). Структурообразование зон локализации пластической деформации в сплавах 3d-переходных металлов как результат быстропротекающих процессов [Диссертация на соискание степени доктора технических наук, Новокузнецк]. http://www.dslib.net/kondensat/strukturoobrazovanie-zon-lokalizacii-plasticheskoj-deformacii-v-splavah-3d.html // Noskov, F.M. (2018). Strukturoobrazovanie zon lokalizatsii plasticheskoi deformatsii v splavakh 3d-perekhodnykh metallov kak rezultat bystroprotekayushchikh protsessov [Structure formation of plastic deformation localization zones in alloys of 3d transition metals as a result of fast processes] [Dissertation for the degree of Doctor of Technical Sciences, Novokuznetsk]. http://www.dslib.-net/kondensat/strukturoobrazovanie-zon-lokalizacii-plasticheskoj-deformacii-v-splavah-3d.html (In Russ.)

Панин, В.Е., & Егорушкин, В.Е. (2013). Солитоны кривизны как обобщенные волновые структурные носители пластической деформации и разрушения. Физическая мезомеханика, 16(3), 7–26. https://cyberleninka.ru/article/n/solitony-krivizny-kak-obobschennye-volnovye-strukturnye-nositeli-plasticheskoy-deformatsii-i-razrusheniya // Panin, V. E., & Egorushkin, V. E. (2013). Solitony krivizny kak obobshchennye volnovye strukturnye nositeli plasticheskoi deformatsii i razrusheniya [Curvature solitons as generalized wave structural carriers of plastic deformation and fracture]. Fizicheskaya

mezomekhanika [Physical Mesomechanics], 16(3), 7–26. https://cyberleninka.ru/-article/n/solitony-krivizny-kak-obobschennye-volnovye-strukturnye-nositeli-plasticheskoy-deformatsii-i-razrusheniya (In Russ.)

Панин, В. Е., & Егорушкин, В. Е. (2015). Основы физической мезомеханики пластической деформации и разрушения твердых тел как нелинейных иерархически организованных систем. Физическая мезомеханика, 18(5), 100–113. https://cyberleninka.ru/article/n/17177468.pdf // Panin, V. E., & Egorushkin, V. E. (2015). Osnovy fizicheskoi mezomekhaniki plasticheskoi deformatsii i razrusheniya tverdykh tel kak nelineinykh ierarkhicheski organizovannykh sistem [Fundamentals of physical mesomechanics of plastic deformation and fracture of solids as nonlinear hierarchically organized systems]. Fizicheskaya mezomekhanika [Physical Mesomechanics], 18(5), 100–113. https://cyberleninka.ru/article/n/17177468.pdf (In Russ.)

Панин, В.Е., Егорушкин, В.Е., & Панин, А.В. (2012). Нелинейные волновые процессы в деформируемом твердом теле как многоуровневой иерархически организованной системе. Успехи физических наук, 182(12), 1351–1357. https://doi.org/10.3367/-UFNr.0182.201212i.1351 // Panin, V.E., Egorushkin, V.E., & Panin, A.V. (2012). Nelineinye volnovye protsessy v deformiruemom tverdom tele kak mnogourovnevoi ierarkhicheski organizovannoi sisteme [Nonlinear wave processes in a deformable solid as a multilevel hierarchically organized system]. Uspekhi fizicheskikh nauk [Physics-Uspekhi], 182(12), 1351–1357. https://doi.org/10.3367/UFNr.0182.201212i.1351 (In Russ.)

Information about authors

Riza Abylkalykova – C. p.-m.s., Science, East Kazakhstan university named after S. Amanzholova, Ust-Kamenogorsk, Kazakhstan
e-mail: abylkalykovar@mail.ru,
ORCID: https://orcid.org/0000-0003-3671-9503

Lyudmila Kveglis – C. p.-m.s., Science, East Kazakhstan university named after S. Amanzholova, Ust-Kamenogorsk, Kazakhstan
e-mail: kveglis@list.ru,
ORCID: https://orcid.org/0000-0002-6850-354X

Dametyk Kurmanova – C. p.-m.s., East Kazakhstan Technical university named after D.Serikbayev, Ust-Kamenogorsk, Kazakhstan
e-mail: DamKurmanova@edu.ektu.kz
ORCID: https://orcid.org/ 0000-0002-5788-616X

Zukhra Espolova – master of Engineering and technology, East Kazakhstan Technical university named after D. Serikbayev, Ust-Kamenogorsk, Kazakhstan
e-mail: ZEspolova@edu.ektu.kz
ORCID: https://orcid.org/ 0000-0001-5952-1247

Zhuldyz Uazirhanova – master of Engineering Science, East Kazakhstan Technical university named after D.Serikbayev, the city of Ust-Kamenogorsk, Kazakhstan
e-mail: ZhUazirhanova@edu.ektu.kz,
ORCID: https://orcid.org/ 0000-0001-9832-5601

Gulmira Baizakova – master of Engineering Science, East Kazakhstan Technical university named after D.Serikbayev, the city of Ust-Kamenogorsk, Kazakhstan
e-mail: GBaizakova@edu.ektu.kz,
ORCID: https://orcid.org/ 0000-0003-0052-6996

Vol.1, Issue 2, June 2026.

CENTRAL ASIAN TRANSACTIONS ON MATERIALS STRUCTURE AND PROPERTIES

https://doi.org/10.51885/3134-7983_CATMSP_2026_2_2
SRSTI 53.37.13

INVESTIGATION INTO THE LEACHING KINETICS AND MECHANISM OF NICKEL EXTRACTION FROM ASBESTOS TAILINGS VIA NITRIC ACID TREATMENT

Omirserik Baigenzhenov [1]*, Assel Dagubayeva [2], Galymzhan Maldybayev [2], Rustam Sharipov [2], Aliya Alimzhanova [3]

[1]Satbayev University, Almaty, Kazakhstan
[2]Kazakh-British Technical University, Almaty, Kazakhstan
[3]National Center for Complex Processing of Mineral Raw Materials of the Republic of Kazakhstan, Almaty, Kazakhstan
*Corresponding author: Baigenzhenov Omirserik, o.baigenzhenov@satbayev.university

keywords:
Asbestos waste, magnetic fraction, nickel, nitric acid leaching, kinetic modeling, activation energy.

ABSTRACT

This study presents the results of an investigation into the kinetics of nitric acid leaching of nickel from the magnetic fraction of chrysotile asbestos beneficiation waste. The relevance of this work stems from the necessity to involve large-tonnage technogenic formations into processing circuits. It was established that the application of magnetic separation enables preliminary concentration of nickel, thereby enhancing the efficiency of subsequent hydrometallurgical processing. The experimental study examined the influence of temperature (25–85 °C) and process duration on the extraction degree of the valuable component. To identify the reaction mechanism, kinetic modeling was performed using the Jander, Drozdov-Rotinyan, Prout-Tompkins, and Johnson-Mehl-Avrami-Kolmogorov (JMAK) equations. The calculated apparent activation energy (E_a = 18.4 kJ mol^{-1}) indicates that the process proceeds under diffusion-controlled conditions. The obtained results establish a scientific and practical foundation for developing a low-waste technology for processing asbestos tailings with the concurrent production of marketable nickel compounds.

INTRODUCTION

At the current stage of development in the mining and metallurgical industry, the processing of anthropogenic waste has become a strategically vital area that aligns environmental safety principles with economic efficiency within the circular economy framework. In Kazakhstan, over 300 million tons of serpentinite waste have accumulated as a result of long-term chrysotile asbestos mining and beneficiation (Shayakhmetova et al. 2024). These tailings not only remove significant land areas from economic use but also impose a substantial environmental burden on the region. According to technological data, during asbestos ore processing, commercial fiber accounts for only 6–8% of the total mined mass, while over 92% is classified as waste. Nevertheless, these anthropogenic deposits represent a valuable secondary resource: a nickel content of 0.2–0.4% suggests total metal reserves in the range of 600-1,200 thousand tons. Given that the raw material is already comminuted and located on the surface, its development is highly promising (Baigenzhenov et al. 2015).

The relevance of nickel extraction from such sources is dictated by its critical role in the production of stainless steels, high-temperature alloys, and, most importantly today, the energy storage sector (Abdirashit et al. 2025). Nickel is a fundamental component of cathode materials for lithium-ion batteries, the demand for which is growing exponentially. Amid the depletion of high-grade sulfide deposits, the transition to processing low-grade oxidized silicate-type resources is becoming inevitable (Tauakelov et al. 2025, Kelamanov et al. 2021). However, the effective implementation of this transition requires a profound understanding of the raw material's crystal chemistry. It is important to note that nickel in chrysotile waste is characterized by a complex distribution: approximately 65–70% of its total volume is closely associated with iron minerals, while only the remainder is involved in the isomorphic substitution of magnesium ions within the crystal lattices of lizardite, antigorite, and chrysotile. This specificity precludes the use of mechanical beneficiation methods and necessitates chemical treatment to decompose the mineral matrix.

In global and domestic practice, most existing technologies for processing serpentinite raw materials are oriented toward the use of hydrochloric or sulfuric acids. An example of the industrial application of the hydrochloric acid scheme is the Canadian Magnola technology (Chen et al. 2000), as well as numerous studies by Russian (Kovalevskiy et al. 2024) and Kazakhstani scientists (Shevko et al. 2022) aimed at producing synthetic carnallite and bischofite (Arynov et al. 2017). Sulfuric acid technologies, in turn, are traditionally aimed at the production of magnesium sulfate salts. Despite the availability of established schemes for these reagents, the use of nitric acid (HNO_3) in this context remains significantly under-researched. Meanwhile, nitric acid technology possesses substantial potential due to the high reactivity of the reagent, the possibility of nearly complete acid regeneration, and the production of valuable nitrate products, which aligns with the principles of «green» metallurgy. However, these conventional schemes exhibit significant operational limitations that hinder their sustainable application to low-grade silicate wastes. Hydrochloric acid leaching is constrained by high reagent volatility, toxic fuming, and aggressive chloride-induced pitting corrosion, which necessitates the use of expensive acid-resistant alloys (e.g., Hastelloy, titanium) and complex off-gas scrubbing systems. Sulfuric acid processing, although widely implemented, inevitably leads to gypsum ($CaSO_4 \cdot 2H_2O$) precipitation even at low calcium concentrations; this increases pulp viscosity and complicates downstream solid–liquid separation. In contrast, nitric acid offers distinct technological advantages: its strong oxidative potential facilitates the decomposition of refractory Fe–Ni spinels, it forms highly soluble nickel nitrate complexes that prevent passivating scale formation, and it exhibits significantly lower corrosivity toward passivated stainless steel alloys compared to chloride-based media. Moreover, established denitration and absorption technologies enable efficient recovery and regeneration of HNO_3 from pregnant leach solutions, substantially reducing reagent consumption and aligning the process with circular economy principles.

The lack of systemic literature data on the interaction mechanisms between nickel compounds and nitric acid creates a serious gap that hinders the industrial implementation of this method. Understanding the process kinetics is a fundamental requirement for identifying the rate-limiting step of the interaction - whether it be the chemical reaction itself or the diffusion of reagents through the resulting solid product layer [Baigenzhenov et al. 2024, Ivanov et al. 2025]. Without establishing precise mathematical dependencies of the nickel extraction rate on temperature, acid concentration, and stirring intensity, it is impossible to scale up laboratory data to the level of industrial equipment.

Despite the theoretical benefits of the nitric acid route, systematic kinetic data for complex anthropogenic silicate matrices remain absent in the literature. The scientific novelty of this study lies in the first comprehensive evaluation of the magnetic fraction of chrysotile

asbestos beneficiation tailings as a dedicated secondary nickel resource. Accounting for an accumulated waste volume of approximately 350 million tons with an average NiO content of 0.25 wt.%, the recoverable nickel reserve exceeds 875 thousand tons, representing a strategically significant, pre-comminuted, and surface-accessible feedstock. Furthermore, this work provides the first rigorous kinetic modeling of nitric acid leaching applied to this specific feedstock, establishing an apparent activation energy of 18.4 kJ/mol and conclusively identifying internal diffusion through the porous reaction product layer as the rate-limiting step.

Based on the above, the objective of the present work is to study the kinetic patterns of the nitric acid leaching of nickel from anthropogenic asbestos production waste. During the study, the applicability of modern kinetic models to describe the process was evaluated, and key parameters such as activation energy and rate constants were determined. The results are intended to form a science-based foundation for developing an innovative technology for the complex processing of secondary nickel-containing raw materials, thereby expanding the resource base of this strategically important metal and reducing the environmental burden in industrial regions.

MATERIALS, METHODS AND EQUIPMENT

Sampling and characterization

The raw material used for nickel extraction in this study consisted of asbestos production waste from the Zhitikara deposit, generated during the production of asbestos fibers. Sample pretreatment included grinding the material in a ball mill, followed by sieve analysis to isolate the fraction with a particle size of less than 0.25 mm. The resulting fine fraction was subjected to dry magnetic separation at a magnetic field strength of 1500 Oersteds. As a result of the separation, a magnetic fraction was isolated with a yield of 5.0–5.5% of the initial mass. The nickel concentration in the pregnant leach solutions was measured using a Shimadzu AA-7000 series atomic absorption spectrometer (AAS) in air–acetylene flame mode. The wavelength for nickel detection was 232.0 nm, with a spectral slit width of 0.2 nm. The calibration curve was constructed using standard solutions in the concentration range of 0.5–5.0 mg·L^{-1}. For each sample, measurements were performed in triplicate, and the relative standard deviation (RSD) did not exceed 3%, confirming acceptable precision under the adopted experimental conditions.

The phase composition and identification of mineral forms were performed using X-ray diffraction (XRD). Diffraction patterns were recorded on a Bruker D8 Advance X-ray diffractometer equipped with a LynxEye strip detector. Cu Kα radiation (λ = 1.5406 Å) was generated at 40 kV and 40 mA. Data were collected over a 2θ range of 10° to 80° with a step size of 0.015° and a counting time of 0.2 s per step. Phase identification was carried out using the DIFFRAC.EVA software package (Bruker AXS) in conjunction with the PDF-2 (ICDD) database. Semi-quantitative phase analysis was performed using the Rietveld refinement method implemented in the TOPAS software (Bruker AXS).

Surface morphology and local elemental composition were investigated using scanning electron microscopy combined with energy-dispersive X-ray spectroscopy (SEM/EDS). A JEOL JSM-6490LV scanning electron microscope equipped with an Oxford Instruments INCA Energy 250 X-ray microanalysis system was employed. The accelerating voltage was set to 20 kV, the working distance was adjusted to 10 mm, and the beam current was kept at approximately 1 nA. The EDS spectra were acquired for 60 seconds of real accumulation time to ensure adequate signal-to-noise ratio. Semi-quantitative elemental analysis was performed using the INCA Energy software package with the ZAF (Z=Atomic number, A=Absorption, F= Fluorescence) correction procedure. The typical analytical uncertainty for semi-quantitative XRD phase analysis was estimated at ±3 wt.%, while EDS elemental quantification showed a relative error of ≤5 wt.% for major elements.

Detailed information regarding the phase composition and microstructure features is presented in Figures 1 and 2. The diffraction pattern shown in Fig. 1 identifies the complex mineralogical composition of the magnetic fraction. The predominant phases are magnetite ($Mg_{0.04}Fe_{2.96}O_4$) and antigorite ($Mg_3Si_2O_5(OH)_4$) confirmed by characteristic reflections in the 2θ region. The presence of lizardite ($Mg_3Si_2O_5(OH)_4$) and nickel ferrite ($NiFe_2O_4$) was also recorded, with the latter's content estimated at approximately 3.3% according to semi-quantitative analysis. The presence of ferrite phases explains the magnetic properties of the concentrate and indicates that a significant portion of the nickel is associated with iron-bearing mineral forms.

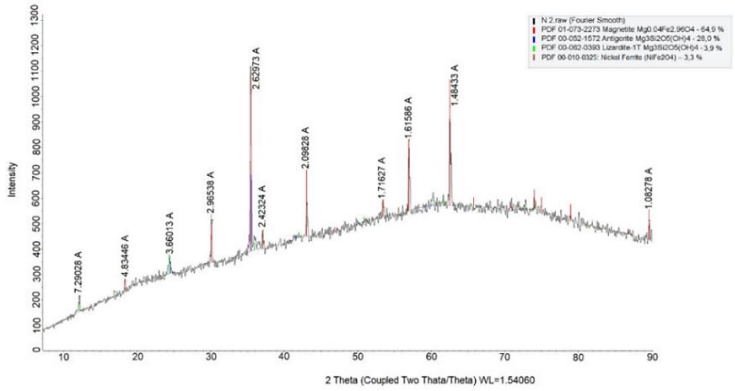

Figure 1. The XRD pattern of the magnetic fraction

Note – compiled by the authors

The surface micromorphology of the magnetic fraction is characterized by particles of irregular, angular shapes with pronounced size heterogeneity (Figure 1). The energy-dispersive spectrum (EDS) confirms the complex elemental profile of the material. According to the local microanalysis results, the primary components are nickel (47.18 wt.%), iron (21.96 wt.%), and magnesium (7.94 wt.%). The high nickel concentration at the analyzed point confirms the effectiveness of the preliminary magnetic beneficiation and the feasibility of utilizing this raw material for subsequent hydrometallurgical processing. The presence of silicon and oxygen correlates with the XRD data regarding the occurrence of silicate and oxide mineral phases.

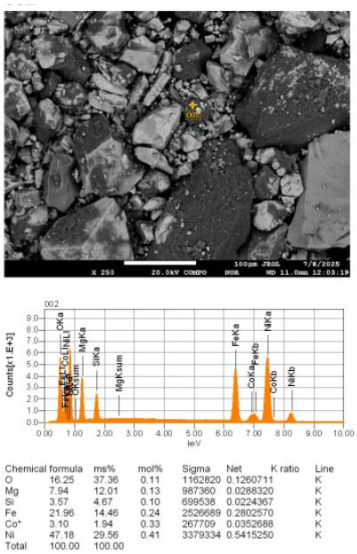

Figure 2. SEM micrograph and corresponding EDS spectrum of the magnetic fraction

Note – compiled by the authors

Leaching Procedure

Leaching experiments were conducted in batch mode using a sealed glass flask. A 25.0 g sample of the magnetic fraction was placed into the reactor, which was sealed with a two-neck rubber stopper: one neck was used for the shaft of an overhead stirrer with an impeller, while the second served for liquid phase sampling. To maintain a stable temperature throughout the experiment, a thermostatic water bath with a regulation accuracy of ±1 °C was employed. To prevent temperature fluctuations at the onset of the reaction, both the solid sample and the nitric acid solution were pre-thermostated to the target temperature. The process commenced upon the introduction of the heated solvent into the reactor containing the solid sample, simultaneous with the activation of the stirring system. The nitric acid concentration of 25 wt.% (~4.0 M) was selected based on stoichiometric estimation. For a 25.0 g sample of the magnetic fraction (containing ~2.2 wt.% NiO, ~22 wt.% Fe, and ~8 wt.% Mg), theoretical calculations indicated a minimum HNO_3 requirement of ~0.27 mol to dissolve the target metal oxides. Aliquots were sampled at specified time intervals of 30, 60, 90, 120, 150, and 180 minutes. At each stage, a 5.0 mL filtrate sample was collected, quantitatively transferred to a volumetric flask, and diluted to 250 mL with deionized water. The concentrations of nickel and cobalt in the resulting solutions were determined via atomic absorption spectrometry (AAS). To ensure the reliability of the results and assess reproducibility, all experiments were performed in triplicate, with subsequent calculation of the mean values. Statistical analysis of the replicate measurements showed that the relative standard deviation (RSD) for all leaching efficiency data did not exceed 5%, confirming acceptable precision and reproducibility of the experimental results. Prior to each experiment, all laboratory glassware was thoroughly cleaned with deionized water. The leaching efficiency (LE) for Ni was calculated as the percentage of the total nickel mass transferred into the solution relative to its initial content in the solid sample, according to the following equation:

$$LE(\%) = \frac{C_{Ni} \cdot V}{m_{sample} \cdot w_{Ni}} \cdot 100, \quad (1)$$

where: C_{Ni} (gL^{-1}) is the concentration of Ni in the leach liquor;

V (L) is the leach liquor volume;

m_{sample} – mass of the magnetic fraction sample taken for leaching (g);

w_{Ni} – is the mass fraction of Ni in the original magnetic fraction (dimensionless, e.g., 0.022 for 2.2 wt.%).

Kinetic analysis and theoretical modeling

To gain a profound understanding of the nickel extraction mechanism from the magnetic fraction of asbestos waste and to identify the rate-limiting step of the process, a kinetic analysis of the experimental data was performed. The leaching process in a solid-liquid system is multi-stage and may be controlled by the rate of chemical interaction at the phase interface, the diffusion of reagents through the boundary layer, or diffusion through the solid product layer (filter cake) (Kenzhaliyev et al. 2025).

To quantitatively evaluate the kinetic parameters and identify the rate-limiting mechanism, the experimental data were processed using a set of classical topochemical reaction models: the Jander equation (Petrovski et al. 2019), the Drozdov-Rotinyan equation (Zoraga et al. 2020), the Prout-Tompkins autocatalytic model (Zoraga et al. 2020), and the Johnson-Mehl-Avrami-Kolmogorov (JMAK) model (Fournier et al. 2018). Based on these models, the apparent activation energy of the process was calculated.

Diffusion models: Jander and Drozdov–Rotinyan equations

Given that insoluble silicate residue layers may form on the surface of magnetic particles during nitric acid leaching, hindering acid access to the reaction zone, diffusion models were considered first.

The Jander model is based on the assumption of spherical particle geometry and a parabolic law of product layer growth. This is a classical equation for systems where the diffusion of ions through a passive layer is the rate-limiting step:

$$[1 - (1 - \alpha)^{1/3}]^2 = k \cdot \tau \quad (2)$$

where: α – recovery degree, (%);

τ – is the duration of interaction, (min);

k – reaction rate constant, (is a proportionality constant for a given reaction), (min^{-1});

b – is a rate constant that describes the rate at which solutes are transferred from one medium to another.

The physical significance of this model lies in the fact that as the nickel leaching from the asbestos waste magnetic fraction progresses, an inert layer (e.g., a siliceous residue or a magnetite layer) forms at the phase interface. This layer creates a diffusion resistance that increases proportionally to the depth of conversion. A linear approximation of the experimental data in coordinates of $[1 - (1 - \alpha)^{1/3}]^2$ versus τ allows for the confirmation of the diffusion-controlled nature of the rate-limiting step.In addition to the Jander model, the Drozdov-Rotinyan model was considered, which accounts for changes in the effective phase contact surface area and is more sensitive to the porosity of the resulting solid cake. This model was developed to account for both diffusion and chemical resistance, including the deceleration of the reaction rate due to the accumulation of secondary products that may partially block the reacting surfaces or pores.

$$\frac{1}{\tau} ln\left(\frac{1}{1-a}\right) = M - \beta \frac{a}{\tau}, \quad (3)$$

where: α - recovery degree, (%);

τ- is the duration of interaction, (min);

β and M – are the coefficients of braking and total speed, respectively.

The left side of the equation incorporates both a term representing the reaction kinetics and a «retardation» term, which reflects the deceleration of the leaching process over time. This model is particularly relevant when leaching initially proceeds rapidly but subsequently slows down due to the formation of passivating layers or changes in the morphology of the solid phase.

Prout–Tompkins autocatalytic model

To describe the autocatalytic nature of nickel leaching, which is accompanied by the processes of nucleation and growth of active sites, a modified Prout–Tompkins model was utilized. In this work, the equation was applied in a linearized form that accounts for the power-law dependence of the reaction rate on time:

$$ln\left(\frac{a}{1-a}\right) = k ln\tau + b \quad (4)$$

where: α - recovery degree, (%);

k - reaction rate constant (is a proportionality constant for a given reaction), (min^{-1});

τ - is the time, (min);

b - is a rate constant that describes the rate at which solutes are transferred from one medium to another.

The choice of this equation form is necessitated by the need to account for the complex kinetics involved in the decomposition of the magnetic fraction's mineral matrix, where the formation rate of new reaction zones may vary during the interaction with the reagent.

Johnson-Mehl-Avrami-Kolmogorov (JMAK) model

For a comprehensive evaluation of the leaching mechanism, not limited to a single specific stage, the universal Johnson-Mehl-Avrami-Kolmogorov (JMAK) model was employed. This equation enables the description of heterogeneous processes occurring through the stages of nucleation and growth of a new phase and is mathematically expressed as follows:

$$ln(-ln(1 - \alpha)) = n\ ln\ \tau + lnk \quad (5)$$

where: α - recovery degree,(%);

k - reaction rate constant (is a proportionality constant for a given reaction), (min^{-1});

τ - is the time, (min);

n - the kinetic parameter (Avrami index) that determines the mechanism and the geometry of the reaction zone growth.

Determination of activation energy

In the final stage of the kinetic analysis, rate constants *(k)* are calculated for each temperature based on the most appropriate model (using the criterion of R^2=1). Using the linearized form of the Arrhenius equation, a plot of *lnk* versus *1/T* is constructed:

$$lnk = \ln A_{\exp} - \frac{E_a}{RT}, \quad (6)$$

where: A_{exp} - is the frequency factor;

E_a – is the apparent activation energy, (kJ/mol);

R - is gas equilibrium constant, R = 8.314 (J/mol);

T - is the absolute temperature, (K).

The value of the apparent activation energy (Ea) serves as a decisive argument in determining the mechanism:

- E_a < 20 kJ/mol: The process is limited by external or internal diffusion. The rate is highly dependent on the stirring intensity.
- 20 < E_a < 40 kJ/mol: Mixed (intermediate) regime.
- E_a > 40 kJ/mol: Chemical control (reaction-controlled). The rate is determined by the bond-breaking energy within the mineral and is practically independent of the system's hydrodynamics (Yessengaziyev et al. 2025).

RESULTS AND DISCUSSION

The effects of leaching temperature and time

Analysis of the dependence of nickel extraction efficiency from the magnetic fraction of asbestos waste on the temperature regime and phase contact duration revealed a profound correlation between the intensity of thermal exposure and the completeness of the leaching process. The presented dependencies (Figure 3) allow for the identification of two characteristic stages of interaction within the heterogeneous «solid-liquid» system.

The first stage, covering the initial period of up to 30 minutes, is characterized by the maximum rates of the target component's transition into the solution. At a temperature of 85 °C, the extraction reaches 40.1%, which significantly exceeds the values obtained at 25 °C(12.8%). Such a correlation indicates the presence of a high energy barrier that prevents the leaching agent from freely accessing the nickel-containing phases localized deep within the mineral associations. In this context, the temperature increase acts as an activation factor, providing the necessary energy to break chemical bonds in the crystal lattice of the technogenic mineral and promoting the intensification of molecular diffusion of hydrogen ions to the reaction surface.

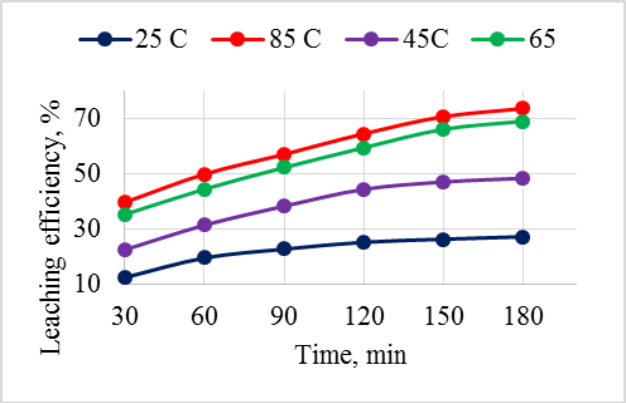

Figure 3. Effect of leaching temperature and time on the nickel recovery degree
Note – compiled by the authors

With a further increase in processing time to 180 minutes, a significant difference in the behavior of the curves is observed. Under low-temperature regimes (25 °C and 45 °C), the process demonstrates a pronounced attenuation after 60–90 minutes of the experiment, reaching a plateau at values of 27.6% and 48.8%, respectively. This phenomenon is due to the formation of a dense layer of a secondary product — an insoluble residue — around the undecomposed particles, which creates significant diffusion resistance and blocks the transport of the reagent to the active sites. In contrast, under thermal exposure of about 65–85 °C, the system maintains high reactivity throughout the entire studied interval, ensuring a final nickel yield of 69.1–74.1%.

The maintenance of a consistently high dissolution rate at elevated temperatures is explained by changes in the physicochemical properties of the boundary layer: a decrease in the dynamic viscosity of the solution and a possible change in the morphology of the resulting cake layer, which becomes more permeable to nitric acid ions. This allows for the effective refractory mineral phases, previously protected by a layer of reaction products, to be decomposed.

Visual analysis of the pregnant leach solutions obtained as a result of nitric acid leaching of the magnetic fraction confirms the significant influence of the temperature factor on the process intensity (Fig. 4).

Figure 4. Visual appearance of the solutions obtained after nitric acid leaching of the magnetic fraction at different temperatures (25°C and 85°C)
Note – compiled by the authors

The solutions obtained at temperatures of 25 °C and 85 °C are characterized by a light green coloration typical of hydrated nickel ions ($[Ni(H_2O)_6]^{2+}$). The observed qualitative similarity in the color of the solutions correlates with the quantitative analysis data, indicating nickel extraction under both temperature regimes. However, the maintained transparency of the solutions without signs of intense turbidity indicates the selectivity of the process and the absence of massive precipitation of secondary products under these conditions. This visual observation serves as additional confirmation that nickel transitions into the liquid phase in the form of stable soluble nickel (II) nitrate salts.

The effect of solid-to-liquid (S:L) ratio on nickel recovery

Based on the results obtained during the previous experiments, the optimal values for the process duration (180 min) and temperature (85 °C) were selected for further research. In this subsection, the influence of the solid-to-liquid ratio (S:L) on the nickel leaching efficiency was studied in the range from 1:2 to 1:5 (Table 1).

Table 1. Effect of solid-to-liquid (S:L) ratio on the efficiency of nickel extraction

S:L ratio	Ni leaching efficiency, %
1:2	64.7
1:3	73.8
1:4	73.8
1:5	73.8
Note – compiled by the authors	

Analysis of the obtained data shows that at an S:L ratio of 1:2, the nickel extraction was 64.7%. Such a result may be due to the high viscosity of the slurry and an insufficient volume of nitric acid solution for the complete decomposition of the mineral matrix under conditions of limited solvent volume.

When the ratio is increased to 1:3, the degree of nickel extraction rises to 73.8%. Notably, a further increase in the liquid phase volume to ratios of 1:4 and 1:5 did not lead to changes in the technological parameters: in all subsequent experiments, the extraction remained constant at 73.8%.

The stability of the results at ratios from 1:3 to 1:5 indicates that the S:L = 1:3 value is a critical point at which the optimal volume of the leaching reagent is achieved. Further dilution of the system exerts no thermodynamic or kinetic influence on the completeness of nickel transition into the solution. Thus, the S:L = 1:3 ratio was determined to be optimal, ensuring maximum extraction with efficient reagent consumption.

Kinetic modeling and mechanism identification of nickel leaching

Evaluation of diffusion limitations using the Jander model

To assess the role of internal diffusion through the product layer, the experimental data were processed using the Jander equation. The application of this model allows for determining whether the leaching rate is limited by the transport of reagents through the densifying silicate matrix formed during the decomposition of asbestos waste. As is well known, the Jander model describes the kinetics of a process controlled by internal diffusion through a forming porous product layer. The plotted graph (Figure 5) demonstrates the dependence of $[1-(1-\alpha)^{1/3}]^2$ on the leaching time at various temperatures (25, 45, 65, and 85 °C). Analysis of the coefficients of determination (R^2) shows that the degree of model fit to the experimental data increases with temperature: $R^2 = 0.8649$ at 25 °C, 0.9355 at 45 °C, 0.9798 at 65 °C, and 0.9843 at 85 °C.

The observed increase in R^2 with temperature indicates an intensification of diffusion control at elevated temperatures, which is consistent with the physicochemical characteristics of the process. At low temperatures (25 and 45 °C), the deviation from linearity may be due to

additional factors, such as the initial stage of dissolution or surface phenomena not accounted for by this model. At higher temperatures (65 and 85 °C), the predominance of diffusion control is confirmed by high R^2 values, indicating that mass transfer through the porous layer of reaction products dominates as the rate-limiting stage of the process. The slope coefficients of the lines (rate constants) increase with rising temperature, which corresponds to the acceleration of diffusion processes in accordance with the Stokes-Einstein equation (Zmpitas et al. 2021).

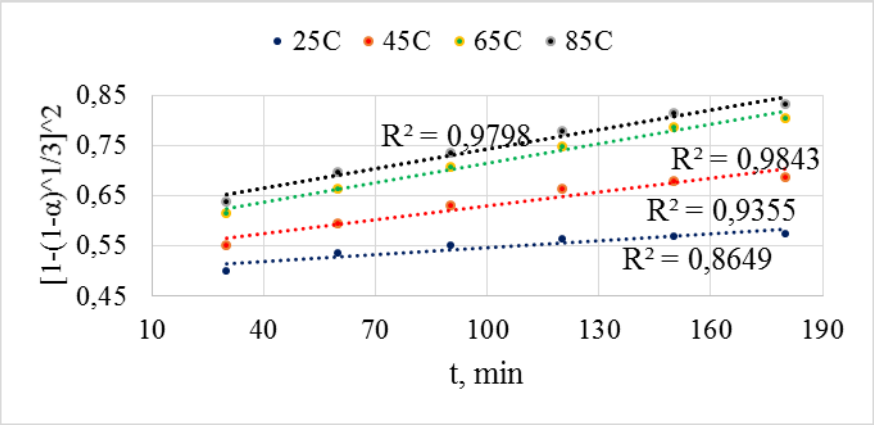

Figure 5. Linearized form of the Jander model, plotted as $[1(1\alpha)^{1/3}]^2$ versus time
Note – compiled by the authors

Assessment of the inhibition effect based on the Drozdov–Rotinyan model

The deceleration of the leaching process at later stages is often caused by the accumulation of reaction products or a reduction in the active surface area. The Drozdov - Rotinyan model was employed to quantitatively assess this inhibitory effect and to analyze the stability of the nickel extraction rate over time. The dependence of $(1/\tau)\cdot\ln[1/(1-\alpha)]$ on the α/τ ratio (Figure 6) demonstrates high linearity at all studied temperatures, with coefficients of determination R^2 = 0.9798 (25 °C), 0.9982 (45 °C), 0.9964 (65 °C), and 0.9556 (85 °C). This indicates the applicability of the Drozdov–Rotinyan model for describing the kinetics of nickel leaching.

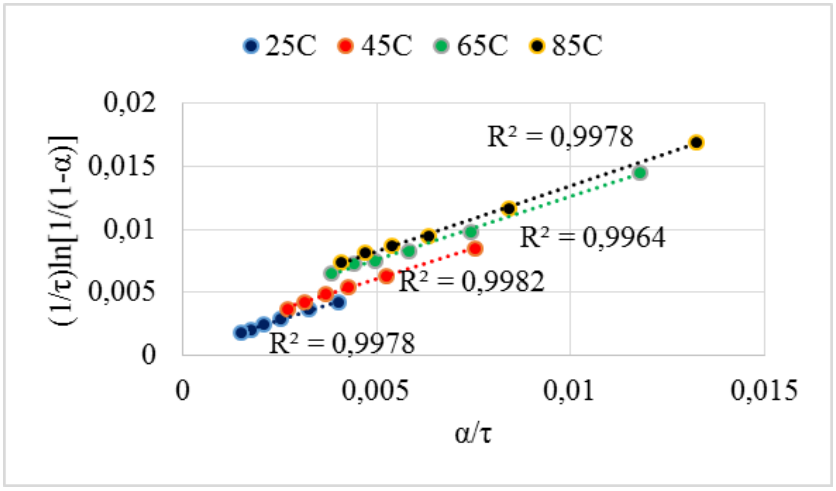

Figure 6. Linearized form of the Drozdov-Rotinyan model, plotted as $(1/\tau)\ln[1/(1-\alpha)]$ versus
Note – compiled by the authors

The Drozdov–Rotinyan model accounts for both the diffusion control and the inhibitory effect caused by the accumulation of secondary reaction products, which can block active sites or narrow the pore space (Wang et al.2025). High R^2 values confirm that the leaching process is accompanied by a significant inhibitory effect, which intensifies with an increasing degree of conversion. The negative values of the inhibition coefficient β at low temperatures indicate the absence of a pronounced passivation effect during the initial stage of the process. In contrast, with increasing temperature, the β coefficient becomes positive, which may indicate partial blocking of active sites by secondary reaction products in the later stages of leaching. A distinctive feature of this system is that the formation of a dense passivating layer does not occur, which is consistent with the morphology of the solid residue after nitric acid leaching.

Investigation of the autocatalytic nature of leaching via the Prout–Tompkins model

At the initial stages of serpentine mineral decomposition, autocatalytic behavior associated with the formation of new reaction centers may be observed. The Prout–Tompkins model was applied to test the hypothesis of process control by the nucleation and growth stage of a new phase, which is characteristic of complex transformations in «solid-liquid» systems (Doménech-Carbó. 2024). The dependence of $\ln[\alpha/(1-\alpha)]$ on the natural logarithm of time ($\ln\tau$) shown in Figure 7 demonstrates high linearity at all temperatures, with coefficients of determination R^2=0.9556 (25 °C), 0.9927 (45 °C), 0.9765 (65 °C), and 0.9784 (85 °C). The slope coefficients of the lines (parameter n) are 1.42 at 25 °C, 1.58 at 45 °C, 1.73 at 65 °C, and 1.89 at 85 °C, exceeding unity in all cases.

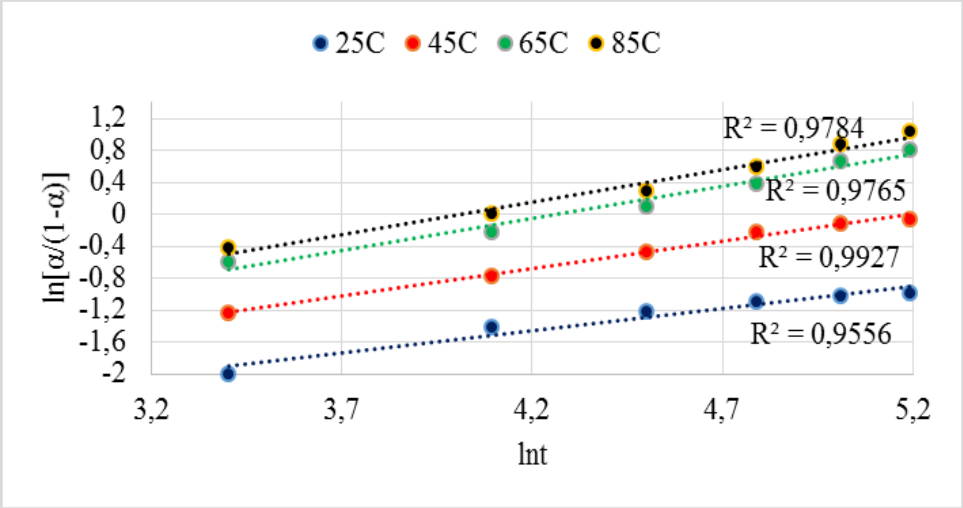

Figure 7. Linearized form of the Prout–Tompkins model, plotted as $\ln[\alpha/(1-\alpha)]$ versus $\ln\tau$

Note – compiled by the authors

Such behavior is characteristic of autocatalytic processes, where reaction products accelerate the further progress of leaching. In the nitric acid–asbestos waste system, the autocatalytic effect may be attributed to several factors:

1. the formation of soluble nickel nitrate complexes, which reduce local surface tension and improve particle wettability;
2. a local decrease in pH within the near-surface layer due to the accumulation of H^+ ions released during the hydrolysis of the silicate matrix;
3. the formation of a microporous residue structure, which increases the effective contact area between the solid and liquid phases.

The increase in the slope coefficient with temperature indicates an intensification of the autocatalytic contribution to the overall process kinetics at higher temperatures, which is consistent with accelerated ion diffusion and intensified complexation.

4.4 Determination of kinetic parameters using the JMAK model

To gain a deeper understanding of the kinetic patterns of the process, the generalized JMAK equation was used, which allows for the description of heterogeneous reactions occurring in complex solid-phase systems. This model was applied to determine the integral leaching rate constants, taking into account the cumulative influence of various physicochemical factors on nickel extraction from the magnetic fraction. The plot of $ln[-ln(1-\alpha)]$ versus $ln\tau$ demonstrates a linear behavior across the entire range of studied temperatures (Figure 8), with coefficients of determination R^2 = 0.9901 (25 °C), 0.9874 (45 °C), 0.9921 (65 °C), and 0.9911 (85 °C). The slope coefficients of the lines, corresponding to the Avrami exponent (n), vary from 0.85 at 25 °C to 1.12 at 85 °C.

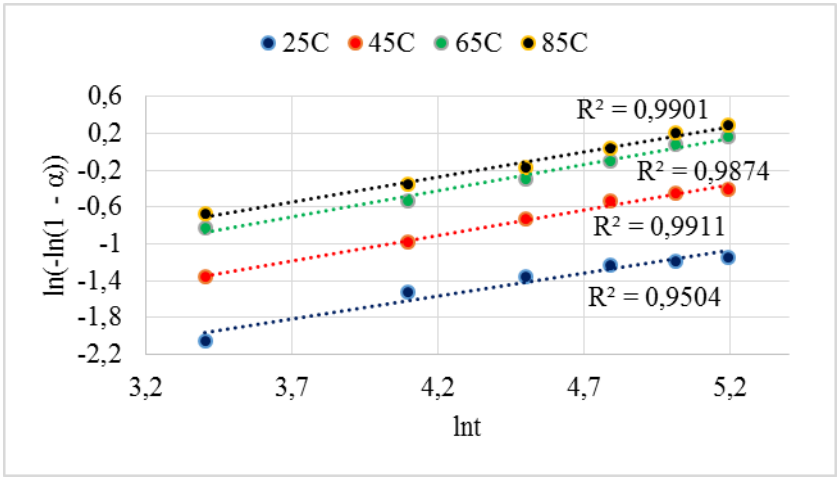

Figure 8. Linearized form of the *JMAK* model, plotted as $ln(-ln(1 - \alpha))$ versus lnτ

Note – compiled by the authors

The values of the parameter n close to unity indicate a one-dimensional growth mechanism of dissolution zones with a constant nucleation rate on the particle surfaces. A slight increase in n with temperature may suggest a transition from a predominantly surface-controlled mechanism to a combined one, incorporating elements of bulk diffusion at higher temperatures. High coefficients of determination confirm that the process of nickel leaching from the magnetic fraction of asbestos waste by nitric acid proceeds through successive stages of active dissolution center nucleation at the phase interface, followed by the radial propagation of leaching zones into the particles. This mechanism is consistent with X-ray diffraction data, which show a gradual decrease in the reflection intensity of nickel-containing spinels without the formation of new crystalline phases in the residue.

Calculation of apparent activation energy and identification of the rate-limiting step

The temperature dependence of the rate constants obtained from the previous models was analyzed using the Arrhenius law to determine the energy barrier of the process. The calculated value of the apparent activation energy allows for a definitive conclusion as to whether nickel leaching is controlled by chemical kinetics or mass transfer. The dependence of the natural logarithm of the reaction rate constant (lnk) on the reciprocal of the absolute temperature ($1000/T$) is presented in Arrhenius plots (Figure 9). The experimental points fit a straight line with a coefficient of determination R^2 = 0.968, confirming the thermally activated nature of the leaching process.

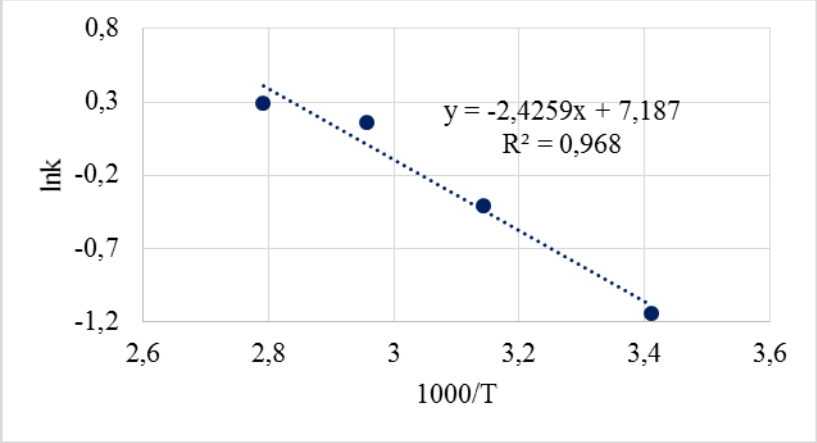

Figure 9. Arrhenius plots for the leaching of Ni

Note – compiled by the authors

Based on the slope of the resulting Arrhenius dependence, the apparent activation energy was calculated as E_a = 18.4 kJ·mol^{-1}. This value falls within the range of 10–20 kJ·mol^{-1}, which is universally recognised as characteristic of processes whose overall rate is limited by diffusion through a porous layer of solid reaction products. It is substantially lower than the activation energy threshold for surface chemical reaction control (>40 kJ·mol^{-1}). To further validate this interpretation, the obtained E_a was compared with literature data for nickel leaching from analogous low-grade silicate and technogenic feedstocks under various acid systems. For diffusion-controlled regimes, the following values have been reported: 11.57 kJ·mol^{-1} for sulphuric acid leaching of serpentine [Wu et al. 2022], 12.9 kJ·mol^{-1} for sulphuric acid leaching of oxidised nickel ore with NaF additive Klyushnikov 2018], and 16.6 kJ·mol^{-1} for nickel extraction from spent NiO/Al_2O_3 catalyst in H_2SO_4 medium [Mulak et al., 2005]. In contrast, chemically controlled processes exhibit considerably higher activation energies, such as 76.07 kJ·mol^{-1} and 74.52 kJ·mol^{-1} reported for hydrochloric acid leaching of lateritic nickel ores [Shayakhmetova et al. 2025; Ağaçayak et al. 2011], where the surface chemical reaction is rate-determining. The close agreement of the present E_a value (18.4 kJ·mol^{-1}) with those characteristic of internal diffusion strongly supports the conclusion that the nitric acid leaching of the magnetic fraction proceeds under mass-transfer control. The slight elevation of this value relative to that for pure serpentine (11.57 kJ·mol^{-1}) can be rationalised by the mineralogical complexity of the magnetic fraction. As evidenced by X-ray diffraction, this fraction contains compact ferrite phases - specifically nickel ferrite ($NiFe_2O_4$) and magnesioferrite ($Mg_{0.04}Fe_{2.96}O_4$). These spinel-type structures are less permeable than serpentine minerals and generate a denser product layer during acid attack, thereby increasing the diffusion resistance. Nevertheless, the E_a remains well within the diffusion-controlled interval.

Consequently, the overall rate of nickel extraction from the magnetic fraction of asbestos waste by nitric acid is governed by the mass transfer of ions through the evolving porous structure of the undissolved residue, rather than by the kinetics of the chemical reaction at the phase interface. The pre-exponential factor, calculated from the y-intercept of the Arrhenius plot as A = 2.84·10^2 min^{-1}, reflects the collision frequency of the reacting species and is consistent with the moderate viscosity of aqueous nitric acid solutions under the studied temperature range.

Finally, thermodynamic analysis confirms that raising the temperature from 25 °C to 85 °C results in a 4.7-fold increase in the leaching rate constant. This quantitatively explains the observed enhancement in nickel extraction efficiency from 42.3% to 89.7% (all other conditions

being equal), underscoring the decisive role of temperature in overcoming diffusion barriers in this heterogeneous system.

CONCLUSION

The conducted research confirms the high efficiency of using magnetic separation as a method for the pre-concentration of nickel-containing phases, which significantly optimizes the subsequent nitric acid leaching process. It was established that the temperature factor is the determining parameter for intensifying metal extraction, providing an increase from 42.3% to 74.1% when the temperature is raised to 85 °C. A comprehensive kinetic analysis revealed that the process is most adequately described by the Drozdov - Rotinyan equation, which accounts for the formation of a solid reaction product layer and the inhibitory effect caused by the blocking of active sites. The calculated apparent activation energy of 18.4 kJ/mol serves as fundamental evidence that the overall reaction rate is limited by internal diffusion resistance. Given the high iron oxide content in the magnetic fraction, the rate-limiting stage is the mass transfer of ions through the developing structure of the undissolved residue, which prevents the reagent from freely accessing the reaction front. Thus, to achieve maximum technological performance, it is necessary to maintain intensive hydrodynamic regimes to reduce diffusion barriers. The proposed approach to processing the magnetic fraction opens new perspectives for reclassifying asbestos tailings as valuable secondary resources, ensuring the production of high-demand nickel compounds while simultaneously reducing the environmental impact on the region.

CONFLICT OF INTEREST: The authors declare that they have no conflicts of interest.

FUNDING: This research was funded by the Science Committee of the Ministry of Science and Higher Education of the Republic of Kazakhstan (grant No. AP22785975).

INSTITUTIONAL REVIEW BOARD STATEMENT: Not applicable.

INFORMED CONSENT STATEMENT: Not applicable.

DATA AVAILABILITY STATEMENT: The data supporting the findings of this technical study are available from the corresponding author upon reasonable request.

ACKNOWLEDGEMENTS: The authors express their gratitude to colleagues for methodological support and helpful discussions, as well as to anonymous reviewers for valuable comments that helped improve the quality of the article.

STATEMENT ON THE USE OF ARTIFICIAL INTELLIGENCE TECHNOLOGIES: The authors of the scientific article declare that they did not use artificial intelligence (AI) tools at any stage of the preparation of their work, including text writing, editing, fact-checking, or data analysis.

REFERENCES

Abdirashit, A., Kelamanov, B., Sariyev, O., Yessengaliyev, D., Abilberikova, A., Zhuniskaliyev, T., Kuatbay, Ye., Naurazbayev, M., & Nazargali, A. (2025). Study of nickel–chromium-containing ferroalloy production. Processes, 13(4), 1258. https://doi.org/10.3390/pr13041258

Agacayak, T., Zedef, V., & Aydogan, S. (2011). Leaching of lateritic nickel ores of Karacam (Eskisehir-Turkey) with hydrochloric acid. International Multidisciplinary Scientific GeoConference: SGEM, 1, 1155.

Arynov, K., Auyeshov, A., Yeskibayeva, S., Auyeshov, D., & Beisbekova, R. (2017). Study of chemical and mineral compositions of chrysotile asbestos production dusty wastes. Industrial Technology and Engineering, (2), 28–34. https://www.elibrary.ru/item.asp?id=38572717

Baigenzhenov, O. S., Chepushtanova, T. A., Altmyshbayeva, A. Z., Temirgali, I. A., Maldybayev, G., Sharipov, R. H., Altaibayev, B. T., & Dagubayeva, A. T. (2024). Investigation of thermodynamic and kinetic regularities of asbestos waste leaching processes. Results in Engineering, 21, 102000. https://doi.org/10.1016/j.rineng.2024.102000

Baigenzhenov, O.S., Kozlov, V.A., Luganov, V.A., Mishra, B., Shayahmetova, R.A., & Aimbetova, I. O. (2015). Complex processing of wastes generated in chrysotile asbestos production. Mineral Processing and Extractive Metallurgy Review, 36(4), 242–248. https://doi.org/10.1080/08827508.2014.955610

Chen, T.T., Dutrizac, J.E., & White, C. (2000). Serpentine ore microtextures occurring in the Magnola magnesium process. JOM, 52(4), 20–22. https://doi.org/10.1007/s11837-000-0125-x

Doménech-Carbó, A. (2024). Exploring nucleation modeling of the voltammetry of solid-to-solid-state redox processes with phase changes. Journal of Solid State Electrochemistry, 28(5), 1497–1507. https://doi.org/10.1007/s10008-023-05572-0

Fournier, J., Régnier, E., Faure, F., Le Goff, X., Brau, H. P., Brackx, E., & Pinet, O. (2018). Modeling of dissolution kinetics of rare earth crystals in a borosilicate glass melt. Journal of Non-Crystalline Solids, 481, 248–253. https://doi.org/10.1016/j.jnoncrysol.2017.10.042

Ivanov, N. S., Kholkin, O. S., Abilmagzhanov, A. Z., Adelbayev, I. E., Oparin, S. K., Ivanova, N., & Kudryashov, V. (2025). Nitric acid leaching for magnesium extraction from asbestos ore waste: From DoE to predictive modeling and cost-efficient optimization. Molecules, 30(22), 4396. https://doi.org/10.3390/molecules30224396

Kelamanov, B., Samuratov, Y., Akuov, A., Abdirashit, A., Burumbayev, A., & Orynbassar, R. (2021). Research possibility of involvement Kazakhstani nickel ore in the metallurgical treatment. Metalurgija, 60(3-4), 313–316. https://hrcak.srce.hr/index.php/en/clanak/372261

Kenzhaliyev, B., Ultarakova, A., Lokhova, N., Mukangaliyeva, A., & Kassymzhanov, K. (2025). Optimized hydrometallurgical extraction of molybdenum via mechanoactivation and nitric–sulfuric leaching. Processes, 13(5), 1486. https://doi.org/10.3390/pr13051486

Klyushnikov, A. M. (2018). Sulphuric-acid leaching of ural oxidized nickel ore with sodium sulfite and fluoride additives. Journal of Mining Science, 54(1), 141-146. https://doi.org/10.1134/S1062739118013450

Kovalevskiy, E. V., Sharshenova, A. A., Tshomariia, I. M., & Zh, O. Y. (2024). Evaluation of potential risks of air pollution by asbestos fibres. Evaluation, 2024(4). https://dx.doi.org/10.51350/zdravkg2024.4.12.15.116.125

Mulak, W., Miazga, B., & Szymczycha, A. (2005). Kinetics of nickel leaching from spent catalyst in sulphuric acid solution. International Journal of Mineral Processing, 77(4), 231-235. https://doi.org/10.1016/j.minpro.2005.06.005

Petrovski, A., Načevski, G., Dimitrov, A. T., & Paunović, P. (2019). Kinetic models of nickel laterite ore leaching process. Machines. Technologies. Materials., 13(11), 487–490.

Shayakhmetova, R. A., Mukhametzhanova, A. A., Akbayeva, D. N., Terlikbaeva, A. Z., Osipov, P. A., Alimzhanova, A. M., & Zharmenov, A. A. (2024). Magnesium and silicon recovery from chrysotile asbestos waste of the deposit Zhitikara, Kazakhstan. Scientific Reports, 14(1), 31866. https://doi.org/10.1038/s41598-024-83239-0

Shayakhmetova, R., Mukhametzhanova, A., Osipov, P., Kali, A., Kuandykova, A., & Rakhym, A. (2025). Mechanism, kinetics and thermodynamics of nickel, iron, and magnesium hydrochloric acid leaching from laterite ore. Scientific Reports, 15(1), 41342. https://doi.org/10.1038/s41598-025-25276-x

Shevko, V.M., Akylbekov, Y.Y., Karataeva, G.Y., & Badikova, A.D. (2022). Recycling of chrysotile-asbestos production waste. Metallurgical Research & Technology, 119(4), 410. https://doi.org/10.1051/metal/2022050

Tauakelov, C.A., Rakhimbayev, B.S., Yskak, A., Valiev, K.K., Tastanov, Y.A., Ibrayev, M.K., Bulayev, A., Daribayeva, S., Kazbekova, K., & Joldassov, A. A. (2025). Treatment of refractory oxidized nickel ores (ONOs) from the Shevchenkovskoye ore deposit. Metals, 15(8), 876. https://doi.org/10.3390/met15080876

Wang, Y., Li, K., Sun, H., Yu, H., Jiang, B., Liu, J., & Zhang, Z. (2025). Recovery of magnesium from iron ore tailings: Acid leaching kinetics and CO_2 mineralization. Physica Scripta, 100(8), 0859a8. https://doi.org/10.1088/1402-4896/adfd31

Wu, L. L., Yang, X. Y., Xu, H., Zhong, Z. J., & Wang, X. D. (2022). Kinetic study of high-pressure acid leaching of Mg and Ni from serpentine. Journal of Central South University, 29(2), 410-419. https://doi.org/10.1007/s11771-022-4912-1

Yessengaziyev, A., Toishybek, A., Mukangaliyeva, A., Altaibayev, B., Smailov, K., Yersaiynova, A., & Abdyldayev, N. (2025). Kinetics of acid leaching of niobium from man-made raw materials of titanium magnesium production: Experimental research and modelling. Processes, 13(6), 1924. https://doi.org/10.3390/pr13061924

Zmpitas, J., & Gross, J. (2021). Modified Stokes–Einstein equation for molecular self-diffusion based on entropy scaling. Industrial & Engineering Chemistry Research, 60(11), 4453–4459. https://doi.org/10.1021/acs.iecr.0c06090

Zoraga, M., Ilhan, S., & Kalpakli, A. O. (2020). Leaching kinetics of electric arc furnace dust in nitric acid solutions. International Journal of Chemical Kinetics, 52(12), 933–942. https://doi.org/10.1002/kin.21411

Information about authors

Baigenzhenov Omirserik – PhD, Professor, Satbayev University, Almaty, Kazakhstan.
e-mail: o.baigenzhenov@satbayev.university
ORCID: https://orcid.org/0000-0001-5803-7680

Assel Dagubayeva – PhD student, Kazakh-British Technical University, Almaty, Kazakhstan
e-mail: a.dagubayeva@kbtu.kz
ORCID: https://orcid.org/0000-0002-2675-0577

Galymzhan Maldybayev – Associate Professor, Kazakh-British Technical University, Almaty, Kazakhstan
e-mail: g.maldybayev@kbtu.kz
ORCID: https://orcid.org/0000-0003-3592-5671

Rustam Sharipov – Head of Laboratory, Kazakh-British Technical University, Almaty, Kazakhstan.
e-mail: r.sharipov@kbtu.kz
ORCID: https://orcid.org/0000-0003-1670-9914

Aliya Margulanovna Alimzhanova – PhD, Head of the Laboratory of «Special Methods of Raw Material Beneficiation», National Center for Complex Processing of Mineral Raw Materials of the Republic of Kazakhstan, Almaty, Kazakhstan.
e-mail: aliyuchca@gmail.com
ORCID: https://orcid.org/0000-0001-6098-7626

https://doi.org/10.51885/3134-7983_CATMSP_2026_2_3
SRSTI 52.45.15

OPTIMIZATION OF CRUSHING SIZE FOR HEAP LEACHING OF OXIDIZED COPPER ORE AT THE BERKARINSKOE DEPOSIT: FROM LABORATORY STUDIES TO INDUSTRIAL IMPLEMENTATION

Madina Barmenshinova [1]*, **Saltanat Beisenova** [1]
[1]K.I. Satpayev Kazakh National Research Technical University, Almaty, Kazakhstan
*Corresponding author: Madina Barmenshinova, e-mail: m.barmenshinova@satbayev.university

Keywords:
heap leaching, oxidized copper ore, Berkarinskoe deposit, crushing size optimization, percolation column tests, copper extraction, SX–EW, technological regulation.

ABSTRACT
This paper presents the results of studies on the optimization of crushing size for heap leaching of oxidized copper ore at the Berkarinskoe deposit (East Kazakhstan Region). The initial technological regulation for heap leaching was developed on the basis of comprehensive laboratory studies including chemical, phase-chemical, granulometric, mineralogical, X-ray diffraction, and thermogravimetric analyses, as well as laboratory percolation column tests on −10 mm material, which yielded copper extraction of 78.8% over 90 days. Following industrial implementation, pilot-scale column tests on −25 mm and −30 mm fractions showed that the −25 mm fraction achieves 70% copper extraction in 100 days with acid consumption of 99.4 kg/t ore (10.4 kg/kg Cu), versus 128 days and 114.7 kg/t ore (11.3 kg/kg Cu) for the −30 mm fraction. The two pilot columns were charged with different ore types — oxidized ore (K-1, −25 mm) and mixed ore (K-2, −30 mm) – which differ markedly in phase composition (9.4% versus 54.4% secondary copper sulfides), so the comparison reflects ore type as well as crushing size; this is accounted for in the interpretation. The 3.5 m columns simulated the heap height and the planned two-lift stacking. The −25 mm crushing size was identified as the optimal parameter, enabling crushing plant throughput of 90,000 t/month while maintaining extraction within regulation limits. Percolation properties remained stable throughout all tests, confirming the favorable physical characteristics of the ore. The study provides empirical, pilot-scale scale-up data linking the laboratory-based technological regulation to industrial crushing-size optimization for an operating heap leach facility.

INTRODUCTION

Heap leaching combined with the solvent extraction–electrowinning (SX–EW) process has become the dominant technology for processing oxidized copper ores worldwide, accounting for approximately 20% of global copper production and offering significant economic and environmental advantages over conventional pyrometallurgical methods (Schlesinger et al., 2022; Petersen, 2016). The efficiency of heap leaching is directly dependent on a number of ore-specific parameters, among which the crushing size plays a critical role: it determines both the accessibility of copper minerals to the leaching solution and the percolation properties of the ore bed, while simultaneously defining the capacity and energy consumption of the crushing and screening plant (Ghorbani et al., 2011; Ghorbani et al., 2016).

Particle size selection in heap leaching represents a fundamental trade-off. Finer crushing increases mineral liberation and accessibility for the leach solution, accelerating reaction kinetics and improving copper recovery; however, excessive fines can compromise heap permeability, induce channeling, and ultimately reduce extraction efficiency (Bouffard, 2008; Watling, 2006). Coarser crushing reduces capital and operating costs of comminution and improves the structural stability of the heap, but may limit copper recovery if the ore mineralogy locks copper minerals within larger particles.

The Berkarinskoe deposit, located in the East Kazakhstan Region, is an operating heap leaching facility processing oxidized copper ore with grades ranging from 0.92% to 1.52% Cu. The initial technological regulation for the operation was developed based on comprehensive laboratory investigations that provided a detailed characterization of the ore material composition and established the key leaching parameters for a crushing size of −10 mm.

However, industrial operation of the heap leaching facility revealed the need to optimize the crushing size in order to increase the throughput of the crushing and screening plant, reduce unit crushing costs, and improve the efficiency of heap construction and ore stacking. In this context, the transition to coarser crushing — specifically to −25 mm and −30 mm — was considered as a practical solution, provided that copper extraction remained within acceptable limits defined by the technological regulation.

The scientific novelty and practical significance of this work lie in the direct linkage between a laboratory-derived technological regulation and its verified industrial-scale optimization. Rather than reporting laboratory leachability alone, the study provides empirical pilot-scale data (3.5 m bed height) that quantify the trade-off between crushing-size thresholds, copper-extraction kinetics, acid consumption, and crushing-plant throughput for an operating facility — data that are rarely reported for the full laboratory-to-industry transition. Accordingly, the objectives of the study were: (i) to characterize the chemical, phase, mineralogical, and physical–mechanical properties of the Berkarinskoe oxidized ore; (ii) to establish the baseline leaching behaviour underlying the existing −10 mm regulation; and (iii) to evaluate, through pilot-scale percolation column tests that simulate the full heap height and the planned two-lift (two-tier) stacking, whether the production transition to coarser crushing — −25 mm for the oxidized ore and −30 mm for the mixed ore — preserves copper extraction within the regulation limits while increasing crushing-plant throughput.

MATERIALS AND METHODS

Deposit Characteristics and Ore Sampling

The Berkarinskoe deposit is located in the East Kazakhstan Region of Kazakhstan. The deposit contains 2,405,220 t of oxidized ore (average Cu 1.28%) and 1,687,224 t of mixed ore (average Cu 1.61%). Copper content in oxidized ores ranges from 0.92% to 1.52%. The main technological sample of oxidized ore (BR-3) used for the initial laboratory studies had a copper content of 1.23%. For the pilot-scale column tests, the two different ore types processed at the facility were used: oxidized ore (sample K-1, Cu 1.37%, crushed to −25 mm) and mixed ore (sample K-2, Cu 1.46%, crushed to −30 mm), corresponding to the production transition to coarser crushing for both ore types. The maximum lump size of run-of-mine ore from the open pit is 500 mm.

The two pilot columns were charged with the two different ore types processed at the facility: K-1 with oxidized ore and K-2 with mixed ore, each crushed to the size adopted for it in production (−25 mm and −30 mm, respectively). The samples are therefore representative of the respective ore types as they are actually fed to the heap. Because oxidized and mixed ores differ fundamentally in the ratio of oxidized copper to secondary copper sulfides, K-1 and K-2 differ markedly in phase composition (detailed below); consequently the two columns do not constitute a particle-size-controlled experiment, and this is explicitly taken into account when interpreting the comparative results.

Chemical, Phase, and Granulometric Analyses

The material composition of the oxidized ore was studied using chemical analysis, phase-chemical analysis, and granulometric analysis with copper assaying by size fraction. X-ray diffraction (XRD) analysis was performed to identify the principal crystalline phases. Thermogravimetric analysis (TGA) was used to characterize thermal stability and decomposition behavior. Physical and mechanical properties – Protod'jakonov hardness coefficient (f), abrasivity index, specific gravity, bulk density, angle of repose, and moisture capacity — were determined according to standard procedures. Percolation rates were measured through static ore beds of −5 mm, −10 mm, and −20 mm fractions.

Mineralogical Examination

To study the mineralogical composition of the copper-bearing ore, core samples with ore mineralization were selected. Petrographic and mineragraphic investigations were carried out in the physicochemical research laboratory using an OLYMPUS BX51 Pol. polarizing microscope equipped with a SIMAGIS 2P-2C video camera and SIAMS Mineral C7 image analysis software. Polished sections ("anshlif") were prepared from representative ore samples and examined in reflected light at magnifications of ×50 to ×400.

Initial Laboratory Column Leaching Tests (−10 mm)

Laboratory percolation column tests were conducted on −10 mm and −20 mm fractions (variants BR-10, BR-20, and BR-10A with acid pre-agglomeration) irrigated with dilute sulfuric acid solution over 90 days. These tests formed the basis for the development of the technological regulation for the Berkarinskoe heap leaching operation.

Pilot-Scale Column Tests for Crushing Size Optimization

Following industrial implementation of the heap leaching operation, pilot-scale column tests were initiated in September 2024. Two columns were operated in parallel: K-1 (−25 mm) and K-2 (−30 mm). Columns were fabricated from polyethylene pipe SDR17 (internal diameter 340 mm, height 4,750 mm) with an irrigation area of 0.09 m². The ore bed height was 3.5 m, chosen to simulate the full height of an industrial heap lift and to represent the planned two-lift (two-tier) stacking of the heap under the transition to coarser crushing. Leaching solution containing 25–30 g/L H_2SO_4 was applied at an irrigation density of 8–10 L/m²/h. Tests were conducted until 70% copper extraction was achieved. Pregnant leach solution (PLS) was sampled regularly to monitor copper concentration dynamics and calculate cumulative extraction and acid consumption. Leaching was conducted under ambient, atmospheric conditions with dilute sulfuric acid as the sole lixiviant; no oxidant was added and the oxidation–reduction potential (ORP) of the solutions was not monitored, because the objective of the pilot programme was to evaluate the effect of increased crushing size relative to the existing technological regulation, not to study sulfide-oxidation kinetics.

Calculation of leaching indicators. The cumulative copper extraction at a given time, ε(*t*), was calculated from the cumulative mass of copper reporting to the pregnant leach solution (PLS) up to that time, expressed as a percentage of the total copper charged to the column:

$$\varepsilon(t) = \frac{\sum ViCi}{m \cdot \beta} 100\,\% \quad (1)$$

where: ε(t) — cumulative copper extraction, %;

Vi — volume of PLS collected in interval *i*, L;

Ci— copper concentration in interval *i*, g/L;

m — mass of ore charged to the column, kg;

β — copper head grade of the ore (mass fraction, kg Cu/kg ore).

The specific acid consumption was calculated as the total mass of sulfuric acid added (corrected for the residual free acid in the PLS) divided by the mass of ore loaded (kg/t ore) and by the mass of copper extracted (kg/kg Cu):

$$\text{qore} = \frac{Aadd - Ares}{more} \quad (2)$$

$$q\text{Cu} = \frac{Aadd - Ares}{mCu} \quad (3)$$

where: A_{ad} — cumulative mass of sulfuric acid added, kg;

A_{res} — mass of residual free acid in PLS, kg;

m_{ore} — mass of ore loaded, t or kg (must be consistent with units);

m_{Cum} — mass of copper extracted, kg.

The target extraction level of 70% was adopted from the technological regulation of the Berkarinskoe operation as both the completion criterion for each pilot test and the basis for comparison between the two crushing sizes.

RESULTS AND DISCUSSION

Chemical and Phase Composition

Chemical analysis of the main oxidized ore sample (BR-3) established a copper content of 1.23%, iron 5.28%, aluminum 7.92%, silicon dioxide 59.96%, and silver 22.0 g/t (Table 1). Phase-chemical analysis showed that 83.6% of copper occurs in acid-soluble forms, of which 70.5% are readily leachable carbonates (malachite, azurite) and chalcanthite. This high proportion of acid-soluble copper forms was a key factor in confirming the suitability of the ore for sulfuric acid heap leaching and establishing the basis of the technological regulation. Notably, no acid-consuming carbonate gangue was identified in the oxidized ore, which is favorable for acid consumption management during leaching.

Table 1. Multi-element chemical analysis of ore samples, Berkarinskoe deposit

Component	Oxidized ore BR-3 (2017)	Mixed ore (2019)	Mixed ore (2021)	Unit
Cu	1.23	1.07	1.24	%
Fe	5.28	6.55	5.62	%
Al	7.92	8.46	6.88	%
SiO_2	59.96	55.86	55.76	%
Ca	1.10	1.95	2.13	%
Ag	22.0	17.4	19.6	g/t
Note – compiled by the authors				

Mineralogical Description of the Ore

The host rocks are represented by fine-clastic tuffs and acid-composition porphyries. The altered fine-clastic tuff is a pyroclastic rock of acid, moderately alkaline composition with relict or crystallo-vitrioclastic structure and massive texture. Initially, the rock appears to be an acid (subalkaline) effusive. Under higher magnification, numerous small (0.3 mm) fragments of feldspar crystals (crystalloclasts), isolated quartz crystals, devitrified glass fragments (vitroclasts), and isolated larger (up to 1–2 mm) fragments of the groundmass with trachytoid structure (litoclasts) are visible. The matrix between the pyroclastic fragments is an unindividualized quartz-feldspar aggregate with fine (0.02 mm) sericite flakes. The ore minerals present are: I — black, rare incomplete subidiomorphic crystals 0.2 mm; II — green, thin films along fragment margins; III — replaced by earthy epidote (typically after magnetite).

The altered acid porphyry with ore minerals has a fine-porphyritic structure with a felsitic to fine-felsitic groundmass. Rare fine phenocrysts (0.3–0.6 mm) consist of short prismatic and tabular alkali K-Na feldspars. The groundmass is an unindividualized microfelsitic quartz–feldspar aggregate with subordinate hydrosericite microflakes. The ore material (gray) is unevenly distributed but, at low magnification, is clearly confined to thin (0.01 mm and wider)

thread-like branching quartz veinlets. The size of ore aggregates depends directly on the thickness of these veinlets, reaching up to 1 mm. The ore minerals are completely xenomorphic – shapeless, amoeboid, lobate forms 0.01–0.8 mm in size. The ore texture is veinlet, irregularly disseminated, and nest-disseminated. Ore minerals include malachite, azurite, chalcanthite, chrysocolla, tenorite, chalcocite, and covellite. Isolated occurrences of native copper and electrum are also observed.

Malachite, azurite, chalcanthite, and chrysocolla commonly occur in association, filling fractures in the host rocks as crusts and films with thicknesses from 0.05–0.3 mm to 1 mm. Chalcanthite in rock cavities forms colloform coatings on quartz crystals, films 0.05–0.1 mm thick along fractures, and nests in cavities 2–4 mm in size with inclusions of malachite and azurite. Malachite forms fine-grained films along fractures in the rock and, less commonly, acicular aggregates 0.05–1.0 mm in size (isolated grains up to 15 mm). Azurite occurs as nests of crystals from 0.1–0.3 mm to 3×14 mm along fractures filled with chalcanthite.

Figure 1. Polished section. Crusts of azurite (blue), malachite (green), and goethite (black) along cleavage planes of the core

Note – compiled by the authors

Tenorite in intensely oxidized rocks forms veinlets with mosaic twinning structure and dendritic intergrowths when replacing chalcocite. The thickness of the veinlets is 0.02–3.0 mm. In the bulk of the host rocks, rare uneven dissemination of chalcocite is observed, with grain sizes from 0.003 to 0.05×0.075 mm, occasionally up to 0.10×0.40 mm , as well as nests composed of acicular malachite 0.3–0.5 mm in size with remnants of chalcocite and covellite.

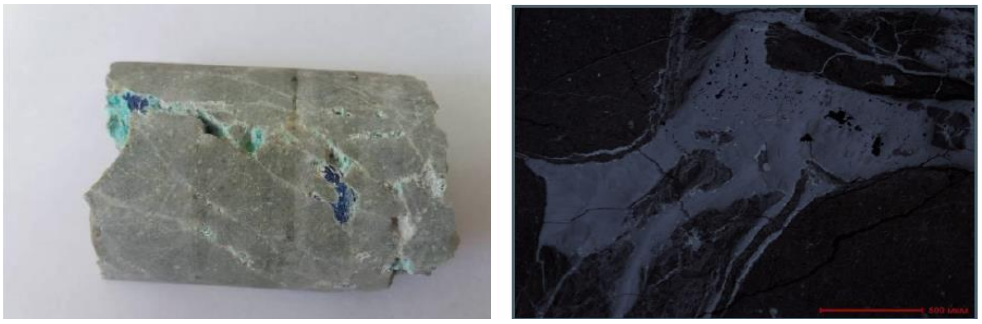

Figure 2. Polished sections: top — nests of azurite (blue) in association with chalcanthite (light blue) along fractures in the core; bottom — veinlets of tenorite with mosaic twinning structure, ×50 (scale bar 500 μm)

Isolated globules of native copper measuring 0.005×0.025–0.05 mm have been observed within iron hydroxides. Isolated inclusions of electrum measuring 0.002×0.005–0.006 mm occur within the non-ore matrix of the rock and within iron hydroxides.

The mineralogical observations are fully consistent with the phase-chemical analysis results showing 83.6% acid-soluble copper. The dominant copper-bearing minerals (malachite, azurite, chalcanthite, chrysocolla, and tenorite) are all amenable to sulfuric acid leaching at ambient temperature, while the silicate gangue (quartz, feldspar, sericite, chlorite) does not consume significant amounts of acid. Together with the absence of carbonate gangue, this mineralogical assemblage confirms the suitability of the Berkarinskoe ore for heap leaching with sulfuric acid as the lixiviant.

Physical and Mechanical Properties

The Protod'jakonov hardness coefficient is f = 8 (hard rock), abrasivity index 16 mg (below average), specific gravity 2.73 g/cm³, bulk density 1.70 g/cm³, angle of repose 29°, and moisture capacity 7.0%. These properties confirmed the ore's amenability to conventional crushing with low fines generation — a critical factor for heap percolation stability (Ghorbani et al., 2011).

Granulometric Analysis

Granulometric analysis of sample BR-3 at P93.6 = 20 mm showed that 47.7% of the ore falls in the −20+10 mm fraction (Table 2). Acid-soluble copper is uniformly distributed across all size fractions at 81–91%, confirming consistent leachability regardless of particle size. Percolation rates measured through static ore beds were 84,232 dm³/(m²·h) for minus 20 mm, 80,489 dm³/(m²·h) for minus 10 mm, and 44,924 dm³/(m²·h) for minus 5 mm material — all well above the minimum required for heap leaching.

Table 2. Copper distribution by size fraction, sample BR-3 (P93.6 = 20 mm)

Size fraction, mm	Yield, %	Cu, %	Acid-sol. Cu (rel.), %	Cu distribution, %
−30+20	6.4	0.96	83.33	5.2
−20+10	47.7	1.06	87.74	42.8
−10+5	23.6	1.30	89.23	26.0
−5+2.0	12.0	1.10	81.82	11.2
−2.0+0	10.3	—	87–90	14.8
Total	100.0	1.18	87.29	100.0
Note – compiled by the authors				

Initial Laboratory Column Tests

Laboratory percolation column tests on minus 10 mm material (variant BR-10) achieved copper extraction of 78.8% over 90 days, with projected recovery of 80–81% over 4 months. The minus 20 mm fraction (BR-20) yielded 73.6% in 90 days, with projected recovery of 76–77% over 4 months. Pre-agglomeration with acid (variant BR-10A) provided no significant improvement, confirming that agglomeration is unnecessary for this ore type given its favorable natural percolation properties (Bouffard, 2008). These results established the technological regulation for the Berkarinskoe heap leaching operation, with minus 10 mm as the design crushing size. However, following industrial implementation, operational experience demonstrated that this crushing size constrained the throughput of the crushing and screening plant and created challenges for efficient heap construction and ore stacking. This motivated the investigation of coarser crushing sizes as an operational optimization measure.

Pilot-Scale Column Tests: Crushing Size Optimization

Pilot-scale column tests were initiated in September 2024 on minus 25 mm (K-1) and minus 30 mm (K-2) fractions with ore bed height of 3.5 m (Table 3). The phase composition of the ore loaded into K-1 showed 73.8% copper in oxidized forms, 9.4% in secondary sulfides, and 16.8% as primary sulfides. The mixed ore (K-2) had a fundamentally different phase composition, with only 42.9% oxidized copper, 54.4% secondary sulfides, and 2.7% primary sulfides — a difference

inherent to the two ore types that is of central importance to the interpretation of the comparative results discussed below.

Table 3. Parameters and results of pilot-scale column leaching tests

Parameter	K-1 (−25 mm)	K-2 (−30 mm)
Ore type	Oxidized	Mixed
Ore weight, kg	448.45	465.45
Cu content, %	1.37	1.46
Oxidized Cu forms, %	73.8	42.9
Days to 70% extraction	100	128
Acid consumption, kg/t ore	99.4	114.7
Acid consumption, kg/kg Cu	10.4	11.3
Note – compiled by the authors. The "secondary copper sulfides" row was added to make the phase-composition difference between the columns explicit		

Column K-1 (−25 mm) achieved 70% copper extraction in 100 days with acid consumption of 99.4 kg/t ore (10.4 kg/kg Cu) – within the established regulation limit of 11.9 kg/kg Cu. Column K-2 (−30 mm) required 128 days with higher acid consumption of 114.7 kg/t ore (11.3 kg/kg Cu). Peak copper concentration in the PLS reached 14.5 g/L in the first days of leaching in both columns, with similar dynamics over the initial 10-day period. Beyond this point, the leaching rate of the −30 mm material (K-2) progressively lagged behind that of the −25 mm material (K-1).

This lag must not be attributed to particle size alone, because K-1 and K-2 were different ore types rather than two size splits of one sample. The dominant difference between the columns is mineralogical: whereas 73.8% of the copper in the oxidized ore (K-1) occurred in readily acid-soluble forms with only 9.4% in secondary sulfides, the mixed ore (K-2) contained only 42.9% oxidized copper and 54.4% secondary copper sulfides (chalcocite, covellite). Secondary copper sulfides dissolve far more slowly in sulfuric acid than copper carbonates and require an oxidant – ferric iron or dissolved oxygen — to leach effectively; because no oxidant was added and ORP was not controlled in these tests (see Materials and Methods), the copper hosted in secondary sulfides in K-2 could be recovered only to the limited extent of its slow, acid- and oxygen-restricted dissolution. The higher specific acid consumption of K-2 (11.3 versus 10.4 kg/kg Cu) is likewise consistent with this larger proportion of refractory sulfide copper. A particle-size effect acts in the same direction — the larger −30 mm particles present longer diffusion path lengths, as predicted by shrinking-core models for coarser material (Ghorbani et al., 2011) — but it is secondary to, and cannot be separated from, the ore-type (mineralogical) difference. Consequently the slower kinetics of K-2 reflect primarily its more refractory mixed-ore mineralogy, with coarser crushing as a contributing factor, and the present data do not allow a particle-size contribution to be isolated quantitatively.

Table 4. Cumulative copper extraction dynamics, pilot-scale column tests

Days of leaching	K-1 (−25 mm), %	K-2 (−30 mm), %
30	44	39
60	60	55
90	68	64
120	73	69
135	74	71
Note – compiled by the authors		

The oxidized ore at −25 mm (K-1) reached the target extraction faster than the mixed ore at −30 mm (K-2) across all time intervals; at day 120, extraction reached 73% for K-1 versus 69% for K-2. However, since K-1 and K-2 were different ore types crushed to different sizes, this difference cannot be read as a particle-size optimization. The practical conclusion supported by the data is that both ore types, at their respective production crushing sizes (−25 mm oxidized, −30 mm mixed), reach the 70% target within the extraction and acid-consumption limits of the technological regulation, confirming that the transition to coarser crushing and two-lift heap stacking is viable for both ore types fed to the Berkarinskoe operation.

Percolation Stability and Industrial Implications

No deterioration in percolation properties was observed in either column throughout the testing period. Bed permeability remained stable at all crushing sizes, consistent with the low clay content and low slime-forming tendency of the ore established during the initial characterization. This confirms that coarser crushing to minus 25 mm does not negatively affect heap percolation stability — a critical requirement for industrial heap leaching operations (Petersen, 2016; Watling, 2006).

The transition from −10 mm to −25 mm crushing represents a significant operational improvement: it enables an increase in crushing plant throughput to 90,000 t/month (this figure was obtained from a throughput calculation for the crushing-and-screening section, reflecting the higher capacity of the crushing circuit when producing a coarser −25 mm product instead of the original −10 mm product), reduces unit crushing energy consumption, and facilitates more efficient ore stacking and heap construction, while maintaining acid consumption within the technological regulation limit of 11.9 kg/kg Cu.

CONCLUSIONS

The initial laboratory characterization established that 83.6% of copper in the Berkarinskoe oxidized ore occurs in acid-soluble forms, predominantly readily leachable malachite, azurite, and chalcanthite. The ore exhibits favorable physical properties — low hardness (f = 8), low clay content, and stable percolation — supporting heap leaching at various crushing sizes without agglomeration.

Mineralogical examination confirmed that copper minerals are distributed as crusts, films, and nests along fractures and as fine xenomorphic grains in thin quartz veinlets. The dominant copper-bearing phases (malachite, azurite, chalcanthite, chrysocolla, tenorite) are all amenable to sulfuric acid leaching, while the silicate gangue (quartz, feldspar, sericite) does not consume significant acid.

Granulometric analysis confirmed uniform distribution of acid-soluble copper (81–91%) across all size fractions and high percolation rates, providing the physical basis for evaluating coarser crushing sizes.

Laboratory column tests on −10 mm material established baseline extraction of 78.8% over 90 days and formed the basis for the technological regulation of the Berkarinskoe heap leaching operation.

Following industrial implementation, pilot-scale column tests demonstrated that the transition from −10 mm to coarser crushing is technically justified for both ore types. For the oxidized ore at −25 mm (K-1), 70% copper extraction is achieved in 100 days with acid consumption of 99.4 kg/t ore (10.4 kg/kg Cu), within established regulation limits, while the crushing-plant throughput is increased to 90,000 t/month.

The mixed ore at −30 mm (K-2) required 128 days to reach 70% extraction with higher acid consumption (114.7 kg/t, 11.3 kg/kg Cu). Because K-2 was a different ore type — mixed ore with a substantially higher proportion of refractory secondary copper sulfides (54.4% versus 9.4%) — its slower kinetics and higher acid consumption reflect primarily its mineralogy rather than the

coarser crushing size; nonetheless it too reached the regulation target, confirming that the mixed ore is also amenable to heap leaching at −30 mm.

Percolation stability was maintained throughout all pilot-scale tests, confirming that coarser crushing to −25 mm does not negatively affect heap filtration properties. The adoption of −25 mm as the operational crushing size increases crushing plant throughput to 90,000 t/month, reduces unit crushing costs, and improves heap construction efficiency — representing a well-grounded operational optimization for the Berkarinskoe heap leaching facility.

The principal limitation of the pilot programme is that K-1 and K-2 were different ore types (oxidized and mixed) crushed to different sizes, so the column results characterize each ore type at its production crushing size rather than isolating the effect of particle size. To quantify a particle-size effect specifically, future work should compare crushing sizes on splits of a single homogenized sample of constant mineralogy, and should monitor ORP and oxidant addition to quantify the contribution of secondary-sulfide oxidation to copper recovery and acid consumption.

CONFLICT OF INTEREST: The authors declare no conflict of interest.

INSTITUTIONAL REVIEW BOARD STATEMENT: Not applicable. The study was purely technical and did not involve human participants or animals.

INFORMED CONSENT STATEMENT: Not applicable.

DATA AVAILABILITY STATEMENT: The data supporting the findings of this study are available from the corresponding author upon reasonable request.

ACKNOWLEDGEMENTS: The authors express their gratitude to the staff of the metallurgical research laboratory for the foundational laboratory studies that established the original technological regulation, and to the operations and laboratory personnel of the Berkarinskoe heap leaching facility for their support during pilot-scale testing.

REFERENCES

Bouffard, S. C. (2008). Agglomeration for heap leaching: Equipment design, agglomerate quality control, and impact on the heap leach process. Minerals Engineering, 21(15), 1115–1125. https://www.sciencedirect.com/science/article/abs/pii/S0892687508000368?via%3Dihub

Dhawan, N., Safarzadeh, M. S., Miller, J. D., Moats, M. S., Rajamani, R. K., & Lin, C.-L. (2012). Recent advances in the application of X-ray computed tomography in the analysis of heap leaching systems. Minerals Engineering, 35, 75–86. https://doi.org/10.1016/j.mineng.2012.03.033

Әділқанова, М. (2025). Усовершенствование технологии переработки окисленных медных руд месторождения Казахстана. Вестник ВКТУ им. Д. Серикбаева. https://journals.ektu.kz/vestnik/article/view/926 // Adilkanova, M. (2025). Usovershenstvovanie tekhnologii pererabotki okislennykh mednykh rud mestorozhdeniya Kazakhstana [Improvement of the technology for processing oxidized copper ores from a deposit in Kazakhstan]. Vestnik VKTU im. D. Serikbaeva [Bulletin of D. Serikbayev EKTU]. (In Russ.)

Ghorbani, Y., Becker, M., Mainza, A., Franzidis, J.-P., & Petersen, J. (2011). Large particle effects in chemical/biochemical heap leach processes: A review. Minerals Engineering, 24(11), 1172–1184. https://doi.org/10.1016/j.mineng.2011.04.002

Ghorbani, Y., Franzidis, J.-P., & Petersen, J. (2016). Heap leaching technology: Current state, innovations and future directions: A review. Mineral Processing and Extractive Metallurgy Review, 37(2), 73–119. https://doi.org/10.1080/08827508.2015.1115990

Lu, J., Dreisinger, D., & West-Sells, P. (2017). Acid curing and agglomeration for heap leaching. Hydrometallurgy, 167, 30–35. https://doi.org/10.1016/j.hydromet.2016.10.019

Petersen, J. (2016). Heap leaching as a key technology for recovery of values from low-grade ores: A brief overview. Hydrometallurgy, 165, 206–212. https://doi.org/10.1016/j.-hydromet.2016.10.022

Petersen, J., & Dixon, D. G. (2007). Modeling and optimization of heap bioleach processes. In D. E. Rawlings & D. B. Johnson (Eds.), Biomining (pp. 153–176). Springer. https://doi.org/10.1007/978-3-540-34911-2_8

Petersen, J., & Dixon, D. G. (2007). Principles, mechanisms and dynamics of chalcocite heap bioleaching. In E. R. Donati & W. Sand (Eds.), Microbial Processing of Metal Sulfides (pp. 193–218). Springer. https://doi.org/10.1007/1-4020-5589-7_10

Кенжалиев, Б.К., Койжанова, А.К., & Чепуштанова, Т.А. (2024). Инновационные методы переработки медных руд в Казахстане: комплексный подход к повышению эффективности извлечения ценных компонентов. Известия НАН РК. Серия химии и технологии. https://journals.nauka-nanrk.kz/chemistry-technology/article/view/6626/-4666 // Kenzhaliev, B.K., Koizhanova, A.K., & Chepushtanova, T.A. (2024). Innovatsionnye metody pererabotki mednykh rud v Kazakhstane: kompleksnyi podkhod k povysheniyu effektivnosti izvlecheniya tsennykh komponentov [Innovative methods for processing copper ores in Kazakhstan: An integrated approach to improving the efficiency of valuable component extraction]. Izvestiya NAN RK. Seriya khimii i tekhnologii [News of the National Academy of Sciences of the Republic of Kazakhstan. Series of Chemistry and Technology]. (In Russ.)

Watling, H. R. (2006). The bioleaching of sulphide minerals with emphasis on copper sulphides: A review. Hydrometallurgy, 84(1–2), 81–108. https://doi.org/10.1016/j.hydromet.-2006.05.001

Bartos, P.J. (2002). SX-EW copper and the technology cycle. Resources Policy, 28(3–4), 85–94. https://www.sciencedirect.com/science/article/abs/pii/S0301420703000254?via%3Dihub

Information about authors

Madina Barmenshinova – Candidate of Technical Sciences, Associate Professor, Head of the Department of Metallurgy and Mineral Processing, Kazakh National Research Technical University named after K.I. Satpayev,
e-mail: m.barmenshinova@satbayev.university,
ORCID: https://orcid.org/0000-0003-0534-2387

Saltanat Beisenova – Doctoral Student of the Department of Metallurgy and Mineral Processing, Kazakh National Research Technical University named after K.I. Satpayev,
e-mail: saltanat.beisenova97@gmail.com,
ORCID: https://orcid.org/0009-0005-0786-974X

https://doi.org/10.51885/3134-7983_CATMSP_2026_2_4
SRSTI 53.01.05

THE INFLUENCE OF SAND-RESIN MOLD FORMATION MODES ON THE QUALITY OF THE CAST

Ardak Dostayeva[1]*, **Vitaly Kulikov**[1], **Yerkebulan Nartbay**[1]
[1]Karaganda Technical University Named After Abilkas Saginov, Karaganda, Kazakhstan
Corresponding author: Dostayeva Ardak, e-mail: a.dostayeva@ktu.edu.kz

keywords:
shell mold, sand, pulverbakelite, casting, gas permeability, roughness, mixture.

ABSTRACT
When heating pulverbakelite in sand-resin mixtures during the manufacturing of shell molds, its state of aggregation changes into solid–liquid–solid form. In the process of forming a sand-resin mold, to reduce the amount of binder (pulverbakelite) in the mixture and to increase strength, along with the thermal effect, static pressure was applied that varied in accordance with changing the aggregate state of the resin. The initial pressure was 0.25 MPa, and the mixture was fed from the hopper into a model plate heated to 230 °C. After 10 seconds, pressure increased to 0.35 MPa, and after another 10 seconds it decreased to 0.2 MPa. It was experimentally established that the internal stresses of castings obtained in sand-resin molds made with the use of variable pressure were minimal and uniform. Studies also showed that such castings had a high surface purity (Rz 70-80) and no internal defects.

INTRODUCTION

Sand-resin mixtures exhibit properties characteristic of both viscous fluids and solid bodies. These mixtures constitute multiphase dispersed systems characterized by a high concentration of dispersed particles. Immediately following preparation, they consist of a solid phase (sand), resin, moisture, and air.

When a load is applied to a sand-resin mixture, the solid-phase particles (sand) coalesce as a result of the gaseous medium (air) expulsion. During the heating process, the gaseous phase becomes filled with molten resin. Under static loading, phase interaction occurs not only in response to changes in the volume of the solid phase but also in response to changes in its shape. During shape deformation, both individual solid particles and certain volumes of material undergo displacement. The gaseous phase and the molten resin serve to reduce internal friction, thereby enhancing the compaction process. The density of the mixture can be increased through the elimination of intergranular air.

As demonstrated by years of practical experience, the technology of producing molds is fundamentally based on the physicochemical and technological properties of the binders and mixtures employed. Studying these properties leads to the development of fundamentally new technological processes (Kowalczyk et al., 1995). The physicochemical processes occurring within such a dispersed medium are examined in works (Beeley, 2001; Issagulov et al., 2008; Issagulov et al., 2015; Koreniugin & Rovin, 2023; Kovaleva et al., 2017; Kulikov et al., 2025). The physical and mechanical properties that play the crucial role in the compaction of molding mixtures include compressive strength, tensile strength, shear strength, density, porosity, mass, bulk density, and moisture content. Additionally, there exists a range of significant technological

properties, such as flowability, pourability, gas permeability, compactability, and moldability. The mixture strength varies over a wide range, typically spanning from 0.04 MPa to 0.4 MPa.

Work (Dostayeva et al., 2025) examines various compositions of molding mixtures and proposes methods of enhancing their physical and mechanical properties. The interrelationship between the parameters of the molding process, the properties of the composition, and the properties of the molding mixture is demonstrated.

One of the factors that hinder the widespread adoption of resin-bonded sand casting is a relatively high cost of the binder material. The amount of binder in the mixture can be reduced by applying pressure during the heating phase of the molding process (Issagulov et al., 2008). The cost of shell molds and castings can be lowered by reducing the concentration of the expensive binder within them. This is achieved by applying static pressure while heating the mixture and forming the shell mold. Furthermore, by varying the applied pressure, it is possible to enhance the operational and mechanical properties of the shell.

The application of compression during the thermal heating of the mixture accompanied by a slight increase in pressure, the process known as "pre-pressing", facilitates the uniform distribution of the binder among the sand grains, improves grain compaction, and results in increased compressive, tensile, and flexural strength. The density of the mixture also increases due to the compaction of the sand grains and the elimination of interstitial air. This method does not require the use of coated sand mixtures, so, it entails no additional costs. Ultimately, all these factors enable reducing the binder content, thereby leading to lower casting costs.

Within both domestic and international scientific contexts, numerous studies have focused on the production of rigid, high-strength, and granular sand-resin materials (including molds, cores, briquettes, and foundations). Studies are currently underway to refine the equipment, technologies, and material compositions utilized in the manufacturing of such materials. It is well established that applying an additional load to a sand-resin mixture enhances the resulting mold strength [8].

A casting mold must possess sufficient strength to withstand external loads, such as the assembly and transport of molds and cores without cracking or fracturing, as well as internal loads resulting from the static and dynamic pressure of the molten metal during casting, along with its thermal effects. Although the sand-resin mold strength is relatively high due to chemical interactions, it is essential to establish specific processing conditions to achieve the requisite strength while minimizing the binder concentration. The mixture strength can be enhanced through the application of static loads, and the variability of this strength during the shell-curing process contributes to the overall increase in durability.

In contrast to previously published studies on resin-bonded sand molds produced under constant or variable pressure conditions, the present work focuses on the optimization of pressure variation during shell mold formation in accordance with the thermally induced phase transformation of the resin binder. The scientific contribution of the study consists in establishing a pressure–temperature processing mode that improves particle packing, enhances binder distribution uniformity, reduces binder consumption, and improves casting surface quality. Furthermore, the relationships between molding pressure, binder concentration, sand grain size distribution, strength, gas permeability, and surface roughness were quantitatively analyzed, providing a comprehensive technological basis for the production of high-quality shell molds and castings.

The scientific novelty of this study lies in the development and experimental validation of a variable-pressure shell mold formation method synchronized with the thermally induced solid–liquid–solid transformation of the resin binder. Unlike previous studies that considered the general application of pressure during shell mold production, the present work establishes an optimized pressure schedule (0.25–0.35–0.20 MPa) and evaluates its influence on mold structure,

mechanical strength, gas permeability, and casting surface quality. Furthermore, the combined effects of binder content and quartz sand fraction distribution under variable-pressure conditions were systematically investigated. The obtained results provide practical recommendations for reducing binder consumption while maintaining the required technological and mechanical properties of shell molds and ensuring the production of defect-free castings.

MATERIALS AND RESEARCH METHODS

One method of producing precision castings is casting in sand-resin molds. This method enables the production of castings with precise geometric dimensions and low surface roughness (Kowalczyk et al., 1995). Furthermore, one approach to enhancing the quality of castings produced via the shell molding method involves forming the molds under variable pressure (Koreniugin & Rovin, 2023).

When a sand-resin mixture is heated, resin liquefies at the temperature of approximately 130 °C; however, at temperatures exceeding 200 °C it undergoes irreversible solidification, that is, the resin undergoes changing its physical state. The use of shell molds significantly improves both the surface quality and the geometric accuracy of the resulting castings (Kovaleva et al., 2017).

This study utilized a device designed and manufactured based on a patented technology for the production of sand-resin molds. The device design and operating principle are predicated on the precise control of the key technological molding parameters, specifically temperature and pressure, thereby enabling the regulation of the density, strength, and thermal stability of the resulting molds.

A distinctive feature of the device design is its compatibility with interchangeable pattern plates. This capability allows for the fabrication of sand-resin molds in a wide variety of shapes and geometric dimensions, thereby ensuring the device broad applicability in experimental and laboratory research.

Despite the widespread adoption of 3D-printed plastic molds in modern manufacturing, sand-resin molds remain technologically relevant in traditional metallurgy, particularly for high-temperature casting applications and the processing of heat-resistant alloys. In this context, the proposed device serves as an effective tool for studying and optimizing metallurgical casting processes.

Prior to the commissioning of this unit, sand-resin molds were produced under laboratory conditions using manual compaction (ramming); this increased the labor intensity of the process and limited reproducibility of the resulting molds properties. The proposed unit eliminated these drawbacks, enabling the automation and stabilization of the mold-making process.

Strict safety protocols are observed during the operation of the unit. The sand-resin mixture is loaded into a dedicated hopper in the specific ratio prescribed by the proprietary technology. The control system sets the required temperature and pressure parameters, and the unit automatically forms the mixture against the pattern plate. Upon completion of the process, the upper mold lifts, and the finished sand-resin mold is extracted.

The average production time for a single mold is 3–5 minutes; this demonstrates the device high throughput and enables the production of a large volume of molds within a short timeframe under laboratory conditions. The finished molds emerge at high temperatures and emit a distinct odor resulting from the thermal decomposition of resin; therefore, additional safety precautions are observed during their extraction.

The HZ-450-B is a four-column machine featuring an open-and-closed frame design intended for the production of resin-coated sand cores (Figure 1).

The machine is capable of operating in fully automatic, single-cycle, and manual control modes. It is designed for the production of sand molds weighing no more than 6 kg.

This equipment is utilized for manufacturing cores and thin-walled sand molds using sand coated with phenolic resin.

This method proves highly effective in foundry operations where high precision, surface finish quality, and dimensional stability are critical requirements.

Figure 1. General view of sand shell molding machine HZ-450-B

Note – compiled by the authors

For each experimental condition, three specimens were prepared and tested to ensure the repeatability of the results. The values presented in the tables and figures correspond to the arithmetic mean of the measurements obtained from the tested specimens. Tensile strength and gas permeability were determined using standard laboratory methods employed in foundry practice. Surface roughness of the castings was evaluated using profilometric measurements and expressed as the roughness parameter Rz. The resulting castings were additionally subjected to visual inspection and metallographic examination to assess the presence of surface and internal defects. The repeatability of the obtained results confirmed the reliability of the experimental methodology and the observed process trends.

RESULTS AND DISCUSSION

When the sand-resin mixture is discharged from the hopper onto the pattern plate, specific initial pressure (0.25 MPa) is applied. This helps to expel excess air from the mixture and to increase the contact area between the sand grains and the powdered bakelite particles, which in turn enhances heat transfer. During formation of the powdered bakelite layer around the pattern, it is advisable to increase pressure to 0.35 MPa. As demonstrated by experiments, this ensures the establishment of strong bonds between the sand grains; resin is distributed uniformly throughout the entire mold shell and completely coats the sand particles.

Once the shell layer has cured in the region immediately adjacent to the pattern, pressure must be reduced again to prevent the sand from being forced out of the formed shell and to avoid the overall structural failure of the shell. Previously (Dostayeva et al., 2025), the optimal composition for the sand-resin mixture intended for molding using variable pressure was determined (Table 1).

The technological process was carried out as follows: after mixing, the sand-resin mixture was loaded into the machine hopper. Subsequently, the pattern plate heated to 230 °C and fitted with the casting patterns was moved into position beneath the hopper containing the mixture. At this moment, pressure of 0.25 MPa was simultaneously applied through the plate. After 10 seconds, pressure was increased to 0.35 MPa, and after further 10 seconds, it was reduced to 0.2 MPa. As a result, a shell mold with the thickness of 10–12 mm was formed. The molds were then heated at the temperature of 320–340 °C witin 2 minutes.

Table 1. The sand-resin mixture composition

No.	Parameter	Additive content, %
1	Quartz sand, fraction 0.1–0.5 mm	70
2	Quartz sand, fraction 0.4–0.9 mm	30
3	Powdered Bakelite SFP-011A	4,5 (100% and higher)
4	TS Kerosene	0,2-0,4
5	Oil thinner (white spirit)	2-3
6	Boric acid	0-0.2
Note – compiled by the authors		

To select correctly the technological parameters of the shell, it is advisable to determine their impact on stress concentration in the resulting casting, as an excessively dense and rigid mold will impede the solidification of the metal. Figure 2 illustrates a mold fabricated of a mixture of sand and resin.

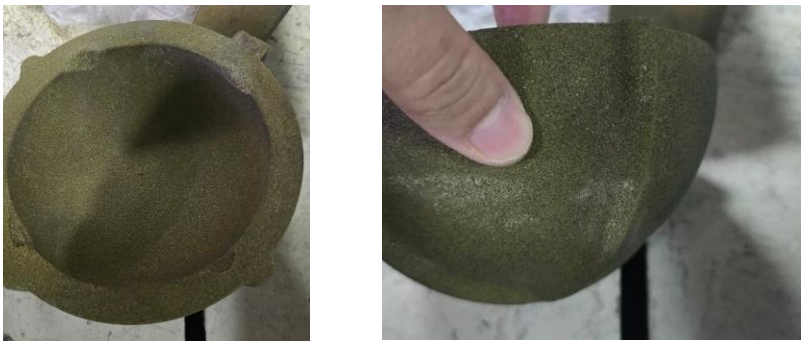

Figure 2. Molds made at the factory with the use of variable pressure
Note – compiled by the authors

It is well known that stresses are particularly dangerous during the initial stage of cooling, as the high-temperature strength of alloys is very low at this time. Furthermore, if low-melting phases form within the alloy, its strength can decrease even further. These stresses lead to the formation of hot cracks in castings.

Figure 3 (magnification ×30) illustrates the structures of a mixture of quartz sand and powdered bakelite obtained under constant pressure (a) and variable pressure (b), respectively.

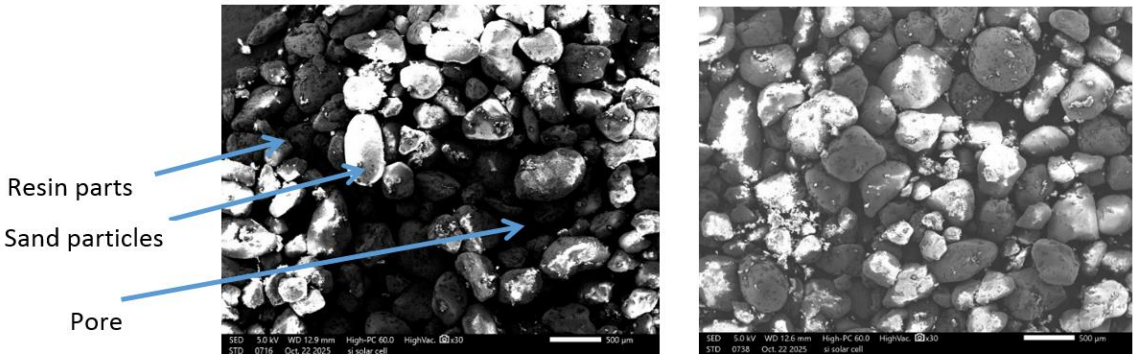

a) – with constant pressure; b) – with variable pressure
Figure 3. Compound structure, (×30) 500 µm
Note – compiled by the authors

Figure 3a reveals that the sand particles are not sufficiently densely packed, resulting in the formation of pores; moreover, the bakelite particles are distributed unevenly, which leads to insufficient strength in the mixture.

Figure 3b shows that the sand particles are packed more densely, and the frequency of contact points is significantly higher than that observed under constant pressure. Additionally, a relatively uniform distribution of the powdered bakelite particles is visually apparent. Such a structure contributes to an increase in the mechanical strength of the shell.

Table 2 presents the results of studying the powdered bakelite content effect on strength and gas permeability of sand-resin molds.

Table 2. The amount of powdered bakelite in the mixture effect on tensile strength values and gas permeability

Bakelite content in the mixture, %	Tensile strength limit, MPa	Gas permeability, un.
4	13.9	144
7	14.3	133
10	14.7	126
13	14.9	119
Note – compiled by the authors		

Table 2 demonstrates that, when utilizing this technology, the binder content exceeding 4–7% has a negligible effect on increasing strength. However, gas permeability remains within the technologically required limits across all the binder concentrations employed.

The dependence of tensile strength on the binder content is illustrated in Figure 4. In the experiments, the amount of binder (bakelite powder) in the mixture varied from 1% to 7%. The formation of the shell mold was carried out under pressure of 0.25 MPa applied to the mixture throughout the entire molding period; initial pressure was 0.25 MPa and was increased to 0.32 MPa and subsequently decreased to 0.2 MPa by the end of the molding process.

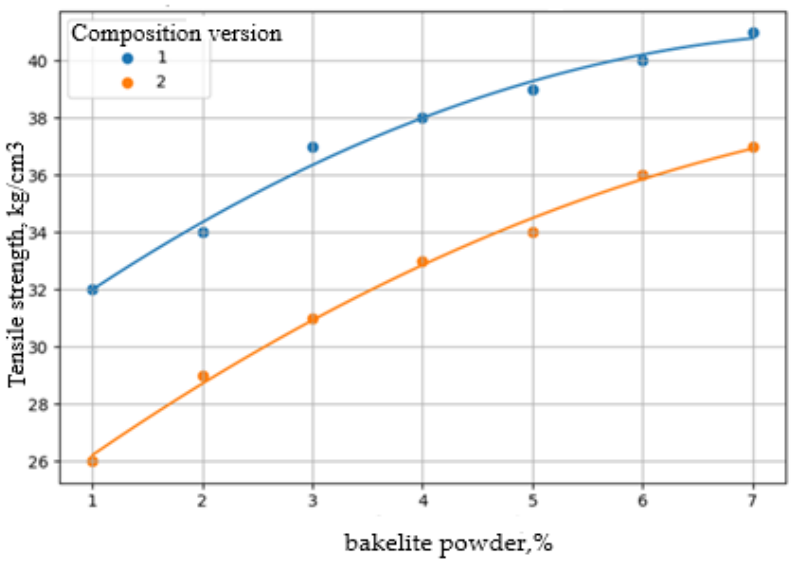

1 – composition obtained under variable pressure during the molding process;
2 – constant pressure during the molding process

Figure 4. Tensile strength dependence on bakelite powder content

Note – compiled by the authors

It is evident that, with the technology employed here, the a binder content of 4–7% is sufficient to achieve the required technological properties of the mixture. Naturally, using the minimal amount of binder in the mixture does not result in sufficient adhesion and homogeneity among its components to withstand the pouring of molten metal into the mold. Conversely, a higher binder content is inadvisable, as it yields no improvement in the mold performance characteristics while simultaneously increases its production cost. The bakelite powder content exceeding 7–8% leads to the formation of an excessive liquid phase, which ultimately compromises the structural integrity of the system.

A study was conducted on the effect of quartz sand of different fractions on the strength and gas permeability of the mixture (Table 3).

Table 3. Strength and gas permeability of the quartz sand and fraction 0.1–0.5 mm and 0.4–0.9 mm mixture in different proportions

Quartz sand and fraction 0.1–0.5 mm and 0.4–0.9 mm mixture in different proportions	Tensile strength, MPa	Gas permeability, un.
100:0	12.5	148
30:70	11.9	111
70:30	14.6	129
0:100	10.7	102
Note – compiled by the authors		

The most optimal solution proved to be the use of quartz sand composed of two fractions: 70% coarse sand and 30% fine sand. The ratio of sand fractions in the mixture (0.1–0.5 mm and 0.4–0.9 mm) was assessed based on strength and gas permeability. The content of Bakelite powder was maintained constant at 7%.

The optimal ratio of sand fractions is characterized by the densest arrangement of particles and the greatest number of contact points. In this case, the mixture gas permeability is maintained at the level that meets technological requirements (approximately 100 units). This result is explained by the uniform compaction of the sand-resin mixture and its effective gas permeability.

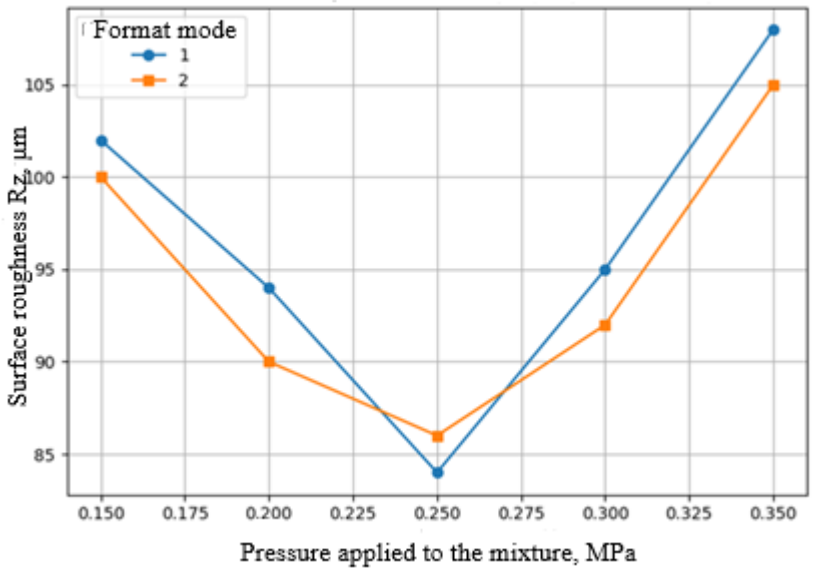

Figure 5. Pressure impact in the film surface roughness

Note – compiled by the authors

The dependence of casting surface roughness on the pressure acting on the mixture is shown in Figure 5. Experimental data indicate that the optimal value is reference pressure of 0.25 MPa. Pressures below this value lead to decreasing the mold strength due to insufficient compaction, while higher pressures cause thermal combustion of the bakelite powder and extrusion of sand particles. As a result, the mechanical strength of the mold decreases and the surface roughness increases, which contributes to crack formation in the hardened mixture.

The effect of alternating pressure on the surface quality of the mixture was also studied. Reference pressure was maintained at 0.25 MPa, with pressure changes occurring every 10–12 seconds, and the total molding time was 35 seconds. Experiments showed that using alternating pressure significantly improved the surface quality of the casting. In this case, the mold surface is formed as smooth as possible, since the surface sand layer is compacted to the boundary of the molten resin which ensures the formation of uniform and smooth zones.

Thus, it can be concluded that the use of variable static pressure in the molding process improves the adhesion between components, increases strength, homogeneity and stability of the resulting mold, which improves the physical and mechanical properties of the entire molding mixture.

The assessment of casting quality was based on a combination of visual inspection, metallographic examination, and comparative analysis of defect formation tendencies in castings produced under different molding conditions. Particular attention was paid to the occurrence of surface cracks, internal discontinuities, and other casting defects associated with excessive mold rigidity and non-uniform cooling conditions. Castings produced in molds formed under variable-pressure conditions demonstrated a lower tendency toward defect formation and exhibited a more uniform microstructural appearance. Therefore, the term “minimal and uniform internal stresses” used in this study refers to the reduced likelihood of stress-related casting defects observed during experimental evaluation.

CONCLUSION

This study substantiated the effectiveness of using static pressure that varied depending on the resin state of aggregation, taking into account the characteristics of the solid-liquid-solid transition of the bakelite powder upon heating during the formation of film sand-resin molds. A pressure curve was chosen as the process mode, in which the model plate temperature was 230 °C, Initial pressure: 0.25 MPa; after 10 s increased to 0.35 MPa; after another 10 s reduced to 0.20 MPa. This mode resulted in the stable formation of a film mold 10–12 mm thick, which then completely hardened upon additional heating at 320–340 °C within 2 minutes.

Structural analysis showed that when applying variable pressure, the mechanical properties of the mold were improved due to the dense arrangement of sand grains, the increased frequency of contact points, and the uniform distribution of bakelite particles. This in turn helps maintain internal stresses in the castings at the minimal and uniform level, reducing the risk of hot cracking. Furthermore, the surface quality of the resulting castings was high, characterized by the roughness of Rz 70–80 and the absence of internal defects.

As a result of assessing the effect of the amount of bakelite powder on the properties of the mixture, it was found that the range of 4–7% was optimal from the technological standpoint: within that range, strength indicators were maintained at a sufficient level, and gas permeability met technological requirements with all the concentrations. It was shown that with bakelite powder amounts greater than 7–8%, there was a high probability of excess liquid phase formation, which reduced strength of the system and led to economic inefficiency.

Experiments to optimize the particle size distribution of sand grains confirmed the advantages of combining the two fractions. The most effective result was observed with the ratio of 0.1–0.5 mm:0.4–0.9 mm = 70:30. In this case, the sand particles were packed most densely, the

number of contacts increased, and gas permeability remained within technological limits. Overall, the use of variable pressure improves strength, uniformity, and mold stability by reducing the amount of binder and is recommended as an effective technological method of producing high-quality, defect-free castings in shell molds.

CONFLICT OF INTEREST. The authors declare no conflict of interest.

FUNDING. This study was carried out within the framework of grant AP26103581 "Developing and studying a cost-effective technology of producing precision castings in sand-resin molds obtained by using variable static pressure" of the Science Committee of the Ministry of Higher Education and Science of the Republic of Kazakhstan.

REFERENCES

Beeley, P. (2001). Foundry technology. 2nd ed. Oxford: Butterworth-Heinemann, 443–546. https://doi.org/10.1016/B978-075064567-6/50011-X

Dostayeva, A., Kulikov, V., Baibekov, Sh., Kovalev, P., Kvon, Sv., Issagulov, A., Arinova, S., & Kovaleva, T. (2025). Studying foundry resin-bonded sand molds made with the use of variable pressure. Acta Metallurgica Slovaca, 31(3), 149–155. https://doi.org/10.36547/ams.31.3.2223

Исагулов, А.З., Куликов, В.Ю., Щербакова, Е.П., & Ковалева, Т.В. (2015). Повышение качества отливок при литье в песчано-смоляные формы. Вена: East-West, 188 с. // Issagulov, A. Z., Kulikov, V. Yu., Shcherbakova, E. P., & Kovaleva, T. V. (2015). Povyshenie kachestva otlivok pri lit'e v peschano-smolyanye formy [Improving the quality of castings when casting in sand-resin molds]. Vienna: East-West, 188 p. (In Russ.)

Исагулов, А. З., Максимов, Е. В., Куликов, В. Ю., & Воропаева, О. Ю. (2008). Напряжение ползучести песчано-смоляной смеси в условиях чистого сжатия и сдвига. Известия вузов. Черная металлургия, 8, 33–36. // Issagulov, A. Z., Maksimov, E. V., Kulikov, V. Yu., & Voropayeva, O. Yu. (2008). Napryazhenie polzuchesti peschano-smolyanoj smesi v usloviyakh chistogo szhatiya i sdviga [Creep stress of a sand-resin mixture under conditions of pure compression and shear]. Izvestiya vuzov. Chernaya metallurgiya, 8, 33–36. (In Russ.)

Коренюгин, С.В., & Ровин, С.Л. (2023). Литье и металлургия, 3, 36–40. https://doi.org/10.21122/16836065202333640 // Koreniugin, S.V., & Rovin, S.L. (2023). Lit'e i metallurgiya [Foundry production and metallurgy], 3, 36–40. https://doi.org/10.21122/16836065202333640 (In Russ.)

Kovaleva, T., Yeremin, E., Arinova, S., Medvedeva, I., & Dostayeva, A. (2017). Enhancing surface roughness of castings when sand-resin mold casting. Metalurgija, 56(1–2), 135–138.

Kowalczyk, J., Mroz, W., Warczok, A., & Utigard, T.A. (1995). Viscosity of copper slags from chalcocite concentrate smelting. Metallurgical and Materials Transactions B, 26, 1217–1223. https://doi.org/10.1007/BF02654007

Куликов, В.Ю., Исагулов, А.З., Достаева, А.М., & Байбеков, Ш.С. (2025). Разработка и внедрение производства песчано-смоляных форм при нестабильном давлении с целью повышения качества готовой продукции: монография. Караганда: Издательство Карагандинского технического университета, 150 с. ISBN 978-601-355-587-4 // Kulikov, V. Yu., Issagulov, A. Z., Dostayeva, A. M., & Baybekov, Sh. S. (2025). Razrabotka i vnedrenie proizvodstva peschano-smolyanykh form pri nestabil'nom davlenii s tsel'yu povysheniya kachestva gotovoj produktsii: monografiya [Development and implementation of the production of sand-resin molds under unstable pressure in order to improve the quality of the finished product: Monograph]. Karaganda: Publishing House of Karaganda Technical University, 150 p. ISBN 978-601-355-587-4 (In Russ.)

Information of the authors

Dostayeva Ardak Mukhamediyevna – PhD, Professor, Abylkas Saginov Karaganda Technical University NJSC, Karaganda, Kazakhstan,
e-mail: a.dostayeva@ktu.edu.kz,
ORCID: https://orcid.org/0000-0002-1982-2368,

Kulikov Vitaly Yuryevich – Candidate of Technical Sciences, Professor, Abylkas Saginov Karaganda Technical University NJSC, Karaganda, Kazakhstan,
e-mail: v.kulikov@ktu.edu.kz,
ORCID: https://orcid.org/0000-0001-6191-8569

Nartbai Yerkebulan Zhanbolatuly – Engineer, Abylkas Saginov Karaganda Technical University NJSC, Karaganda, Kazakhstan,
e-mail: e.nartbay@ktu.edu.kz

https://doi.org/10.51885/3134-7983_CATMSP_2026_2_5
SRSTI 52.45.19

IMPROVING THE QUALITY OF PB–ZN CONCENTRATE BY SODIUM SILICATE ADDITION DURING FLOTATION OF OXIDIZED ORE FROM THE KOSHKUDUK DEPOSIT

Alima Mambetaliyeva [1], **Guldana Makasheva** [1]*, **Tansholpan Tussupbekova** [1], **Alemgul Tanabayeva** [1]
[1]K.I. Satpayev Kazakh National Research Technical University, Almaty, Kazakhstan
*Corresponding author: Guldana Makasheva, e-mail: mguldanka@mail.ru

Keywords:
oxidized lead–zinc ore; flotation; sodium silicate; calcium polysulfide; depressant; concentrate quality; Koshkuduk.

ABSTRACT

The processing of oxidized lead–zinc ores is complicated by the hydrophilic surface of valuable minerals, fine dissemination, and the significant presence of silicate and slime components, which reduce flotation selectivity and concentrate quality. This study aimed to improve the quality of a lead–zinc concentrate obtained from oxidized ore of the Koshkuduk deposit by optimizing the dosage of sodium silicate (Na_2SiO_3) during flotation after preliminary sulfidization with calcium polysulfide. Laboratory flotation tests were carried out using sodium silicate dosages ranging from 0 to 500 g/t. The process performance was evaluated based on concentrate yield, Pb, Zn, and Ag grades, recoveries, the Hancock–Luyken separation efficiency criterion, and an additional separation criterion. Without sodium silicate, the concentrate yield was 7.20 %, with Pb, Zn, and Ag grades of 3.78 %, 3.15 %, and 50.03 g/t, respectively. The optimal Na_2SiO_3 dosage was 170 g/t, at which the concentrate yield decreased to 3.62 %, while Pb, Zn, and Ag grades increased to 8.58 %, 6.44 %, and 100.46 g/t, respectively. The corresponding recoveries were 53.56 % Pb, 41.64 % Zn, and 66.12 % Ag. Further increasing the Na_2SiO_3 dosage to 200–500 g/t did not improve flotation performance. The results demonstrate that sodium silicate effectively improves concentrate quality by depressing silicate and slime minerals in oxidized lead–zinc ore flotation.

INTRODUCTION

The gradual depletion of high-grade sulfide ores has increased the need to involve oxidized and mixed lead–zinc ores in mineral processing. These ores are generally characterized by complex mineral composition, high oxidation degree of valuable minerals, fine dissemination, and a significant proportion of silicate, carbonate, and clay minerals (Nayak et al., 2022; Liu et al., 2020; Maghfouri et al., 2018). In contrast to sulfide minerals, oxidized lead and zinc minerals have more hydrophilic surfaces, which makes their direct flotation difficult and reduces the selectivity of separation (Yi et al., 2022; Elizondo-Álvarez et al., 2020; Xue et al., 2023; Zhang et al., 2022).

One of the main technological problems in the flotation of oxidized lead–zinc ores is the production of a concentrate with acceptable quality. Even when the recovery of valuable components is sufficient, the concentrate may be contaminated by gangue minerals, fine slimes, iron-bearing phases, and silicate components. This reduces the grade of lead, zinc, and associated precious metals in the concentrate and may negatively affect subsequent metallurgical processing (Zuo et al., 2020; Bai et al., 2020; Zheng et al., 2018; Ge et al., 2020).

A widely used approach to improve the floatability of oxidized minerals is preliminary sulfidization of their surface. During treatment with sulfidizing reagents, a sulfide-like layer can form on the surface of oxidized minerals, promoting the adsorption of sulfhydryl collectors and increasing particle hydrophobicity (Ke et al., 2018; Li et al., 2017; Li et al., 2014). However, the use of conventional sodium sulfide does not always provide stable results. Excess sulfide ions may depress valuable minerals, while the formed surface compounds may be unstable under flotation conditions (Luo et al., 2023; Zhang et al., 2022; Zhao et al., 2022).

In recent years, increasing attention has been paid to alternative sulfidizing reagents and combined reagent regimes. For oxidized lead–zinc ore from the Koshkuduk deposit, the effectiveness of calcium polysulfide (CaS_x) has previously been demonstrated. Calcium polysulfide provides more stable sulfidization of oxidized mineral surfaces and improves the conditions for collector adsorption (Mambetaliyeva et al., 2026). However, the selection of an effective sulfidizing agent alone is not always sufficient to obtain a high-quality concentrate, because a significant part of the loss of selectivity is associated with the entrainment of silicate and slime particles into the froth product.

To regulate flotation selectivity, depressants and dispersants of gangue minerals are widely used. Sodium silicate (Na_2SiO_3), also known as water glass, is one of the most common reagents used for depressing silicate, carbonate, and calcium-bearing minerals and for reducing the negative effect of fine slimes (Wang et al., 2024; Ni et al., 2025; Silva et al., 2012). In aqueous solutions, sodium silicate undergoes hydrolysis with the formation of silicate and polysilicic species that can adsorb on the surface of gangue minerals, increasing their hydrophilicity and preventing collector attachment (Wang et al., 2024; Silva et al., 2012). As a result, Na_2SiO_3 can reduce concentrate yield, decrease gangue contamination, and increase the grade of valuable components.

The use of sodium silicate is particularly important for complex oxidized ores in which valuable minerals are associated with quartz, aluminosilicates, carbonates, and iron-bearing phases. In such systems, Na_2SiO_3 may perform a dual function: it depresses gangue minerals and stabilizes the dispersed state of the pulp, reducing mechanical slime entrainment into the froth product (Wang et al., 2024; Ni et al., 2025; Silva et al., 2012; Marinakis & Shergold, 1985). However, the efficiency of sodium silicate strongly depends on its dosage. Insufficient reagent addition may not provide adequate gangue depression, whereas excessive dosages may reduce the floatability of sulfidized valuable minerals and decrease recovery.

Despite numerous studies on the sulfidization of oxidized lead–zinc minerals, the improvement of concentrate quality through sodium silicate dosage optimization in the presence of calcium polysulfide remains insufficiently studied. This issue is especially relevant for the Koshkuduk deposit, where the ore is characterized by a high degree of oxidation, fine mineral dissemination, and a considerable silicate component (Mambetaliyeva et al., 2026; Chepushtanova et al., 2022).

The scientific novelty of this study lies in the optimization of sodium silicate dosage for oxidized Pb–Zn ore from the Koshkuduk deposit after preliminary sulfidization with calcium polysulfide. In contrast to previous studies that mainly considered conventional sulfidization or the general depressing effect of sodium silicate on gangue minerals, this work evaluates the combined reagent regime of calcium polysulfide and Na_2SiO_3 under controlled flotation conditions. In addition, the study identifies the rational Na_2SiO_3 dosage and determines the dosage range at which further reagent addition does not improve concentrate quality and may partially depress valuable minerals.

The aim of this study is to investigate the effect of sodium silicate dosage on the flotation performance of oxidized lead–zinc ore from the Koshkuduk deposit after preliminary sulfidization with calcium polysulfide. Particular attention is paid to improving concentrate

quality, reducing froth product yield, increasing Pb, Zn, and Ag grades, and evaluating the recovery and separation efficiency of valuable components.

MATERIALS AND METHODS

The chemical composition of the oxidized polymetallic ore sample from the Koshkuduk deposit was determined using conventional silicate chemical analysis. The contents of gold and silver were measured by fire assay analysis, while the elemental composition of the sample was established by inductively coupled plasma mass spectrometry (ICP-MS). Phase composition was carried out in reflected light on polished sections using an OLYMPUS BX 53 microscope equipped with a SIMAGIS XS-3CU video camera and Mineral C7 image analysis software (SIAMS).

The chemical composition of the polymetallic ore sample is shown in Figure 1.

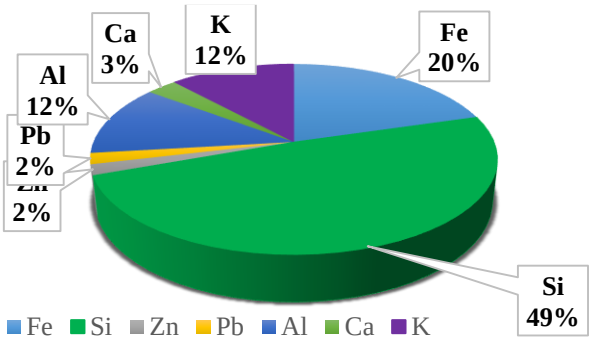

Figure 1. Chemical composition of the polymetallic ore

Note – compiled by the authors

As shown in Figure 1, the ore contains 0.58 wt.% Pb and 0.56 wt.% Zn. The copper content is low (0.02 wt.%) and does not represent industrial interest. At the same time, the ore contains a noticeable amount of precious metals, with gold at approximately 0.6 g/t and silver at 5.5 g/t.

To assess the processability of the ore, a chemical phase analysis of lead, zinc and iron was carried out. The results are presented in Table 1.

Table 1. Results of chemical phase analysis of the oxidized ore from the Koshkuduk deposit

Component forms	Content, wt.% (absolute)	Content, % (relative)
Zinc occurrence forms:		
Water-soluble	< 0.05	-
Oxidized	0.31	55.36
Sulfide	0.07	12.50
Sparingly soluble	0.18	32.14
Total Zn	0.56	100.0
Lead occurrence forms:		
Oxygen-containing	0.29	50.00
Galena	0.13	22.41
Residual forms	0.16	27.59
Total Pb	0.58	100.0
Iron occurrence forms:		
Sulfide	< 0.05	-
Ferrous iron (Fe^{2+})	3.06	48.6
Ferric iron (Fe^{3+})	3.24	51.4
Total Fe	6.30	100.0
Note – compiled by the authors		

The data in Table 1 indicate that the studied ore belongs to the oxidized type. Lead is present in oxidized and silicate forms at 77.59 % (relative). While zinc occurs predominantly in oxidized forms at 87.5 % (relative). Iron is also almost entirely oxidized, as the content of sulfide iron forms does not exceed 0.05 % (absolute).

Mineralogical analysis showed that the ore minerals are mainly represented by fahlores, chalcocite, covellite, goethite, and hematite. Sulfide minerals such as chalcopyrite, galena, pyrite and sphalerite are also present. The mineral aggregates from disseminated and vein-disseminated textures as well as replacement structures. A characteristic feature of the ore is the fine dissemination of minerals (0.005-0.015 mm) and the intensive development of oxidation and replacement processes, with sulfide minerals being replaced by goethite and hematite (Figure 2).

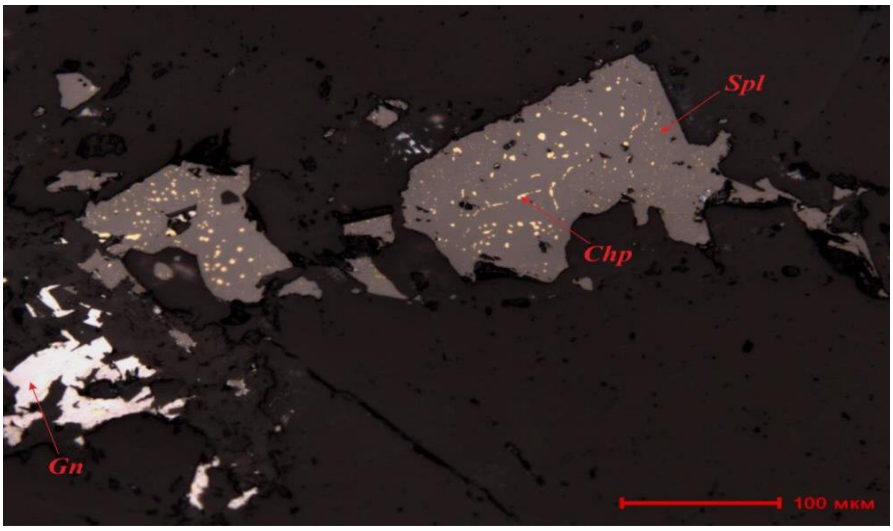

Figure 2. Polished section. Inclusions of chalcopyrite (Chp) in sphalerite (Spl) and galena (Cn) in quartz. Magnification x 200

Note – compiled by the authors

The mineralogical characteristics of the ore and its beneficiation products are further complicated by the presence of finely dispersed ore minerals, clayey material, and extensive replacement of sulfide minerals by their oxidized forms. As a result, particles of sulfide minerals potentially suitable for liberation and subsequent recovery are reduced to sizes of 5 μm or less.

The particle size distribution and the distribution of chemical elements across size fractions are presented in Table 2.

Table 2. Results of sieve analysis

Particle size class, mm	Yield, %	Grade, %, g/t*				Distribution, %			
		Zn	Pb	Fe	Ag*	Zn	Pb	Fe	Ag
-1+0.5 mm	26.46	0.37	0.30	5.83	4.26	17.88	13.80	24.70	20.7
-0.5+0.2 mm	19.90	0.51	0.48	6.21	4.79	18.62	16.62	19.77	17.5
-0.2+0.1 mm	32.89	0.54	0.55	5.92	5.17	32.51	31.90	31.14	31.21
-0.1+0.071 mm	9.49	0.73	0.91	6.90	9.27	12.55	15.13	10.48	16.14
-0.071+0.045 mm	3.31	0.83	1.06	7.43	7.00	5.00	6.16	3.93	4.25
-0.045+0 mm	7.96	0.93	1.17	7.84	6.99	13.43	16.39	9.98	10.2
Total:	100.0	0.56	0.58	6.31	5.50	100.0	100.0	100.0	100.0
Note – compiled by the authors									

The sieve analysis results show that the largest proportion of material is concentrated in the −0.2 +0.1 mm size fraction (32.89 %), while the fine fraction −0.045 +0 mm accounts for 7.96 %. Lead and zinc are predominantly concentrated in the finer size fractions, particularly in the −0.045 +0 mm fraction, where their contents reach 1.17 wt.% Pb and 0.93 wt.% Zn, respectively. The main distribution of lead and silver is observed in the −0.2 +0.1 mm size fraction.

Flotation experiments were carried out using a laboratory pneumatic–mechanical flotation machine VEKTIS with a cell volume of 3 L. Prior to flotation, a 1 kg ore sample with a particle size of −2+0 mm was ground in a laboratory ball mill MShL-7 under wet conditions. Grinding was performed at a pulp solids content of 60 % for 10 min, which provided a grinding fineness of 68.54 % of the −0.071 mm size fraction.

After grinding, the pulp was transferred to the flotation cell and diluted to a solids content of 30 % by mass. The flotation tests were conducted at a pulp temperature of 26 °C. Pulp mixing was carried out using an impeller speed of 1700 rpm. Air was supplied to the flotation zone at a pressure of not less than 5 bar, with an air flow rate of up to 10 NL/min. The froth product was removed using a froth scraper at a rotation speed of 3 rps.

The reagents were added sequentially with preliminary pulp conditioning. At the first stage, calcium polysulfide was introduced into the pulp as a sulfidizing agent to activate the surface of oxidized lead and zinc minerals. Then, sodium silicate (Na_2SiO_3) was added as a depressant of silicate and slime minerals. The dosage of Na_2SiO_3 was varied from 0 to 500 g/t to evaluate its effect on concentrate quality and flotation selectivity. Potassium butyl xanthate was used as the main collector at a dosage of 150 g/t, followed by the addition of T80 frother at 60 g/t and Aero 3418 collector at 60 g/t. The total conditioning time before flotation was 3 min. Main flotation was carried out for 10 min, followed by cleaner flotation for 6 min. The obtained products were filtered, dried, weighed, and analyzed for Pb, Zn, Ag, and Fe contents. Based on the analytical results, the yield, grade, and recovery of valuable components were calculated.

Additional confirmatory flotation tests were carried out for the optimal reagent regime in order to verify the reproducibility of the obtained results. Since the variation between repeated tests was small, Table 3 presents the results of the main laboratory tests for each sodium silicate dosage, while the repeated tests were used only to confirm the stability of the optimal Na_2SiO_3 dosage.

RESULTS

Based on the chemical, phase, mineralogical, and granulometric analyses, the oxidized lead–zinc ore from the Koshkuduk deposit can be classified as a refractory raw material. This is associated with the high oxidation degree of lead and zinc minerals, fine dissemination of ore minerals, and the significant presence of silicate and slime components. These features require the use of a combined reagent regime involving preliminary sulfidization of oxidized mineral surfaces followed by the depression of gangue minerals.

The scheme of the laboratory flotation tests is shown in Figure 3. It includes rougher flotation and a cleaner stage, which makes it possible to evaluate the effect of sodium silicate (Na_2SiO_3) not only on the recovery of valuable components but also on the quality of the resulting lead–zinc concentrate.

The results of the experiments evaluating the effect of sodium silicate dosage on flotation performance are presented in Table 3.

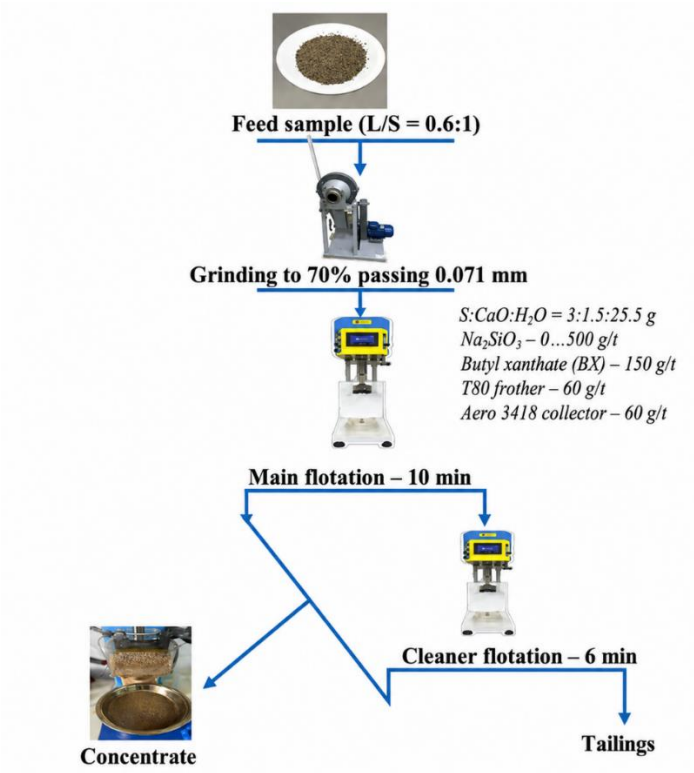

Figure 3. Technological scheme of laboratory flotation tests

Table 3. Effect of sodium silicate (Na_2SiO_3) dosage on the flotation performance of oxidized lead–zinc ore

Reagent dosage, g/t	Product	Yield, %	Grade, %, g/t*				Recovery, %			
			Pb	Zn	Ag*	Fe	Pb	Zn	Ag	Fe
Base test										
Na_2SiO_3 - 0	Concentrate	7.2	3.78	3.15	50.03	2.72	46.9	40.54	65.5	3.1
	Tailings	92.8	0.33	0.36	2.04	6.59	53.1	59.46	34.5	96.9
	Feed (initial sample)	100.0	0.58	0.56	5.50	6.31	100.0	100.0	100.0	100.0
Test 1										
Na_2SiO_3 - 30	Concentrate	4.34	6.04	5.33	78.74	5.68	45.2	41.3	62.1	3.9
	Tailings	95.66	0.33	0.34	2.18	6.34	54.8	58.7	37.9	96.1
	Feed (initial sample)	100.0	0.58	0.56	5.50	6.31	100.0	100.0	100.0	100.0
Test 2										
Na_2SiO_3 - 50	Concentrate	4.21	6.02	5.49	77.24	6.74	43.7	41.24	59.12	4.5
	Tailings	95.79	0.34	0.34	2.35	6.29	56.3	58.76	40.88	95.5
	Feed (initial sample)	100.0	0.58	0.56	5.50	6.31	100.0	100.0	100.0	100.0
Test 3										
Na_2SiO_3 - 70	Concentrate	4.19	6.19	5.47	80.24	6.66	44.7	41.0	61.1	4.4
	Tailings	95.81	0.33	0.35	2.23	6.29	55.3	59.1	38.9	95.6
	Feed (initial sample)	100.0	0.58	0.56	5.50	6.31	100.0	100.0	100.0	100.0
Test 4										
Na_2SiO_3 - 100	Concentrate	4.07	6.43	5.43	83.12	6.00	45.1	39.5	61.5	3.87
	Tailings	95.93	0.33	0.35	2.21	6.32	54.9	60.6	38.5	96.1

Reagent dosage, g/t	Product	Yield, %	Grade, %, g/t*				Recovery, %			
			Pb	Zn	Ag*	Fe	Pb	Zn	Ag	Fe
	Feed (initial sample)	100.0	0.58	0.56	5.50	6.31	100.0	100.0	100.0	100.0
Test 5										
Na_2SiO_3 - 120	Concentrate	3.91	7.20	5.88	87.63	6.62	48.51	41.04	62.3	4.1
	Tailings	96.09	0.31	0.34	2.16	6.30	51.49	58.96	37.7	95.9
	Feed (initial sample)	100.0	0.58	0.56	5.50	6.31	100.0	100.0	100.0	100.0
Test 6										
Na_2SiO_3 - 150	Concentrate	3.84	7.57	6.02	91.81	7.13	50.1	41.3	64.1	4.3
	Tailings	96.16	0.30	0.34	2.05	6.28	49.9	58.7	35.9	95.7
	Feed (initial sample)	100.0	0.58	0.56	5.50	6.31	100.0	100.0	100.0	100.0
Test 7										
Na_2SiO_3 - 170	Concentrate	3.62	8.58	6.44	100.46	6.97	53.56	41.64	66.12	4.0
	Tailings	96.38	0.28	0.34	1.93	6.29	46.44	58.36	33.88	96.0
	Feed (initial sample)	100.0	0.58	0.56	5.50	6.31	100.0	100.0	100.0	100.0
Test 8										
Na_2SiO_3 - 200	Concentrate	3.95	7.71	5.68	89.50	6.58	52.5	40.0	64.3	4.1
	Tailings	96.05	0.29	0.35	2.05	6.30	47.5	60.0	35.7	95.9
	Feed (initial sample)	100.0	0.58	0.56	5.50	6.31	100.0	100.0	100.0	100.0
Test 9										
Na_2SiO_3 - 500	Concentrate	4.01	7.41	5.62	88.05	5.66	51.23	40.24	64.2	3.6
	Tailings	95.99	0.29	0.35	2.05	6.34	48.77	59.76	35.8	96.4
	Feed (initial sample)	100.0	0.58	0.56	5.50	6.31	100.0	100.0	100.0	100.0

Note – compiled by the authors

To provide a clearer visualization of the effect of sodium silicate dosage on the recovery of valuable components, the recovery values of Pb, Zn, and Ag were plotted as a function of Na_2SiO_3 dosage. The obtained dependence is presented in Figure 4.

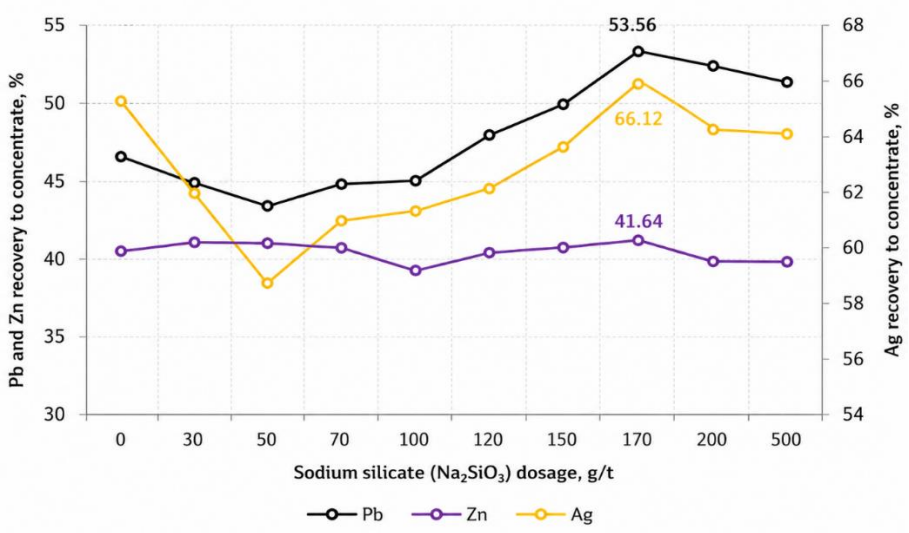

Figure 4. Effect of sodium silicate (Na_2SiO_3) dosage on Pb, Zn and Ag recovery into the concentrate

Note – compiled by the authors

As shown in Figure 4, the addition of sodium silicate (Na_2SiO_3) had different effects on the recovery of lead, zinc, and silver. In the base test without Na_2SiO_3, the recoveries of Pb, Zn, and Ag were 46.90 %, 40.54 %, and 65.50 %, respectively. When the Na_2SiO_3 dosage was increased to 170 g/t, Pb recovery increased to 53.56 %, Zn recovery to 41.64 %, and Ag recovery to 66.12 %. Thus, the highest recovery values for the valuable components were obtained at a sodium silicate dosage of 170 g/t.

A further increase in Na_2SiO_3 dosage to 200–500 g/t did not improve recovery. At 500 g/t, Pb recovery decreased to 51.23 %, Zn recovery to 40.24 %, and Ag recovery to 64.20 %. This indicates that an excess of sodium silicate may have a depressant effect not only on gangue minerals but also partially on sulfidized lead and zinc minerals. Therefore, a Na_2SiO_3 dosage of 170 g/t can be considered rational in terms of combining relatively high Pb, Zn, and Ag recoveries with improved concentrate quality.

In addition to conventional flotation indicators, such as product yield, grade, and recovery of valuable components, the Hancock–Luyken criterion was used to provide a more comprehensive assessment of separation selectivity. This criterion takes into account not only the recovery of the valuable component into the concentrate but also its losses in the tailings and the concentrate yield.

The Hancock-Luyken criterion was calculated using the following equation:

$$E = \frac{\varepsilon - \gamma}{1 - \alpha}$$

where ε is the recovery of the valuable component in the concentrate;

γ is the recovery of the valuable component in the tailings;

α is the concentrate yield.

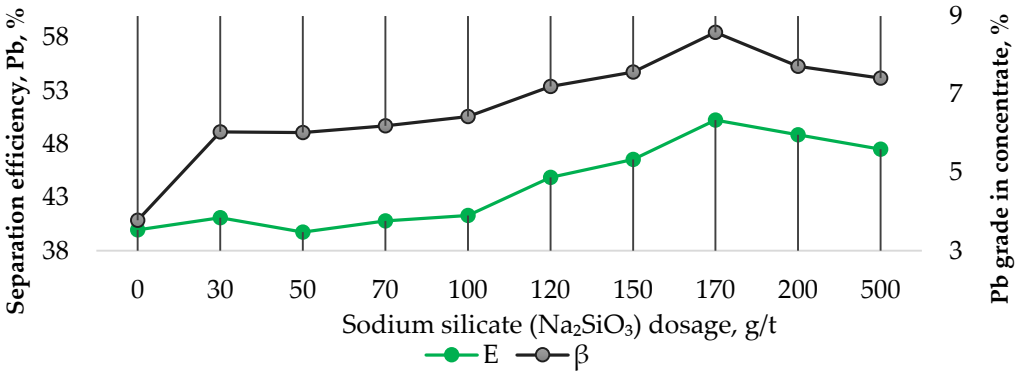

A

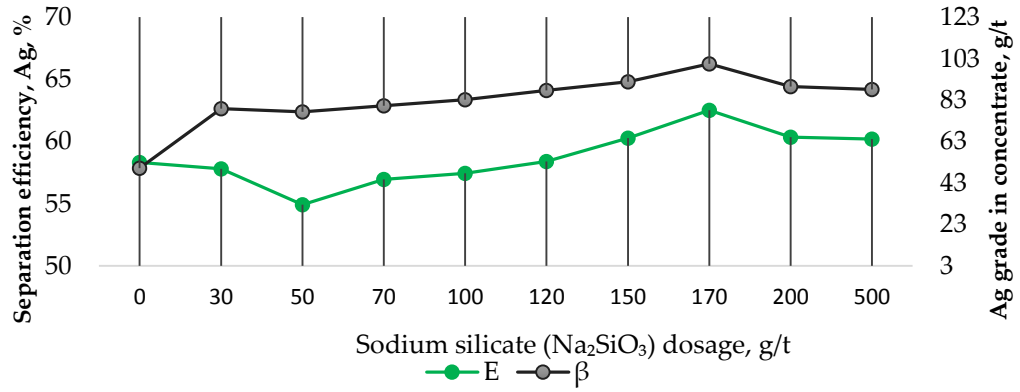

B

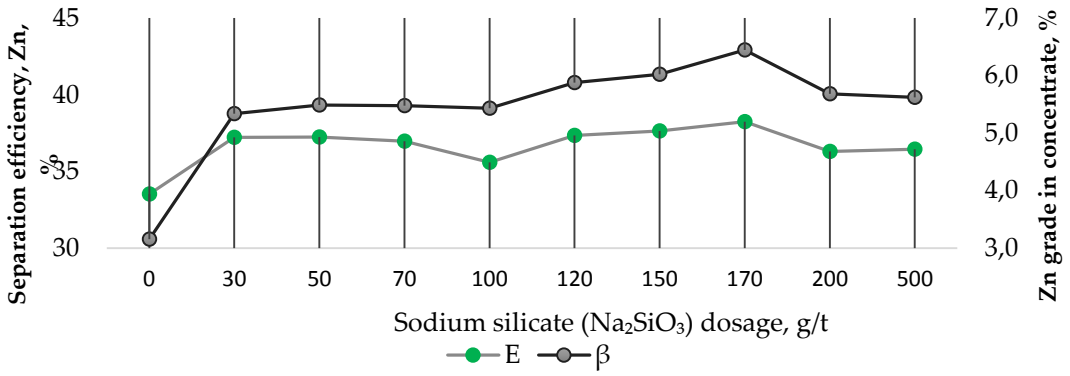

C

Figure 5. Effect of sodium silicate (Na_2SiO_3) dosage on separation efficiency and metal grade in concentrate: (A) Pb, (B) Ag, and (C) Zn.

Note – compiled by the authors

The maximum separation efficiency and metal grade were obtained at a sodium silicate dosage of 170 g/t. This dosage can therefore be considered optimal for improving the quality of the Pb–Zn concentrate under the studied flotation conditions.

The calculation results presented in Figure 5 show that the variation in separation efficiency generally correlates with changes in the metal grade and recovery of the target components. This confirms that the applied efficiency criterion adequately reflects the overall flotation performance at different sodium silicate dosages.

Various intermediate cases may also occur during flotation separation. With an increase in the partial yield of the concentrate in an ideal separation operation, while maintaining the same overall separation efficiency, the contribution of concentrate contamination increases. In this regard, the operational concentrate yield in the ideal separation operation can be used as an additional criterion complementing the Hancock–Luyken criterion.

The additional criterion is expressed by the following equation:

$$D = \frac{\varepsilon - E}{1 - E}$$

where ε is the recovery of the valuable component in the concentrate;

E is the separation efficiency determined by the Hancock-Luyken criterion.

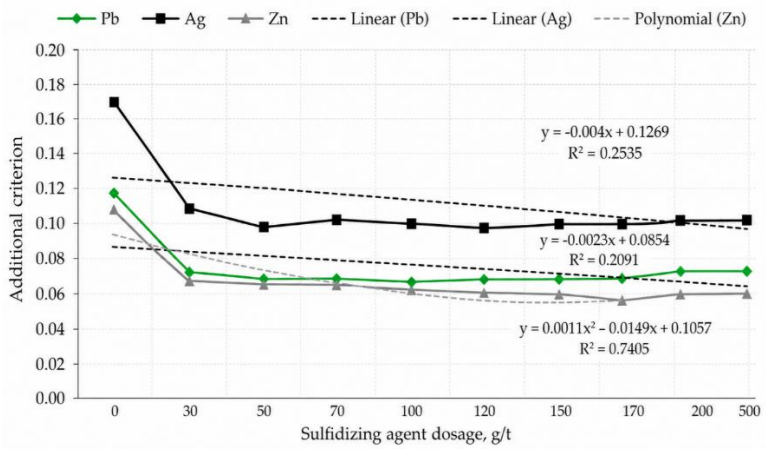

Figure 6. Additional separation efficiency criterion for Pb, Ag and Zn as a function of sodium silicate (Na_2SiO_3) dosage

Note – compiled by the authors

The analysis of the additional separation efficiency criterion shows that sodium silicate dosage has a significant effect on concentrate contamination and flotation selectivity. At low Na_2SiO_3 dosages, the additional criterion values are relatively high, especially for Ag, which indicates a greater contribution of gangue and slime entrainment into the concentrate.

With increasing Na_2SiO_3 dosage, the additional criterion for Pb, Ag and Zn generally decreases, indicating improved depression of silicate and slime minerals and reduced contamination of the froth product. The most favorable values are observed in the dosage range of 150–170 g/t, where high metal grades and recoveries are achieved together with improved separation selectivity.

Further increasing the Na_2SiO_3 dosage to 200–500 g/t does not lead to a significant improvement in the additional criterion. This suggests that excessive sodium silicate addition does not further enhance separation efficiency and may partially depress valuable mineral particles. Therefore, a sodium silicate dosage of 170 g/t can be considered rational for improving the quality of the Pb–Zn concentrate while maintaining acceptable recovery of Pb, Zn and Ag.

DISCUSSION

The obtained results can be explained by the mechanism of sodium silicate (Na_2SiO_3) action as a depressant and dispersant for silicate and slime minerals. According to the literature, sodium silicate undergoes hydrolysis in aqueous pulp with the formation of monomeric and polymeric silicate species, including H_4SiO_4 and $SiO(OH)_3^-$. These species can adsorb on the surface of gangue minerals, increasing their hydrophilicity and reducing the probability of collector attachment (Wang et al., 2024; Ni et al., 2025; Silva et al., 2012).

At low Na_2SiO_3 dosages, the depressant effect of the reagent is insufficient; therefore, part of the silicate, carbonate, and slime particles is mechanically entrained into the froth product. This results in an increased concentrate yield and lower Pb, Zn, and Ag grades. In the base test without sodium silicate, the concentrate yield was 7.20 %, whereas the grades of Pb, Zn, and Ag were relatively low. This indicates significant contamination of the concentrate by gangue minerals.

Increasing the Na_2SiO_3 dosage to 170 g/t promoted more effective depression of gangue and slime minerals. As a result, the mechanical entrainment of non-valuable particles into the froth product decreased, while the grades of valuable components in the concentrate increased. At this dosage, the maximum grades of Pb, Zn, and Ag were obtained: 8.58 %, 6.44 %, and 100.46 g/t, respectively. At the same time, relatively high recoveries of Pb, Zn, and Ag were maintained, confirming the improvement in flotation selectivity.

The depressant mechanism of Na_2SiO_3 is associated with the formation of hydrophilic silicate coatings on the surface of gangue minerals. It has been shown that sodium silicate is an effective depressant for calcium-bearing minerals and can reduce the floatability of calcite, fluorite, dolomite, and other minerals due to the adsorption of silicate species on their surfaces (Wang et al., 2024). In addition, Na_2SiO_3 is widely considered a flotation regulator capable of depressing quartz and silicate minerals; at elevated dosages, it may also exert a depressant effect on sulfide minerals (Ni et al., 2025).

A further increase in Na_2SiO_3 dosage to 200–500 g/t did not improve concentrate quality. On the contrary, a decrease in Pb, Zn, and Ag grades was observed. This may be related to excessive adsorption of silicate species in the pulp and partial depression of sulfidized surfaces of valuable minerals. Such behavior is consistent with literature data indicating that excessive sodium silicate addition can reduce the flotation activity not only of gangue minerals but also of valuable minerals due to the formation of hydrophilic surface layers (Ni et al., 2025; Silva et al., 2012).

Thus, the effect of Na_2SiO_3 is clearly dosage-dependent. At insufficient reagent dosage, gangue depression remains incomplete, whereas excessive sodium silicate addition may

deteriorate the flotation of valuable minerals. A dosage of 170 g/t can be considered rational, since it provides an optimal balance between the depression of silicate–slime components and the preservation of the floatability of sulfidized Pb-, Zn-, and Ag-bearing minerals.

CONCLUSIONS

This study investigated the effect of sodium silicate (Na_2SiO_3) dosage on the flotation performance of oxidized lead–zinc ore from the Koshkuduk deposit after preliminary sulfidization with calcium polysulfide.

It was established that the introduction of Na_2SiO_3 into the reagent regime has a pronounced effect on flotation selectivity and the quality of the obtained concentrate. In the base test without sodium silicate, the concentrate yield was 7.20 %, with Pb, Zn, and Ag grades of 3.78 %, 3.15 %, and 50.03 g/t, respectively. The addition of Na_2SiO_3 reduced the concentrate yield and increased the grades of valuable components, which is associated with the depression of silicate and slime minerals.

The best technological results were obtained at a Na_2SiO_3 dosage of 170 g/t. Under this condition, the concentrate yield was 3.62 %, while the Pb grade reached 8.58 %, the Zn grade reached 6.44 %, and the Ag grade reached 100.46 g/t. The recoveries of Pb, Zn, and Ag were 53.56 %, 41.64 %, and 66.12 %, respectively. Compared with the base test, the Pb grade in the concentrate increased by 2.27 times, the Zn grade by 2.04 times, and the Ag grade by 2.01 times.

Calculations using the Hancock–Luyken criterion and the additional separation efficiency criterion confirmed that a Na_2SiO_3 dosage of 170 g/t provides the most favorable combination of valuable component grades, recoveries, and separation selectivity. A further increase in sodium silicate dosage to 200–500 g/t did not improve flotation performance, which can be explained by the excessive depressant effect of the reagent and the possible reduction in the floatability of sulfidized valuable minerals.

Thus, a sodium silicate dosage of 170 g/t can be considered rational for improving the quality of Pb–Zn concentrate from oxidized ore of the Koshkuduk deposit. The obtained results confirm the feasibility of using Na_2SiO_3 as a depressant for silicate and slime components during the flotation of refractory oxidized lead–zinc ores.

CONFLICT OF INTEREST: The authors declare no conflict of interest..

FUNDING: This research was funded by the Committee of Science of the Ministry of Education and Science of the Republic of Kazakhstan, grant project No. AR23489765.

INSTITUTIONAL REVIEW BOARD STATEMENT: Not applicable. This study was purely technical and did not involve human participants or animals.

INFORMED CONSENT STATEMENT: Not applicable. This study did not involve human participants.

DATA AVAILABILITY STATEMENT: The data supporting the findings of this study are available from the corresponding author upon reasonable request.

ACKNOWLEDGEMENTS: The authors express their gratitude to the laboratory staff for technical support during sample preparation, flotation experiments, and analytical measurements.

STATEMENT ON THE USE OF ARTIFICIAL INTELLIGENCE TECHNOLOGIES: Artificial intelligence tools were used for language editing, text structuring, and improvement of academic style during manuscript preparation. The authors reviewed and approved the final version of the manuscript and take full responsibility for its scientific content, data interpretation, and conclusions.

REFERENCES

Nayak, A., Jena, M. S., & Mandre, N. R. (2022). Beneficiation of lead–zinc ores: A review. Mineral Processing and Extractive Metallurgy Review, 43(5), 564–583. https://doi.org/10.1080/08827508.2021.1903459

Liu, W., Wang, Z., Wang, X., & Miller, J. D. (2020). Smithsonite flotation with lauryl phosphate. Minerals Engineering, 147, 106155. https://doi.org/10.1016/j.mineng.2019.106155

Maghfouri, S., Hosseinzadeh, M. R., Rajabi, A., & Choulet, F. (2018). A review of major non-sulfide zinc deposits in Iran. Geoscience Frontiers, 9(1), 249–272. https://doi.org/10.1016/j.gsf.2017.04.003

Yi, Y., Li, P., Zhang, G., Feng, Q., & Han, G. (2022). Stepwise activation of hemimorphite surfaces with lead ions and its contribution to sulfidization flotation. Separation and Purification Technology, 299, 121679. https://doi.org/10.1016/j.seppur.2022.121679

Elizondo-Álvarez, M. A., Uribe-Salas, A., & Nava-Alonso, F. (2020). Flotation studies of galena, cerussite and anglesite with hydroxamic acids as collectors. Minerals Engineering, 155, 106456. https://doi.org/10.1016/j.mineng.2020.106456

Xue, J., Qu, Y., Chen, Y., Zhang, Ch., Bu, X. (2023). Effective sulfide flotation of cerussite by using trithiocyanuric acid as a novel sulfurizing reagent. Minerals Engineering, 201, 108087. https://doi.org/10.1016/j.mineng.2023.108087

Zhang, S., Xian, Y., Wen, Sh., Liang, G. (2022). Enhancement of xanthate adsorption on lead-modified and sulfurized smithsonite surface in the presence of ammonia. Minerals Engineering, 189, 107872. https://doi.org/10.1016/j.mineng.2022.107872

Zuo, Q., Yang, J., Shi, Y. F., Wu, D. (2020). Activating hemimorphite using a sulfidation-flotation process with sodium sulfosalicylate as the complexing agent. Journal of Materials Research and Technology, 9(5), 10110–10120. https://doi.org/10.1016/j.jmrt.2020.07.005

Bai, S., Li, C., Fu, X., Ding, Z., & Wen, Sh. (2020). Ammonium chloride catalyze sulfidation mechanism of smithsonite surface: Visual MINTEQ models, ToF-SIMS and DFT studies. Minerals Engineering, 147, 106115. https://doi.org/10.1016/j.mineng.2019.106115

Zheng, Y. X., Lv, Jf., Wang, H., Wen, Sh. & Pang, J. (2018). Formation of zinc sulfide species during roasting of ZnO with pyrite and its contribution on flotation. Scientific Reports, 8, 7832. https://doi.org/10.1038/s41598-018-26229-3

Ge, B. L., Pang, J., Zheng, Yx., Ning, Jl., Lü, Jf. (2020). Sulfidation mechanism of cerussite in the presence of sulphur at high temperatures. Journal of Central South University, 27, 3664–3673. https://doi.org/10.1007/s11771-020-4544-2

Ke, Y., Peng, N., Xue, K., Min, X., Chai, L., Pan, Q., Liang, Y., Xiao, R., Wang, Y., Tang, Ch., Liu, H. (2018). Sulfidation behavior and mechanism of zinc silicate roasted with pyrite. Applied Surface Science, 435, 1011–1018. https://doi.org/10.1016/j.apsusc.2017.11.202

Li, Z., Chen, M., Huang P., Zhang, Q., Song Sh. (2017). Effect of grinding with sulfur on surface properties and floatability of three nonferrous metal oxides. Transactions of Nonferrous Metals Society of China, 27(12), 2745–2755. https://doi.org/10.1016/S1003-6326(17)60274-7

Li, C. X., Wei, Ch., Deng, Z. G., Li, X. B., Li M. T., Xu, H. Sh. (2014). Hydrothermal sulfidation and flotation of oxidized zinc–lead ore. Metallurgical and Materials Transactions B, 45, 833–838. https://doi.org/10.1007/s11663-013-9887-8

Luo, Y., Ou, L., Chen, J., Zhang, G. (2023). Understanding the impact of ammonium salt on the sulfidization of smithsonite from coordination chemistry. Applied Surface Science, 625, 157723. https://doi.org/10.1016/j.apsusc.2023.157723

Zhang, X., Deng, J., Wang, Y., Wang, G., Xu, H. (2022). Novel insight into the lead sulfide species formed on hemimorphite surface during lead ions improved sulfidation. Colloids and Surfaces A: Physicochemical and Engineering Aspects, 650, 129959. https://doi.org/10.1016/j.colsurfa.2022.129959

Zhao, W., Yang, B., Liu D., Feng, Q. (2022). Effect of copper ions on sulfidization flotation of smithsonite. Colloids and Surfaces A: Physicochemical and Engineering Aspects, 650, 129515. https://doi.org/10.1016/j.colsurfa.2022.129515

Mambetaliyeva, A., Makasheva, G. K., Sabirova, L.B., Tussupbekova, T.Sh., Rysbekov, K.B., & Barmenshinova, M.B. (2026). Flotation kinetics of oxidized lead–zinc ore in the Eh–pH system using calcium polysulfide. Applied Sciences, 16(12), 5791. https://doi.org/10.3390/app16125791

Wang, J., Lu, W., Cao, Z., Wu, X., Wang, P., Wang, X., & Liu, W. (2024). New insights into the depressive mechanism of sodium silicate on bastnaesite, parisite, and fluorite: Experimental and DFT study. Minerals, 14(9), 870. https://doi.org/10.3390/min14090870

Ni, L., Lv, J., Kong, L., Qin, L. (2025). Effects of sodium silicate on flotation separation of fluorite, calcite, and scheelite. Minerals, 15(1), 82. https://doi.org/10.3390/min15010082

Silva, J. P. P., Baltar, C. A. M., Gonzaga, R. S. G., Peres, A. E. C., & Leite, J. Y. P. (2012). Identification of sodium silicate species used as flotation depressants. Minerals & Metallurgical Processing, 29(4), 207–210. https://doi.org/10.1007/BF03402458

Marinakis, K. I., & Shergold, H. L. (1985). Influence of sodium silicate addition on the adsorption of oleic acid by fluorite, calcite and barite. International Journal of Mineral Processing, 14(3), 177–193.

Chepushtanova, T.A., Motovilov, I.Yu., Merkibayev, Y.S., Polyakov, K.V., & Gostu, S. (2022). Flotation studies of the middling product of lead-zinc ores with preliminary sulfidizing roasting of oxidized lead and zinc compounds. Complex Use of Mineral Resources, 323(4), 77–84. https://doi.org/10.31643/2022/6445.43

Information about authors

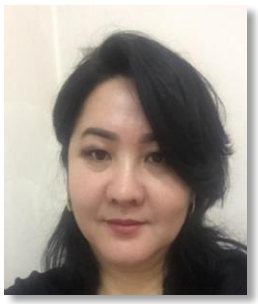

Alima Mambetaliyeva – Ph.D., Associate Professor, Mining and Metallurgical Institute named after O.A. Baikonurov, Department of Metallurgy and Mineral Processing, Almaty, Kazakhstan.
E-mail: a.mambetaliyeva@satbayev.university
ORCID: https://orcid.org/0000-0003-1536-5259

Guldana Makasheva – Doctoral student of the Department of Metallurgy and Mineral Processing at Satbayev University, Almaty, Kazakhstan.
E-mail: mguldanka@mail.ru
ORCID: https://orcid.org/0000-0003-2875-9433

Tansholpan Tussupbekova – Doctoral student of the Department of Metallurgy and Mineral Processing at Satbayev University, Almaty, Kazakhstan
E-mail: tansholpan_87.09@mail.ru
ORCID: https://orcid.org/0000-0003-2940-8715

Alemgul Tanabayeva – Doctoral student of the Department of Metallurgy and Mineral Processing at Satbayev University, Almaty, Kazakhstan
E-mail: alemgul.tanabaeva@gmail.com
ORCID: https://orcid.org/0000-0003-4992-5138

https://doi.org/10.51885/3134-7983_CATMSP_2026_2_6
SRSTI 53.39.31

SYNTHESIS OF COBALT-FREE HIGH-STRENGTH WC-BASED CEMENTED CARBIDES BY SPARK PLASMA SINTERING

Nurken Mussakhan [1], **Aray Abdimutalip** [1]*, **Sardor Kambarbekov** [1], **Dilnoza Baltabayeva** [1], **Berik Kaldar** [1]

[1]The Research Institute "Natural Sciences, Nanotechnology and New Materials",
Khoja Akhmet Yassawi International Kazakh-Turkish University, Turkestan, Kazakhstan
* Corresponding author: Aray Abdimutalip, e-mail: aray.abdimutalip@ayu.edu.kz

Keywords:
Tungsten carbide, Fe-Ni binder, Spark plasma sintering, microstructure, X-ray diffraction, EDS mapping.

ABSTRACT

This study investigates the effect of spark plasma sintering (SPS) temperature (1250 °C and 1300 °C) on the microstructure, phase composition, porosity, density of cobalt-free WC–Fe–Ni, WC–Fe, and WC–Ni hard alloys. The aim of the work was to evaluate the potential of Fe- and Fe–Ni-based binders as alternatives to cobalt in cemented carbides for cutting-tool applications. Microstructural analysis revealed that the WC–Fe–Ni alloy formed a homogeneous and dense structure with a uniform distribution of WC particles at 1250 °C, while increasing the sintering temperature to 1300 °C resulted in carbide grain refinement. In contrast, the WC–Fe system exhibited grain coarsening at the higher temperature. The WC–Ni alloy was characterized by large irregular grains and the formation of brittle secondary phases. X-ray diffraction analysis confirmed the presence of WC, Fe_3W_3C, $FeNi_3$, and Fe–Ni solid-solution phases in the WC–Fe–Ni system, whereas the WC–Ni alloy was dominated by W_2C and W_3Ni_3C phases. Increasing the SPS temperature reduced porosity from 13.2% to 12.7% in WC–Fe–Ni and from 13.8% to 12.0% in WC–Fe, accompanied by an increase in relative density to approximately 87–88%. In contrast, the WC–Ni alloy exhibited the highest porosity (~16%). The results demonstrate that both binder composition and SPS temperature strongly influence phase evolution, densification, and microstructural development. Fe-containing binders provided greater structural homogeneity and phase stability, highlighting their potential as cobalt-free alternatives for cemented carbide applications.

INTRODUCTION

Enhancing the performance properties of materials and products, along with extending their operational lifetime, represents one of the most critical challenges in modern materials science. In this context, intensive research is underway into alloys and protective coatings that can offer high wear resistance, strength, and thermal stability under severe operating conditions. Among such materials, cemented carbides based on tungsten carbide hold a special position, being widely utilized across various industries to protect tools and structural components of machinery (Aghaali et al., 2023; Huang et al., 2025; Zhong et al., 2016). Consequently, these alloys find applications in numerous fields, including metallurgy, medicine, transport, aerospace, as

well as in the production of excavator teeth and other parts of earthmoving equipment (Buravlev et al., 2021; Ma et al., 2019; Maizza et al., 2018). In cemented carbides, tungsten carbide serves as the primary hard phase, imparting high hardness and wear resistance to the alloy. At the same time, the material exhibits considerable crack resistance, reaching about 15–20 MPa·m$^{1/2}$ (Cai et al., 2019; Heydari et al., 2012; Ren et al., 2025). Thanks to the combination of these attributes, such materials can be employed to protect components operating under extreme conditions, including parts of nuclear power plants, where high temperatures and significant thermal loads may occur. Traditionally, cobalt is used as the metallic binder in cemented carbides, playing a key role in wetting tungsten carbide particles and forming a robust metallic matrix. This enhances the material's flexural strength, achieving 3–4 GPa. This, in turn, contributes to the improved strength and stability of refractory hard alloys based on WC. Moreover, iron can form stable carbide phases that are thermodynamically stable and promote the refinement of tungsten carbide grains, which positively affects the material's mechanical properties. Ni-Fe alloys are widely adopted in industry owing to their good corrosion resistance and relatively low cost (Gao et al., 2018; Jin et al., 2022; Soria-Biurrun et al., 2023). With an optimal choice of chemical composition and processing parameters, such materials can exhibit properties comparable to, or even exceeding, those of conventional cobalt-based binder systems.

A variety of technological techniques are employed to produce these alloys, including laser remelting, vacuum melting, conventional sintering, and other powder metallurgy approaches. However, the optimal balance of strength and hardness is typically achieved through modern sintering methods, with spark plasma sintering (SPS) being particularly noteworthy. SPS relies on the application of pulsed electric current, which activates compaction and reactive sintering processes in powder materials. Compared to conventional methods such as hot pressing, hot isostatic pressing, induction heating, or liquid-phase sintering, this technology enables high material density to be attained at lower temperatures and within substantially shorter processing times (Chang et al., 2015).

Although considerable attention has been devoted to the development of cobalt-free WC-based cemented carbides, a systematic comparison of Fe-, Ni-, and Fe–Ni-bonded systems processed under identical SPS conditions remains limited. In particular, the influence of binder composition on phase evolution, microstructure development, and hardness at different SPS temperatures has not been fully clarified. Furthermore, the potential of Fe–Ni binders as a cost-effective and environmentally friendly alternative to conventional cobalt binders requires further investigation. Therefore, the novelty of the present work lies in the comparative study of WC–Fe, WC–Ni, and WC–Fe–Ni cemented carbides fabricated by SPS at different sintering temperatures. Special attention is given to the relationship between binder composition, phase formation, microstructural evolution, and hardness, as well as to the assessment of Fe–Ni binders as potential substitutes for cobalt in cutting-tool applications.

The objective of this work is to fabricate cobalt-free WC-(FeNi), WC–Fe, and WC–Ni cemented carbide systems using SPS and to investigate their phase composition, morphology, hardness, and physical–mechanical properties.

MATERIALS AND METHODS

In this study, tungsten carbide (WC), nickel (Ni), and iron (Fe) with a purity of 99% and a particle size of less than 50 μm, supplied by Hebei Suoyi New Material Technology (Hebei Province, China), were used as starting powder materials. The preparation of powder mixtures included a mechanical activation step. The mechanical activation process and detailed experimental procedure were previously described in our previous work (Aidarova et al., 2025). The mechanosynthesis conditions used in the experiments are given in Table 1.

Table 1. Modes for Mechanosynthesis WC-FeNi, WC-Fe, WC-Ni and composition of powder mixture (Aidarova et al., 2025)

Sample name	Unique code	Time, hour	Surfactant additive (stearic acid), wt%	Rotation speed, rpm	Atmosphere	Mass ratio, (ball/powder)
Powder mixture blending	a	0,3	-	200	Argon	10:1
Mechanosynthesis						
88 wt% WC - 12 wt.%Fe	b1	1	2.5	500	Argon	10:1
	c1	2				
	d1	4	3			
88 wt% WC - 12 wt% Ni	b2	1	2.5			
	c2	2				
	d2	4	3			
88 wt% WC - 6 wt% Fe + 6 wt% Ni	b3	1	2.5			
	c3	2				
	d3	4	3			
Note – compiled by the authors						

After mechanical activation, the resulting powder mixtures were subjected to SPS consolidation using a Dr. Sinter SPS-625 system. The powder mixture was loaded into a 20 mm diameter graphite mold and pre-compacted under a load of 200 kg at a heating rate of 100 °C/min. Sintering was carried out at temperatures of 1250°C and 1300°C with a 5-minute hold, followed by cooling to room temperature over 50 minutes. Three samples with different mass fractions of the components were analyzed; their compositions are presented in Table 2.

Table 2. Sintering conditions for samples using the SPS method

Samples	Composition (wt%)	Temperature ℃	Holding time (min)
Alloy 1	88 wt.% WC+6 wt.% Fe+6 wt.% Ni	1250	5
Alloy 2	88 wt.% WC+6 wt.% Fe+6 wt.% Ni	1300	
Alloy 3	88 wt.% WC+12 wt.% Fe	1250	
Alloy 4	88 wt.% WC+12 wt.% Fe	1300	
Alloy 5	88 wt.% WC+12 wt.% Ni	1300	
Note – compiled by the authors			

A Tescan Vega 4 scanning electron microscope (SEM) with a thermionic tungsten cathode was used to accurately examine the sample and obtain detailed surface images. Surface details, phase types, and structural characteristics of the powders were analyzed using an X-ray diffractometer (Malvern Panalytical Ltd., Almelo, the Netherlands) with a Cu anode, a 20-90° measurement angle, a 40 kV light-emitting tube voltage, a 30 mA current, a 0.02 step size, and a 2 s measurement time at each step.

RESULTS AND DISCUSSION

XRD patterns of WC-based alloys after various sintering temperature processes. X-ray phase analysis of fine- and coarse-grained composites with different contents of the Fe-Ni binder phase (Fig. 1) showed that samples of WC-Fe-Ni and WC-Fe compositions predominantly consist

of Fe, WC and Fe3W3C phases, which is consistent with the data of Lee et al. (2021). At a sintering temperature of 1250°C, WC is the main and most stable carbide phase. However, as the temperature increases to 1300°C, a decrease in the intensity of WC peaks is observed in the WC-Fe-Ni system, which is due to the partial dissolution of tungsten carbide. The released carbon can react with alloy components to form secondary phases such as Fe_3W_3C, W_2C, and free carbon C. Despite possible phase transformations, WC retains key performance advantages: high hardness, high melting point, thermal shock resistance, and oxidation resistance. The formation of a small amount of the brittle η-phase Fe_3W_3C is due to the reaction α-Fe + WC → γ-Fe + Fe_3W_3C. The low intensity of its diffraction peaks is explained by its small volume fraction.

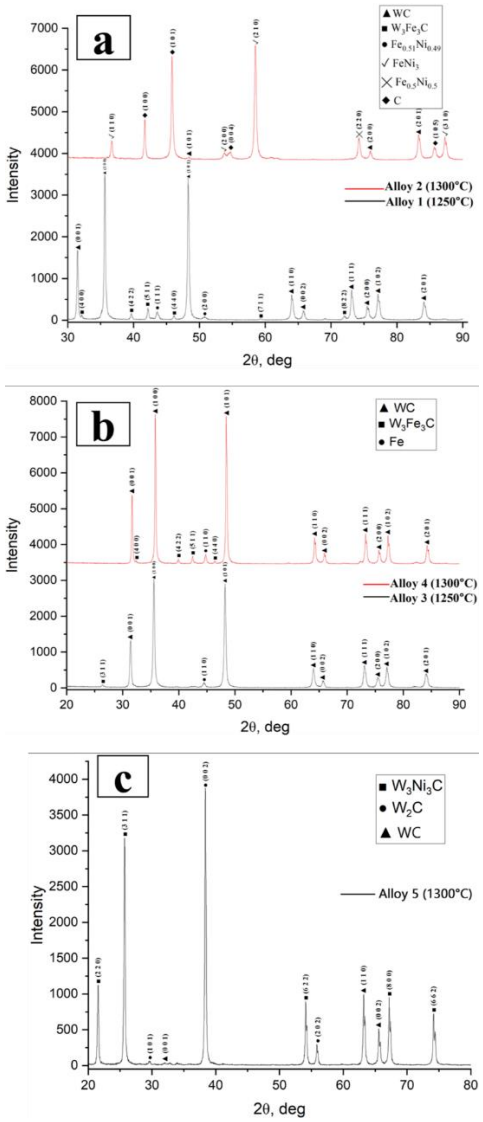

Figure 1. XRD patterns of WC-Fe-Ni cemented carbides with different compositions: (a) Alloy 1,2 (1250 and 1300°C); (b) Alloy 3,4 (1250 and 1300°C); (c) Alloy 5 (1300°C).
Note – compiled by the authors

However, the presence of this phase can weaken the grain boundaries between WC particles and the iron matrix, which potentially reduces the wear resistance of the material (Pan et al., 2019). In the WC-Fe system, an increase in the Fe3W3C content is also associated with SPS features, as noted in Rosa et al. (2020). Under solid-phase sintering conditions at elevated

temperatures and short holding times, carbon diffusion is limited, but sufficient for the formation of secondary phases. In WC-Ni samples (Fig. 1c), the subcarbide phase W2C was detected, which promotes grain coarsening, leading to a decrease in hardness and fracture toughness (Cai et al., 2018). The formation of W2C can occur as a result of carbon redistribution during cooling, while the characteristic faceted morphology of WC grains is preserved (Zeng et al., 2025). The introduction of nickel into the WC-Fe-Ni system leads to a decrease in the grain size and deformation of the crystal lattice due to the formation of solid solutions of the Fe0.5Ni0.5 and Fe0.51Ni0.49 types, which is accompanied by the occurrence of internal microscopic stresses. In addition, the formation of the intermetallic phase FeNi3 helps to suppress the formation of the brittle η-phase. The use of a binder phase based on Fe-Ni also improves the corrosion resistance and oxidation stability of the composite (Kurbanbekov et al., 2024). Additionally, it should be noted that under SPS conditions, possible formation of metastable phases such as Ni3C (3Ni + C → Ni3C) and W2C (2WC + 3Ni → W2C + Ni3C) should be noted, which can lead to the formation of η-phases of the Ni3W3C type (da Silva et al., 2021). The formation of Ni3W3C carbide, characterized by a reduced carbon content, is undesirable, since it leads to a significant deterioration in the mechanical properties of the material (Aghaali et al., 2023). It should be noted separately that there is a pronounced diffraction peak of free carbon (C), which may indicate a local redistribution of carbon during the sintering process and its incomplete binding into carbide phases. Morphology and EDS mapping of tungsten carbide samples. The average grain size is 3±1.5 μm. The morphology of the samples is shown in Fig. 2 and was obtained after sintering using the SPS method. As can be seen from Fig. 2a (1250°C), the structure is relatively loose, the tungsten carbide grains are unevenly distributed, and agglomeration areas are observed. The presence of dark "pore" areas indicates an insufficient degree of compaction and incomplete densification at this temperature.

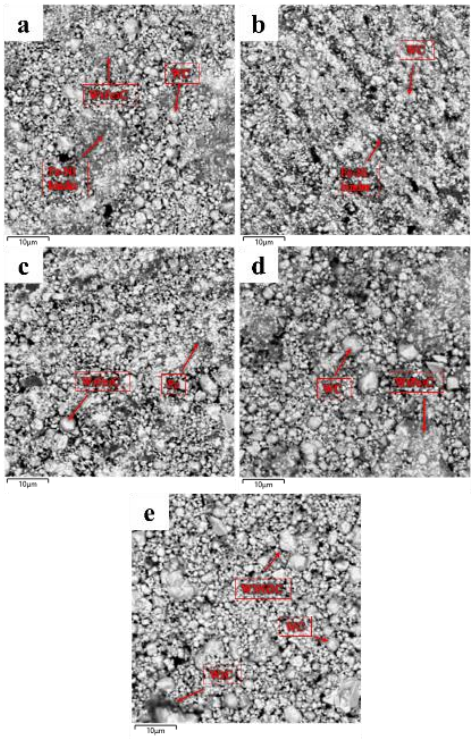

Figure 2. SEM microstructures of the WC-Fe-Ni cemented carbides sintered at different temperatures: (a) Alloy 1 (1250°C); (b) Alloy 2 (1300°C); (c) Alloy 3 (1250°C); (d) Alloy 4 (1300°C); and (e) Alloy 5 (1300°C).

Note – compiled by the authors

In Fig. 2c (1250°C), the structure becomes more uniform compared to Fig. 2a, however, areas with insufficient wetting of the carbide particles by the metal binder remain, indicating limited diffusion and incomplete formation of interphase contacts. With an increase in temperature to 1300°C (Fig. 2b), a pronounced compaction of the structure, a decrease in porosity and an improvement in intergranular cohesion are observed. A more efficient interaction and wetting of tungsten carbide with the iron-nickel binder is noted, which contributes to the formation of a dense composite structure. Fig. 2d (1300°C) shows the growth of WC grains due to the thermal activation of diffusion processes at elevated temperatures, which is consistent with the literature data (Cramer et al., 2020). At the same time, the porosity is significantly reduced compared to the sample obtained at 1250°C (Fig. 2c), indicating a higher degree of sintering. In Fig. 2e (1300°C), the sample with the nickel binder demonstrates the densest and most uniform microstructure. The porosity is minimal, which is associated with the high wetting capacity of nickel and the intensification of diffusion processes at elevated temperatures, which is also confirmed by the results of Aidarova et al. (2025). The intergranular space is effectively filled with the binder, ensuring good adhesion between WC grains and the formation of a uniform composite structure. EDS mapping of the samples obtained at temperatures of 1250 and 1300°C is shown in Fig. 3. WC particles are predominantly rounded and surrounded by a metallic binder based on iron and nickel. This indicates the formation of a binder phase uniformly distributed in the intergranular space and ensuring the formation of a relatively homogeneous composite structure, which is consistent with the results of [23]. The Ni and Fe elements are localized predominantly along the WC grain boundaries, forming a continuous or partially continuous intergranular binder, which promotes structure compaction and improves interparticle contact. At a temperature of 1300°C, a more uniform distribution of the binder elements is observed, which is associated with the intensification of diffusion processes and an increase in the degree of densification. It should be noted that EDS analysis makes it difficult to detect light elements such as carbon (C) and oxygen (O) due to their low sensitivity and overlapping spectral lines. It should be noted that the quantification of light elements, particularly carbon and oxygen, by EDS is associated with higher uncertainty compared with heavier elements such as W, Fe, and Ni. Therefore, the reported C and O contents should be considered semi-quantitative and used primarily for comparative analysis. The measured density of the WC–Fe–Ni alloys increased from 12.39 g/cm3 at 1250 °C to 12.46 g/cm3 at 1300 °C, indicating progressive consolidation during SPS. This behavior can be attributed to enhanced particle rearrangement, neck growth, and diffusion-driven mass transport occurring at elevated temperatures. A comparable trend was observed for the WC–Fe alloys, where the density rose from 12.15 g/cm3 to 12.40 g/cm3 with increasing sintering temperature. The improvement in densification is likely associated with intensified diffusion processes and more effective elimination of residual pores. The WC–Ni alloy exhibited a density of 12.09 g/cm3, which is consistent with its comparatively higher porosity and less compact microstructure. Therefore, their presence is detected primarily in specific zones, particularly in pores or defective areas of the structure. The WC–Fe–Ni composites exhibited a porosity of 13.2% after sintering at 1250 °C. Raising the sintering temperature to 1300 °C resulted in a slight reduction in porosity to 12.7%, indicating enhanced densification of the material. A similar tendency was observed for the WC–Fe system, where porosity decreased from 13.8% at 1250 °C to 12.0% at 1300 °C. These results suggest that higher SPS temperatures promote more efficient particle bonding and consolidation, thereby reducing the volume fraction of pores. In contrast, the WC–Ni alloy sintered at 1300 °C exhibited a porosity of approximately 16%, reflecting a lower degree of densification compared with the Fe-containing systems. The presence of carbon may also be due to the use of graphite fixtures during SPS, which leads to its possible diffusion into the surface layers of the samples. Average atomic and mass percentage values for selected plots are given in table 3a and 3b.

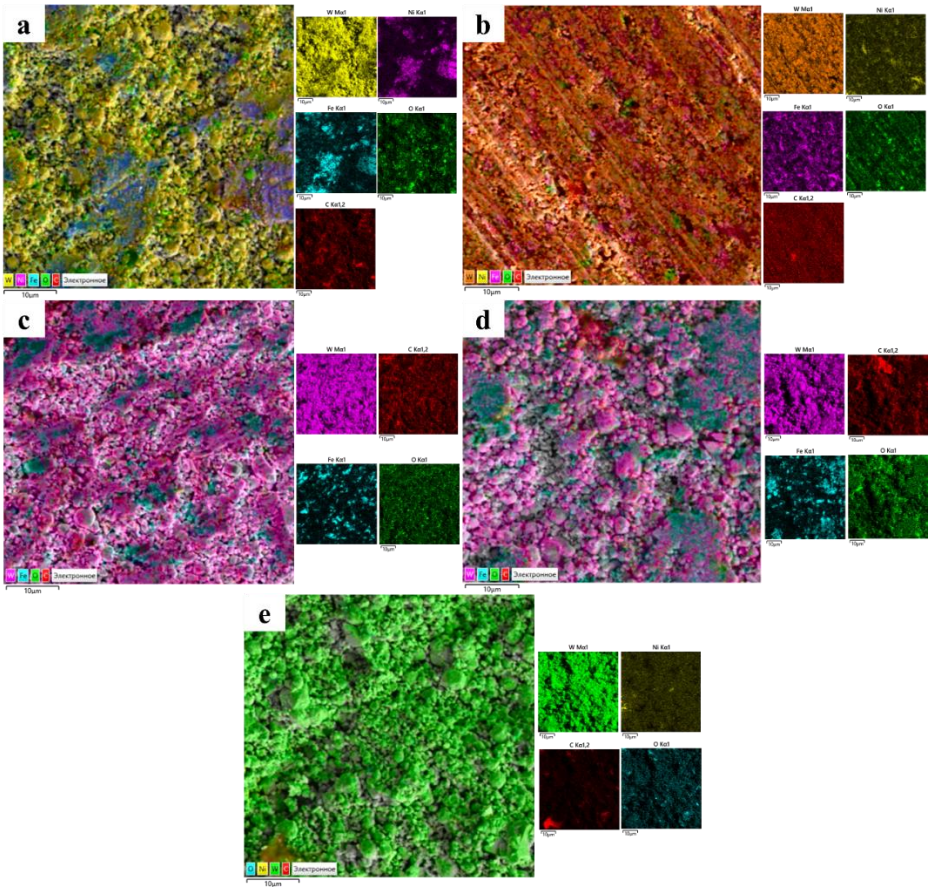

Figure 3. EDS elemental mapping of the alloys after sintering at different temperatures: (a) Alloy 1 (1250°C); (b) Alloy 2 (1300°C); (c) Alloy 3 (1250°C); (d) Alloy 4 (1300°C); and (e) Alloy 5 (1300°C)

Note – compiled by the authors

Table 3a. Average elemental composition (wt.%) derived from EDS maps.

Alloy	WC (wt.%)	Fe (wt.%)	Ni (wt.%)	C (wt.%)	O (wt.%)
Alloy 1	73.75	6.02	5.02	11.84	3.38
Alloy 2	61.82	13.80	3.66	15.74	4.98
Alloy 3	84.66	11.41	0	0	3.93
Alloy 4	70.02	12.69	0	12.71	4.58
Alloy 5	84.24	0.28	0.54	12.90	2.04
Note – compiled by the authors					

Table 3b. Average elemental composition (at.%) derived from EDS maps.

Alloy	WC (at.%)	Fe (at.%)	Ni (at.%)	C (at.%)	O (at.%)
Alloy 1	22.39	6.01	4.77	55.04	11.79
Alloy 2	14.83	10.90	2.75	57.80	13.72
Alloy 3	50.58	22.45	0	0	26.97
Alloy 4	19.51	11.64	0	54.18	14.67
Alloy 5	27.37	0.30	0.55	64.16	7.63
Note – compiled by the authors					

CONCLUSIONS

This study investigated the influence of SPS sintering temperature on the microstructure, phase composition, and morphology of cobalt-free WC-based hardmetals with Fe–Ni, Fe, and Ni binder systems.

Microstructural analysis showed that the WC–Fe–Ni alloy sintered at 1250 °C exhibited a relatively homogeneous and dense structure with a uniform distribution of WC particles within the metallic binder. Increasing the sintering temperature to 1300 °C resulted in microstructural refinement of the carbide phase accompanied by the appearance of localized pores, indicating changes in densification behavior and binder phase redistribution. In the WC–Fe system, higher sintering temperature promoted WC grain growth and the development of a coarser microstructure. EDS analysis revealed the presence of oxygen-containing regions, suggesting partial oxidation of the binder phase at elevated temperature. Increasing the SPS temperature promoted densification in the Fe-containing systems. The porosity of the WC–Fe–Ni alloy decreased from 13.2% to 12.7%, whereas the WC–Fe alloy showed a more significant reduction from 13.8% to 12.0%, accompanied by an increase in relative density to approximately 87–88%. These results indicate improved particle bonding and structural consolidation at higher sintering temperatures. In contrast, the WC–Ni alloy exhibited the highest porosity (~16%), suggesting less effective densification and contributing to its inferior microstructural integrity and mechanical performance.

X-ray diffraction analysis confirmed the formation of WC, Fe_3W_3C, and Fe–Ni phases in the WC–Fe–Ni alloy. Increasing the sintering temperature led to changes in the relative intensities of diffraction peaks and the appearance of additional carbon-containing phases. In the WC–Fe system, WC and Fe_3W_3C remained the dominant phases over the investigated temperature range. In contrast, the WC–Ni alloy was characterized by the formation of W_2C and W_3Ni_3C phases, indicating a different phase evolution pathway compared with the Fe-containing systems.

The results demonstrate that both binder composition and SPS temperature strongly influence the phase evolution, microstructure development, and densification behavior of WC-based hardmetals. Among the investigated compositions, Fe-containing binder systems exhibited higher structural homogeneity and phase stability, whereas the Ni-bonded alloy showed a greater tendency toward the formation of secondary carbide phases. These findings provide useful guidance for the design and optimization of cobalt-free WC hardmetals produced by spark plasma sintering.

CONFLICT OF INTEREST: The authors declare no conflict of interest.

FUNDING: The author(s) declare that financial support was received for the research and/or publication of this article. This research is funded by the Committee of Science of the Ministry of Science and Higher Education of the Republic of Kazakhstan (grant No. BR24992925).

INSTITUTIONAL REVIEW BOARD STATEMENT: Not applicable. The study did not involve human or animal subjects.

INFORMED CONSENT STATEMENT: Not applicable. This research did not involve human participants.

DATA AVAILABILITY STATEMENT: The data supporting the findings of this technical study are available from the corresponding author upon reasonable request.

ACKNOWLEDGEMENTS: We express our gratitude to the Science Committee of the Ministry of Science and Higher Education of the Republic of Kazakhstan. For support of the project “Development of technologies and materials for innovative development of the manufacturing industry of the Republic of Kazakhstan”.

STATEMENT ON THE USE OF ARTIFICIAL INTELLIGENCE TECHNOLOGIES: The authors declare that no artificial intelligence technologies were used in the preparation of this manuscript.

REFERENCES

Huang, N., Guo, S., Ren, H., Guo, J., Li, B., Zhang, J., & Hu, M. (2025). Preparation of V-element-containing Co-based composite powders by spray conversion and its effect on the microstructure properties of cemented carbides. Journal of Alloys and Compounds, 1010, 178273. https://doi.org/10.1016/j.jallcom.2024.178273

Zhong, L., Zhang, X., Chen, S., Xu, Y., Wu, H., & Wang, J. (2016). Fe–W–C thermodynamics and in situ preparation of tungsten carbide-reinforced iron-based surface composites by solid-phase diffusion. International Journal of Refractory Metals and Hard Materials, 57, 42–49. https://doi.org/10.1016/j.ijrmhm.2016.02.001

Aghaali, V., Ebadzadeh, T., Zahraee, S. M., & Mirkazemi, S. M. (2023). Microstructure and mechanical properties of WC–TiC–Co cemented carbides produced by spark plasma sintering (SPS) method. SN Applied Sciences, 5, 285. https://doi.org/10.1007/s42452-023-05510-9

Buravlev, I. Y., Shichalin, O. O., Papynov, E. K., Golub, A. V., Gridasova, E. A., Buravleva, A. A., & Sergienko, V. I. (2021). WC–5TiC–10Co hard metal alloy fabrication via mechanochemical and SPS techniques. International Journal of Refractory Metals and Hard Materials, 94, 105385. https://doi.org/10.1016/j.ijrmhm.2020.105385

Maizza, G., Montanari, R., Richetta, M., Varone, A., Kaciulis, S., Mezzi, A., & Soltani, P. (2018). Surface phenomena during the early stage of liquid phase SPS of a mixture of coarse WC and Ni-alloy particles. Surface and Interface Analysis, 50, 1072–1076. https://doi.org/10.1002/sia.6418

Ma, B., Wang, X., Chen, C., Zhou, D., Xu, P., & Zhao, X. (2019). Dissimilar welding and joining of cemented carbides. Metals, 9, 1161. https://doi.org/10.3390/met9111161

Ren, H. Y., Guo, S. D., Huang, N., Chen, H., Li, B., Guo, J. F., & Wang, B. Q. (2025). Processing of WC-based hard metals using Co–Cr powders obtained by spray conversion. Ceramics International, 51, 15960–15972. https://doi.org/10.1016/j.ceramint.2025.01.432

Cai, X., Zhong, L., Xu, Y., Li, X., & Liu, M. (2019). Microstructure and fracture toughness of a WC–Fe cemented carbide layer produced by a diffusion-controlled reaction. Surface and Coatings Technology, 357, 784–793. https://doi.org/10.1016/j.surfcoat.2018.10.096

Heydari, D., Skandani, A. A., & Al Haik, M. (2012). Effect of carbon content on carbide morphology and mechanical properties of AR white cast iron with 10–12% tungsten. Materials Science and Engineering: A, 542, 113–126. https://doi.org/10.1016/j.msea.2012.02.040

Jin, H., Ji, R., Dong, T., Liu, S., Zhang, F., Zhao, L., & Liu, Y. (2022). Efficient fabrication and characterization of Ni–Fe–WC composite coatings with high corrosion resistance. Journal of Materials Research and Technology, 16, 152–167. https://doi.org/10.1016/j.jmrt.2021.11.145

Soria-Biurrun, T., Lozada-Cabezas, L., Navarrete-Cuadrado, J., Ibarreta-Lopez, F., Martinez-Pampliega, R., & Sanchez-Moreno, J. M. (2023). Densification of WC–Fe–Ni–Co–Cr cemented carbides processed by HIP after sintering: effect of WC powder particle size. International Journal of Refractory Metals and Hard Materials, 110, 105994. https://doi.org/10.1016/j.ijrmhm.2022.105994

Gao, Y., Luo, B. H., He, K. J., Zhang, W. W., & Bai, Z. H. (2018). Effect of Fe/Ni ratio on the microstructure and properties of WC–Fe–Ni–Co cemented carbides. Ceramics International, 44, 2030–2041. https://doi.org/10.1016/j.ceramint.2017.10.148

Chang, S. H., Chang, M. H., & Huang, K. T. (2015). Study on the sintered characteristics and properties of nanostructured WC–15 wt%(Fe–Ni–Co) and WC–15 wt% Co hard metal alloys. Journal of Alloys and Compounds, 649, 89–95. https://doi.org/10.1016/j.jallcom.2015.07.119

Aidarova, M., Kurbanbekov, S., Kizatov, A., Urkunbay, A., Bayatanova, L., Rutkowska-Gorczyca, M., & Amangeldiyeva, Y. (2025). Influence of milling time and binder composition on phase evolution in WC-based composite powders fabricated via high-energy ball milling. Frontiers in Materials, 12, 1684414. https://doi.org/10.3389/fmats.2025.1684414

Lee, J. H., Hong, S. K., & Park, H. K. (2021). Effects of deep cryogenic treatment for tungsten carbide iron cemented carbide. International Journal of Refractory Metals and Hard Materials, 100, 105649. https://doi.org/10.1016/j.ijrmhm.2021.105649

Pan, Y., Liu, A., Huang, L., Du, Y., Jin, Y., Yang, X., & Zhang, J. (2019). Effects of metal binder content and carbide grain size on the microstructure and properties of SPS manufactured WC–Fe composites. Journal of Alloys and Compounds, 784, 519–526. https://doi.org/10.1016/j.jallcom.2019.01.057

Rosa, J. M. B., Lugon, R. D., de Souza Silva, K., das Chagas, V. M., da Silva Guimarães, R., de Carvalho, C. S., & Filgueira, M. (2020). Study of characteristics and properties of spark plasma sintered WC with the use of alternative Fe–Ni–Nb binder as Co replacement. International Journal of Refractory Metals and Hard Materials, 92, 105316. https://doi.org/10.1016/j.ijrmhm.2020.105316

Cai, X., Xu, Y., Liu, M., & Zhong, L. (2018). Evaluation of microstructure and growth kinetics of tungsten carbide ceramics at the interface of iron and tungsten. Journal of Alloys and Compounds, 741, 666–676. https://doi.org/10.1016/j.jallcom.2018.01.212

Zeng, X., Wang, R., Tian, X., & Liu, Y. (2025). Corrosion resistance mechanism in WC/FeCrNi composites: Decoupling the role of spherical versus angular WC morphologies. Metals, 15, 777. https://doi.org/10.3390/met15070777

Kurbanbekov, S., Kozhakhmetov, Y., Skakov, M., Seitov, B., Aidarova, M., & Tabiyeva, Y. (2024). Properties, advantages, and prospects of using cobalt-free composites based on tungsten carbide in industry. Materials, 18, 129. https://doi.org/10.3390/ma18010129

da Silva, E. N., dos Santos, A. A. A., do Nascimento, R. M., Alves, S. M., da Silva Guimarães, R., & Filgueira, M. (2021). Investigation of characteristics and properties of spark plasma sintered ultrafine WC–6.4Fe–3.6Ni alloy as potential alternative WC–Co hard metals. International Journal of Refractory Metals and Hard Materials, 101, 105669. https://doi.org/10.1016/j.ijrmhm.2021.105669

Cramer, C. L., Preston, A. D., Ma, K., & Nandwana, P. (2020). In-situ metal binder-phase formation to make WC–FeNi cermets with spark plasma sintering from WC, Fe, Ni, and carbon powders. International Journal of Refractory Metals and Hard Materials, 88, 105204. https://doi.org/10.1016/j.ijrmhm.2020.105204

Information about authors

Nurken Mussakhan – The Research Institute "Natural Sciences, Nanotechnology and New Materials", Khoja Akhmet Yassawi International Kazakh-Turkish University, Turkestan, Kazakhstan, PhD in Technical Physics, Cobalt-free hard alloys; Microstructure characterization; Physical and mechanical properties of materials
E-mail: nurken.mussakhan@ayu.edu.kz
ORCID: https://orcid.org/0000-0003-4154-0356

Aray Abdimutalip – The Research Institute «Natural Sciences, Nanotechnology and New Materials», Khoja Akhmet Yassawi International Kazakh-Turkish University, Turkestan, Kazakhstan, Second-year master's student, Department of Physics, Spark plasma sintering (SPS); Tungsten carbide-based cemented carbides; Cobalt-free hard alloys
E-mail: aray.abdimutalip@ayu.edu.kz
ORCID: https://orcid.org/0009-0004-0172-2520

Sardor Kambarbekov – The Research Institute «Natural Sciences, Nanotechnology and New Materials», Khoja Akhmet Yassawi International Kazakh-Turkish University, Turkestan, Kazakhstan, Second-year doctoral student, Department of Physics, Spark plasma sintering (SPS); Tungsten carbide-based cemented carbides; Cobalt-free hard alloys
E-mail: sardor.kambarbekov@ayu.edu.kz
ORCID: https://orcid.org/0009-0001-6794-1281

Dilnoza Baltabayeva – The Research Institute «Natural Sciences, Nanotechnology and New Materials», Khoja Akhmet Yassawi International Kazakh-Turkish University, Turkestan, Kazakhstan, Second-year doctoral student, Department of Physics, Spark plasma sintering (SPS); Tungsten carbide-based cemented carbides; Cobalt-free hard alloys
E-mail: dilnoza.baltabayeva@ayu.edu.kz
ORCID**:** https://orcid.org/0000-0001-8249-4398

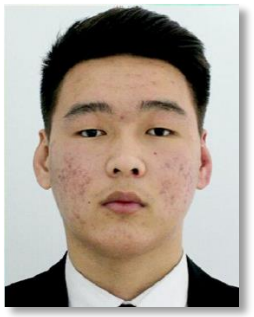

Berik Kaldar – The Research Institute «Natural Sciences, Nanotechnology and New Materials», Khoja Akhmet Yassawi International Kazakh-Turkish University, Turkestan, Kazakhstan, Second-year master's student, Department of Physics, Spark plasma sintering (SPS); Tungsten carbide-based cemented carbides; Cobalt-free hard alloys
E-mail: berik.kaldar@ayu.edu.kz
ORCID: https://orcid.org/0009-0002-9267-7029

https://doi.org/10.51885/3134-7983_CATMSP_2026_2_7
SRSTI 29.19.19

CRYSTALLIZATION BEHAVIOR AND ELECTRICAL PROPERTIES OF InSe AND In_2Se_3 THIN FILMS PREPARED BY THERMAL EVAPORATION

Zabira Oman [1], Nurken Nurlybekov [1], Yerzhan Umarov [1], Ulan Zhylysbayev [1], Alibek Zhakypov [1], Renata Nemkayeva [2], Yerzhan Mukhametkarimov [1,2*]

[1]Faculty of Physics and Technology, Al-Farabi Kazakh National University, Almaty, Kazakhstan
[2]Nanotechnology Laboratory, Al-Farabi Kazakh National University, Almaty, Kazakhstan
*Corresponding author: Yerzhan Mukhametkarimov, e-mail: yerzhan.mukhametkarimov@kaznu.edu.kz

Keywords:
Indium selenide thin films, thermal evaporation, temperature dependence of electrical resistance, phase transition, X-ray structural analysis, Raman spectroscopy

ABSTRACT

In recent years, semiconductors based on indium selenide have attracted significant attention in advanced research due to their unique electronic properties. Characteristics such as low effective electron mass, high thermal conductivity, and high photosensitivity are particularly pronounced in two-dimensional (2D) InSe nanocrystals. However, challenges associated with their large-scale fabrication limit their application in industrial technologies. In this work, the crystallization of amorphous In_xSe_y thin films deposited by thermal evaporation is investigated through annealing in an inert gas atmosphere to obtain large-area InSe and In_2Se_3 thin films. It is shown that annealing films with an In/Se stoichiometry of 50/50 at 350 °C leads to the formation of the β-InSe phase, whereas films with a stoichiometry of 40/60 form a two-phase system consisting of β-In_2Se_3 and γ-In_2Se_3 under the same conditions. The kinetics of electrical resistance during film crystallization is analyzed. Measurements of the temperature dependence of electrical resistance reveal a sharp decrease in the resistance of the InSe film near 170-180 °C, while the In_2Se_3 film exhibits a two-step decrease at approximately 150-190 °C and 270 °C. The results demonstrate the potential of these thin-film phase change materials for application in memory devices.

INTRODUCTION

The indium-selenium phase diagram contains many thermodynamically stable crystalline phases with different stoichiometries, among which InSe and In_2Se_3, are of particular interest due to their unique electronic properties (Bergeron et al., 2020; Günkel et al., 2025; J. Li et al., 2021; Wojnar et al., 2025). High-temperature In_2Se_3 crystal is known for its ferroelectric properties (W. Zheng et al., 2025; X. Zheng et al., 2022), whereas InSe is considered a promising material for optoelectronic applications due to its high charge carrier mobility (Zhao et al., 2020). The band gap of single-layer InSe crystal is approximately ~1.3 eV (Mudd et al., 2013), while for In_2Se_3 crystal this value can vary from 1.3 to 1.9 eV depending on the polymorphic phase. (Chanchal et al., 2022). In general, In_2Se_3 can exist in stable layered α-, β-, and δ- phases, as well as in a non-layered, wurtzite-like γ-phase (W. Li et al., 2018; W. Zheng et al., 2025). In contrast, crystalline InSe has only a layered structure and can exist in α, β, ε, and δ polytypes depending on the stacking sequence of the layers. Within each layer, In and Se atoms are covalently bonded, while adjacent layers are held together by weak van der Waals interactions.

Atomically thin layers of two-dimensional (2D) In_xSe_y nanocrystals can be obtained by mechanical exfoliation. Due to quantum confinement effects, the electronic properties of these 2D crystals differ significantly from those of their bulk counterparts. For instance, it has been demonstrated that the band gap of monolayer InSe crystal increases to ~2.6 eV (Bandurin et al., 2017). Consequently, it paves the way to obtain InSe crystals with the desired electronic structure by controlling the number of layers.

In_xSe_y crystals have attracted attention in the field of optoelectronics, and in recent years their application as functional elements of electrical and optical memory devices has been extensively investigated. The heating-induced transformation of the low-temperature α-In_2Se_3 crystal into the β-In_2Se_3 or γ-In_2Se_3 phases leads to a dramatic change in the material's electrical properties. Based on this phenomenon, prototypes of electrical memory devices have been developed (Choi et al., 2017; W. Zheng et al., 2025).

In the context of development of electrical and optical memory cells, thin In_xSe_y films produced by physical vapor deposition (PVD) are of particular interest (Bergeron et al., 2020; Chanchal et al., 2022; J. Hossain, M. Julkarnain, 2013; Jeengar et al., 2023). This method enables the production of amorphous (a-In_xSe_y) thin film over a large area, which structural and electrical properties can be tuned through post-deposition thermal treatment. Depending on the annealing condition the various crystalline phases can form, leading to significant changes in the electrical properties of the film. Therefore, a comparative analysis of the films with different stoichiometry In_xSe_y under identical annealing and measurement conditions can provide a better understanding of the differences in their functionality, including the evolution of electrical resistance associated with the structural transformation under heat treatment.

In this study, amorphous a-InSe and a-In_2Se_3 thin films were obtained by thermal evaporation of pre-synthesized bulk InSe and In_2Se_3 polycrystals in a vacuum. A comparative study of their crystallization behavior during annealing in an inert atmosphere was also carried out together with an analysis of the temperature dependence of electrical resistance during the heating.

MATERIALS AND METHODS

InSe and In_2Se_3 crystals were synthesized by melting metallic In and elemental Se in a vacuum at a temperature of 860 °C. First, In and Se with a purity of 99.9% were placed in a quartz ampoule at the required mass ratio and hermetically sealed under high vacuum (10^{-3} Pa). The ampoule was then placed in the active zone of the heating furnace described in our previous paper (Oman et al., 2025) and slowly heated. To ensure proper mixing of the molten elements, a vibration motor was connected to the quartz tube in which the ampoule was placed. The formation of high-quality crystals was ensured by a controlled decrease in the temperature of the ampoule with the melt down to 500 °C at a rate of 1–2 °C per minute, followed by further natural cooling to room temperature.

In the next stage, thin InSe and In_2Se_3 films were obtained by thermal evaporation under high vacuum (~10^{-4} Pa) using a resistive heating technique. As a heating stage we used tungsten plates coated with an alumina (Kurt J. Lesker). Such heater minimizes direct contact between the InSe polycrystals and heating material, i.e. metallic tungsten. As a substrate, a high-transparency KU-1 quartz glass (2×2 cm) and a monocrystalline silicon wafer (Si (100), 5-10 Ω×cm, 1×1 cm, Zhejiang Lijing Optoelectronics Technology Co., Ltd.) were used. Before the deposition, the substrates were cleaned in isopropanol using ultrasonic treatment. The deposition was carried out without heating a substrate holder. The distance between evaporation source and the substrate holder was fixed at 10 cm.

The structure of the obtained materials was studied by Raman spectroscopy (Solver Spectrum, NT-MDT) using 633 nm excitation laser source and X-ray structural analysis with the

CuKα monochromator (Rigaku MiniFlex 600), while their elemental composition was analyzed using energy dispersive spectroscopy (EDS) based on SEM with EDAX device (Quanta 3D 200i, FEI company). To determine the film thickness, a scratch was made on the surface of films, then the step edge between film and substrate was scanned using atomic force microscopy (AFM).

The annealing of the as-deposited amorphous thin films was carried out in an ultra-high purity argon (Ar, Ihsantechnogaz, 99.999%) gas atmosphere at 350 °C for a 20 min with the heating rate of 2°C /min. The temperature dependence of the electrical resistance of thin films was studied in situ during the annealing. The measurements were performed in a sealed chamber equipped with two stainless steel needle type electrodes, a heating stage and a gas flow system. The electrodes were brought into direct contact with the film surface, while the distance between the electrodes was fixed at 2 mm. The measurements were carried out using a Keithley 6485 picoammeter connected to computer for automated recording of the electrical current as function of the temperature.

RESULTS AND DISCUSSION

To obtain thin-film samples of InSe and In_2Se_3, bulk polycrystalline InSe and In_2Se_3 were first synthesized, and then the resulting crystals were thermally evaporated onto the selected substrates in high vacuum.

Characterization of bulk InSe and In_2Se_3 crystals

InSe and In_2Se_3 crystals were initially synthesized by melting In and Se elements in a sealed ampoule at a temperature of 860 °C. The Raman spectrum of the obtained InSe crystal is characterized by three peaks at 114, 175 and 224 cm^{-1}. These peaks correspond to the A_1, E" and A'_1 phonon vibrational modes characteristic of the β-polytype of the InSe crystal (Fig. 1a).

The Raman spectrum of the stoichiometric In_2Se_3 sample is characterized by several distinct peaks at 87, 104 (A_1 (LO+TO)) and ~187 (A_1 (LO)) cm^{-1} (Fig. 1b). It is evident that the broad peak at ~187 cm^{-1} consists of several components. In general, this set of peaks corresponds to the vibrational modes of the α-In_2Se_3 phase. A low-intense peak at ~250 cm^{-1} in the spectrum indicates the presence of a small amount of free selenium, while the peak at 150 cm^{-1} is associated with the γ-phase of the In_2Se_3 crystal.

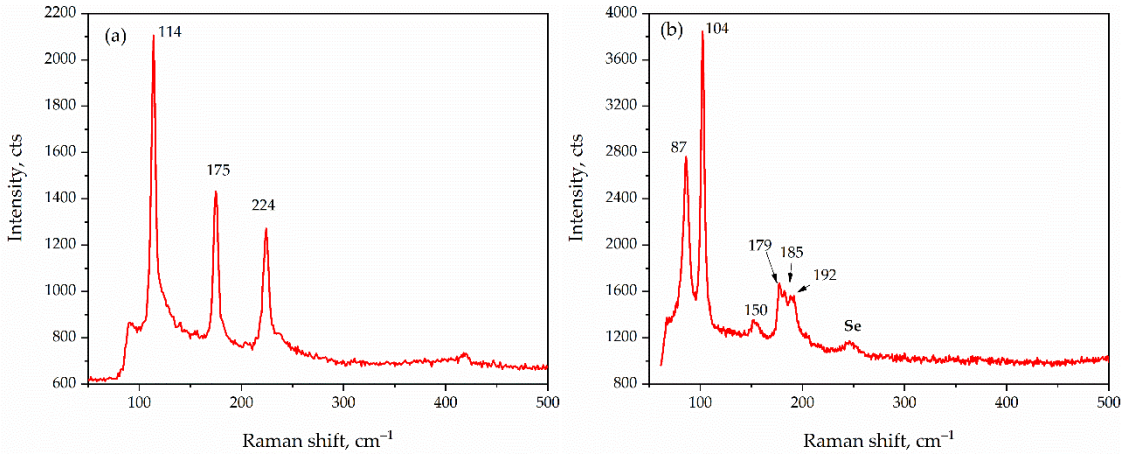

Figure 1. Raman spectra of InSe (a) and In_2Se_3 (b) crystals

The results of EDS analysis along with SEM images of the obtained crystals are presented in Table 1 and Figures 2(a) and 2(b). It can be seen from the SEM images that both InSe and In_2Se_3 crystals possess a layered structure.

Table 1. Elemental composition (EDS analysis) of InSe and In_2Se_3 samples

Element	InSe crystal	InSe thin film	In_2Se_3 crystal	In_2Se_3 thin film
In, at. %	48.81	49.68	40.54	40.49
Se, at. %	51.19	50.32	59.46	59.51

The structure of the synthesized crystals was characterized by X-ray diffraction (XRD) analysis using a Rigaku X-ray analytical system with a CuKα monochromator. The XRD pattern of the InSe crystal (Figure 3(a)) confirms a hexagonal crystal structure belonging to the $P6_3/mmc$ space group with lattice parameters: a = b = 4.0 Å, c = 16.6 Å. The X-ray diffraction pattern of the In_2Se_3 crystal also indicated a formation of hexagonal structure (space group $P6_3/mmc$) with lattice parameters a = b = 4.0 Å, c = 19.2 Å. Additional reflections corresponding to the (100) and (101) planes of elemental selenium were also observed. Phase identification was performed using the PDXL software package (Rigaku) by comparison of experimental diffraction patterns with reference ICDD PDF database card. The card number is shown at the inset of the figure.

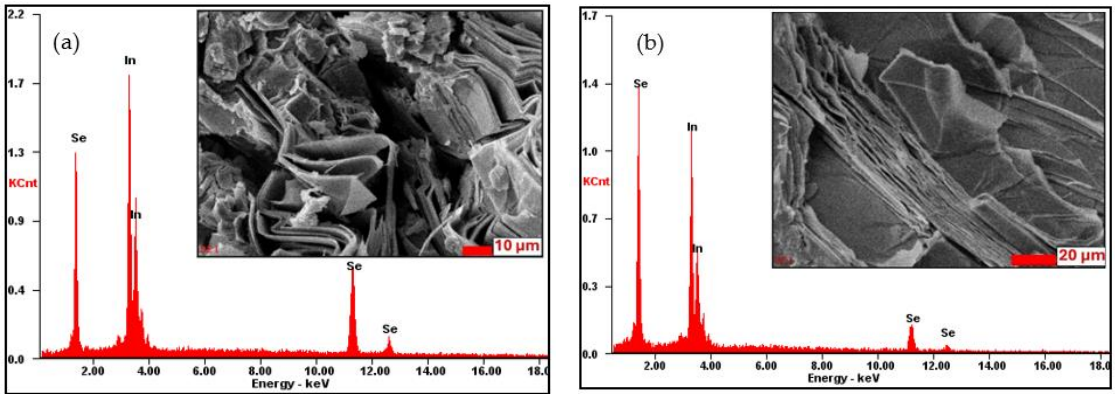

Figure 2. EDS spectra and SEM images of InSe (a) and In_2Se_3 (b) crystals

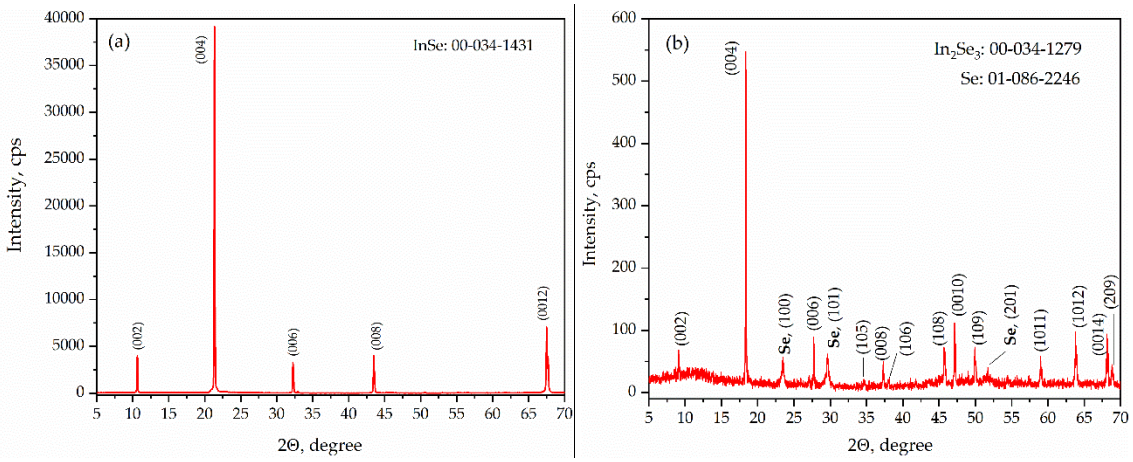

Figure 3. XRD patterns of InSe (a) and In_2Se_3 (b) crystals

Characterization of InSe and In_2Se_3 thin films

Pre-synthesized bulk InSe and In_2Se_3 crystals were thermally evaporated on highly transparent quartz substrates in high vacuum (~10^{-4} Pa) to obtain thin films. The evaporation was

carried out using a tungsten plate coated with an aluminum oxide layer. The thicknesses of the deposited films were 215 nm for InSe and 450 nm for In_2Se_3. The halo-type of XRD patterns and the absence of distinct peaks in the Raman spectra indicate an amorphous structure of the obtained films (Fig. 4-5).

Thermal treatment of as-deposited amorphous thin films in inert atmosphere leads to their crystallization. The peaks at 114 cm^{-1}, 175 cm^{-1} and 225 cm^{-1} appearing in the Raman spectrum of the InSe film (c-InSe), annealed at 350 °C for 20 min in Ar, are characteristic of the β-InSe polytype (Fig. 4a). This result was also confirmed by the XRD analysis data - the diffraction pattern shown in Fig. 5(b) corresponds to a hexagonal structure with lattice parameters a=3.99 Å and c=16.62 Å (Space group: 194:P63/mmc, No. 00-034-1431). The EDS analysis showed that the stoichiometry of the films was preserved similar to that of the initial crystals (Table 1). Thus, proposed technique for production of crystalline InSe films over a large area is considered feasible and effective. It is important to note that annealing the compounds based on In-Se at temperatures other than 350 °C leads to the formation of various phases, In_4Se_3 or In_3Se_4, in the film. Experiments have shown that amorphous a-InSe film annealed at the temperature interval of 300-350°C transforms into biphasic InSe/In_4Se_3 system.

As-deposited amorphous In_2Se_3 thin film was annealed at the same conditions. The appearance of a single peak at 148 cm^{-1} in the Raman spectrum of the annealed crystalline (c-In_2Se_3) thin film shown in Fig. 4(b) indicates the formation of a γ-phase In_2Se_3 crystal. However, XRD pattern shown in Fig. 5d reveals reflections from the planes of the γ-In_2Se_3 and β-In_2Se_3 phases. These findings can be explained by the fact that the temperature of 350 °C is not sufficient for the formation of a uniform single-phase γ-In_2Se_3 crystalline film. It is known that In_2Se_3 crystals typically transform from the α-phase to the β-phase at 200 °C, while further transformation from the β-phase to the γ-state may start at a temperature of 350°C (Han et al., 2014).

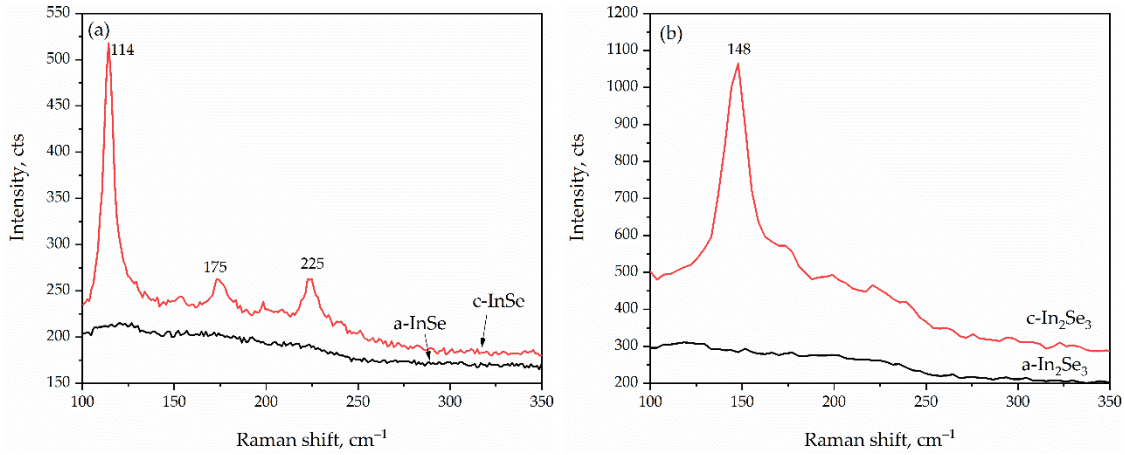

Figure 4. Raman spectra of as-deposited (amorphous) and annealed (crystalline) InSe (a) and In_2Se_3 (b) thin films

Structural transformations are typically accompanied by a change in the physical properties and thermodynamic state of the material. In our case, the crystallization of the films induces a sharp change in their electrical resistance. Therefore, one of the key tasks of this work is to study the temperature dependence of the electrical resistance of thin InSe and In_2Se_3 films. Plots of the obtained dependencies are presented in Figure 6. As can be seen from the figure, the resistance of InSe film demonstrates a sharp decrease by 5 orders of magnitude at around 170-180 °C from ~10^9 Ω to ~10^4 Ω. This can be explained by the formation of conductive channels in the film because of the structural transformation, i.e. amorphous-to-crystalline phase transition.

Several measurements of resistance under heating showed the transition in the temperature indicated interval. These observations correlate with the many reports of other authors. Numerous studies have shown that this transition in InSe films typically occurs in the range of 120-200 °C, depending on the film thickness (Fedyanina et al., 2025; J. Hossain, M. Julkarnain, 2013). The presented experimental curve is typical for films with thickness of 100-300 nm. Raman spectroscopy and XRD analysis of annealed InSe thin film revealed the formation of crystalline β-InSe, suggesting that the resistance drops correlate with the crystallization of the film.

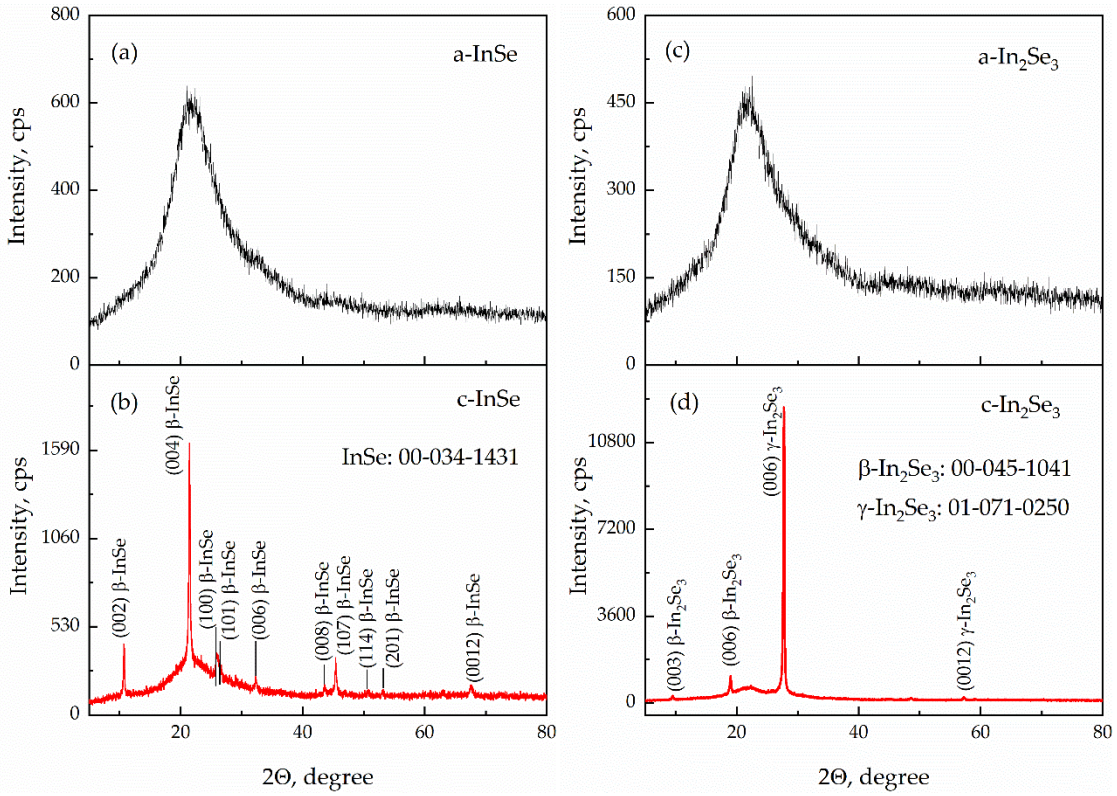

Figure 5. XRD patterns of as-deposited (amorphous) (a,c) and annealed (crystalline) (b,d) InSe and In_2Se_3 thin films

The same analysis for In_2Se_3 thin film revealed a two-step transition from a high-resistance state to a low-resistance state. Initially, the resistance decreases from ~10^{12} Ω to ~10^{7} Ω near 150-190 °C, followed by a second transition near 270 °C, in which the resistance further decreased to ~10^{5} Ω. The observed behavior may indicate a more complex crystallization process involving several structural transformations. The first transition step is possibly associated with the crystallization of the material (formation of low temperature phases α and β In_2Se_3), and the second step can be explained by the transition of already crystalline film from the β -In_2Se_3 phase to the γ -In_2Se_3 phase. Overall, a two-step drop in the electrical resistance of thin In_2Se_3 films was previously demonstrated by Xu et al. in 2023 and multi-level electrical memory cells were designed based on this system. According to the ex-situ Raman and XRD results, the annealed film contains γ-In_2Se_3 and β-In_2Se_3 phases, which suggests that the electrical resistance evolution is related to phase transformation.

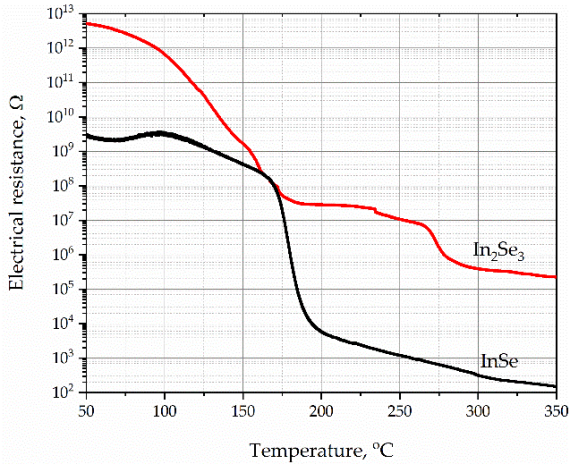

Figure 6. Temperature dependence of the electrical resistance of InSe (black) and In_2Se_3 (red) thin films

CONCLUSIONS

This study presents a comparative analysis of the crystallization conditions of InSe and In_2Se_3 thin films deposited by thermal evaporation. Annealing of the as-deposited thin films in an inert gas atmosphere at 350 °C for 20 min results in the transformation of amorphous InSe into crystalline β-InSe, while amorphous In_2Se_3 crystallizes into two-phase system consisting of β- and γ- In_2Se_3. These results demonstrate that precise control of annealing conditions is essential for obtaining crystalline indium selenide thin films with the desired phase states.

Since the key feature of these materials is a pronounced change in physical properties during crystallization, an analysis of the temperature dependence of the electrical resistance of the films was carried out. The R(T) measurements reveal that the resistance of InSe film decreases sharply by several orders of magnitude at ~170°C, whereas In_2Se_3 film exhibits a two-step decrease in the range from 170°C and 270°C. These findings further highlight the potential of In-Se thin films not only for optoelectronics but also for the development of electrical memory cells.

CONFLICT OF INTEREST The authors declare no conflict of interest.

FUNDING: This research has is funded by the Science Committee of the Ministry of Science and Higher Education of the Republic of Kazakhstan (Grant No. AP26103225)

INSTITUTIONAL REVIEW BOARD STATEMENT: Not applicable.

INFORMED CONSENT STATEMENT: Not applicable.

DATA AVAILABILITY STATEMENT: The data supporting the findings of this study are available from the corresponding author upon reasonable request.

ACKNOWLEDGEMENTS: The authors would like to express their gratitude to D. Serikbayev East Kazakhstan Technical University for providing academic and organizational support during the preparation of this research.

STATEMENT ON THE USE OF ARTIFICIAL INTELLIGENCE TECHNOLOGIES: The authors declare that artificial intelligence technologies were used only for language editing, grammar correction, and improvement of the clarity of the text. The authors have reviewed and edited the content and take full responsibility for the final version of the manuscript.

REFERENCES

Bandurin, D. A., Tyurnina, A. V., Yu, G. L., Mishchenko, A., Zólyomi, V., Morozov, S. V., Kumar, R. K., Gorbachev, R. V., Kudrynskyi, Z. R., Pezzini, S., Kovalyuk, Z. D., Zeitler, U., Novoselov, K. S., Patanè, A., Eaves, L., Grigorieva, I. V., Fal'ko, V. I., Geim, A. K., & Cao, Y. (2017). High

electron mobility, quantum Hall effect and anomalous optical response in atomically thin InSe. Nature Nanotechnology, 12(3), 223–227. https://doi.org/10.1038/nnano.2016.242

Bergeron, H., Guiney, L. M., Beck, M. E., Zhang, C., Sangwan, V. K., Torres-Castanedo, C. G., Gish, J. T., Rao, R., Austin, D. R., Guo, S., Lam, D., Su, K., Brown, P. T., Glavin, N. R., Maruyama, B., Bedzyk, M. J., Dravid, V. P., & Hersam, M. C. (2020). Large-area optoelectronic-grade InSe thin films via controlled phase evolution. Applied Physics Reviews, 7(4), 041402. https://doi.org/10.1063/5.0023080

Chanchal, Jindal, K., Pandey, A., Tomar, M., & Jha, P. K. (2022). Phase-defined growth of In2Se3 thin films using PLD technique for high performance self-powered UV photodetector. Applied Surface Science, 595, 153505. https://doi.org/10.1016/j.apsusc.2022.153505

Choi, M. S., Cheong, B. K., Ra, C. H., Lee, S., Bae, J. H., Lee, S., Lee, G. D., Yang, C. W., Hone, J., & Yoo, W. J. (2017). Electrically driven reversible phase changes in layered In2Se3 crystalline film. Advanced Materials, 29(42), 1703568. https://doi.org/10.1002/adma.201703568

Fedyanina, M. E., Pestova, V. B., Pepelyaev, D. V., Lebedeva, Y. S., Babich, A. V., Smayev, M. P., Romashkin, A. V., Nesterov, S. I., & Kozyukhin, S. A. (2025). Thermal and laser crystallization of InSe thin films formed by vacuum thermal evaporation. Physics of Complex Systems, 6(2), 93–103. https://doi.org/10.33910/2687-153x-2025-6-2-93-103

Günkel, R., Maßmeyer, O., Stein, M., Anhäuser, S., Bräumer, K., Rodriguez, R. S., Anders, D., Dogahe, B. O., Bergmann, M., Solanki, M., Langlotz, N. F., Glowatzki, J., Belz, J., Beyer, A., Witte, G., Chatterjee, S., & Volz, K. (2026). Low temperature MOCVD synthesis of high-mobility 2D InSe. Small, 22(11), 2510911. https://doi.org/10.1002/smll.202510911

Han, G., Chen, Z. G., Drennan, J., & Zou, J. (2014). Indium selenides: Structural characteristics, synthesis and their thermoelectric performances. Small, 10(14), 2747–2765. https://doi.org/10.1002/smll.201400104

Hossain, J., Julkarnain, M., Sharif, K. S., & Khan, K. A. (2013). Crystallization of e-beam evaporated amorphous InSe thin films after heat-treatment. International Journal of Renewable Energy Technology Research, 2(9), 220–226.

Jeengar, C., Tomar, M., Jindal, K., Sharma, A., & Jha, P. K. (2023). Influence of post deposition annealing on thermoelectric properties of In2Se3 thin films. Materials Science in Semiconductor Processing, 153, 107127. https://doi.org/10.1016/j.mssp.2022.107127

Li, J., Li, H., Niu, X., & Wang, Z. (2021). Low-dimensional In2Se3 compounds: From material preparations to device applications. ACS Nano, 15(12), 18683–18707. https://doi.org/10.1021/acsnano.1c03836

Li, W., Sabino, F. P., Crasto de Lima, F., Wang, T., Miwa, R. H., & Janotti, A. (2018). Large disparity between optical and fundamental band gaps in layered In2Se3. Physical Review B, 98(16), 165134. https://doi.org/10.1103/PhysRevB.98.165134

Mudd, G. W., Svatek, S. A., Ren, T., Patanè, A., Makarovsky, O., Eaves, L., Beton, P. H., Kovalyuk, Z. D., Lashkarev, G. V., Kudrynskyi, Z. R., & Dmitriev, A. I. (2013). Tuning the bandgap of exfoliated InSe nanosheets by quantum confinement. Advanced Materials, 25(40), 5714–5718. https://doi.org/10.1002/adma.201302616

Oman, Z., Aitzhanov, M., Nemkayeva, R., Guseinov, N., Markhabayeva, A., Smirnov, V., & Mukhametkarimov, Y. (2025). Effect of the thickness of 2D GaSe crystals on their photoelectric performance. Journal of Electronic Materials, 54(7), 5588–5597. https://doi.org/10.1007/s11664-025-11997-2

Wojnar, P., Wójcik, M., Baranowski, P., Kossut, J., Aleszkiewicz, M., Domagala, J. Z., Dziewiątkowska, R., Głuch, J., Ciepielewski, P., Kuna, M., Kostera, Z., Kret, S., & Chusnutdinow, S. (2025). Quantum size effect in optically active indium selenide crystal phase heterostructures grown by molecular beam epitaxy. Advanced Optical Materials, 13(26), 2500738. https://doi.org/10.1002/adom.202500738

Xu, Z., Yuan, Y., Song, S., Song, Z., Liu, R., & Zhai, J. (2023). Successive crystallization in indium selenide thin films for multi-level phase-change memory. Applied Surface Science, 633, 157642. https://doi.org/10.1016/j.apsusc.2023.157642

Zhao, Q., Jie, W., Wang, T., Castellanos-Gomez, A., & Frisenda, R. (2020). InSe Schottky diodes based on van der Waals contacts. Advanced Functional Materials, 30(24), 2001307. https://doi.org/10.1002/adfm.202001307

Zheng, W., Liu, Z., Xi, G., Liu, T., Wang, D., Wang, L., & Liao, W. (2025). Polymorphic phases in 2D In2Se3: Fundamental properties, phase transition modulation methodologies and advanced applications. Nanoscale Horizons, 10(6), 1054–1076. https://doi.org/10.1039/d4nh00650j

Zheng, X., Han, W., Yang, K., Wong, L. W., Tsang, C. S., Lai, K. H., Zheng, F., Yang, T., Lau, S. P., Ly, T. H., Yang, M., & Zhao, J. (2022). Phase and polarization modulation in two-dimensional In2Se3 via in situ transmission electron microscopy. Science Advances, 8(42), eabo0773. https://doi.org/10.1126/sciadv.abo0773

Information about authors

Oman Zabira – al-Farabi KazNU, Almaty, Kazakhstan, PhD student of EP '8D07112 Nanomaterials and Nanotechnologies', 2D semiconducting materials and heterostructures for photoelectrochemisty and optoelectronics
E-mail: omankaznu@gmail.com
ORCID: https://orcid.org/0009-0008-0681-8475

Nurlybekov Nurken – al-Farabi KazNU, Almaty, Kazakhstan, PhD student of EP '8D07112 Nanomaterials and Nanotechnologies', Low-loss phase change chalcogenide thin films
E-mail: idcnurken@gmail.com
ORCID: https://orcid.org/0009-0006-1917-4547

Umarov Yerzhan – al-Farabi KazNU, Almaty, Kazakhstan, 4th year BS of EP '6B05305 Physics and Nanotechnology', Optical characterization of thin film semiconducting materials
E-mail: tektorarhi@gmail.com
ORCID: https://orcid.org/0009-0005-6365-9376

Zhylysbayev Ulan – al-Farabi KazNU, Almaty, Kazakhstan, MS of EP '7M07135 Materials science and engineering', Optoelectronics of 2D InSe crystals
E-mail: ulanzhylysbaev@gmail.com
ORCID: https://orcid.org/0009-0001-8892-4026

Zhakypov Alibek – al-Farabi KazNU, Almaty, Kazakhstan, PhD in Materials Science, thin film phase-change materials
E-mail: alibek.zhakypov@kaznu.edu.kz
ORCID: https://orcid.org/0000-0001-9904-318X

Nemkayeva Renata – National Nanolaboratory at al-Farabi KazNU, Almaty, Kazakhstan, MS in Physics, Spectroscopy of 2D semiconducting nanomaterials, carbon nanomaterials
E-mail: nemkayeva.renata@gmail.com
ORCID: https://orcid.org/0000-0002-8782-703X

Mukhametkarimov Yerzhan – al-Farabi KazNU, Almaty, Kazakhstan, PhD in Nanomaterials and Nanotechnologies, thin-film semiconducting materials, 2D semiconducting materials, plamonic composite materials, plasma physics
e-mail: yerzhan.mukhametkarimov@kaznu.kz
ORCID: https://orcid.org/0000-0003-1381-4532

Vol. 1, Issue 2, June 2026.

CENTRAL ASIAN TRANSACTIONS ON MATERIALS STRUCTURE AND PROPERTIES

https://doi.org/10.51885/3134-7983_CATMSP_2026_2_8
SRSTI 53.39.00

INFLUENCE OF MECHANICAL ACTIVATION AND SPARK PLASMA SINTERING ON THE STRUCTURE AND PROPERTIES OF WC-FE AND WC-NI ALLOYS

Yerkezhan Tabiyeva [1], Dias Yerbolat [1]*, Azamat Urkunbay [1], Madina Aidarova [1], Sayat Zakerov [1], Małgorzata Rutkowska-Gorczyca [2]

[1]Center of Excellence "VERITAS", D. Serikbayev East Kazakhstan Technical University, Ust-Kamenogorsk, Kazakhstan

[2]Department of Automotive Engineering, Wrocław University of Science and Technology, Wrocław, Poland

*Corresponding author: Yerbolat Dias, e-mail: dyerbolat@edu.ektu.kz

Keywords:

WC-Fe alloys, WC-Ni alloys, mechanical activation, spark plasma sintering, cobalt-free hard alloys, nanocrystalline structure, microhardness, powder metallurgy.

ABSTRACT

The influence of mechanical activation and spark plasma sintering on the structural-phase state and mechanical properties of cobalt-free $WC_{95}Fe_5$ and $WC_{95}Ni_5$ hard alloys was investigated. Powder mixtures were prepared by high-energy milling in a planetary ball mill for 30 and 60 minutes. It was found that increasing the mechanical activation time leads to a decrease in crystallite size to 23.8-32.0 nm and an increase in microstrains to 0.198-0.222%. SPS sintering at temperatures of 1300-1350 °C is accompanied by partial relaxation of the defect structure and crystallite growth. The maximum relative density values were 90% for $WC_{95}Fe_5$ and 89% for $WC_{95}Ni_5$, and microhardness values were 1320 and 1080 HV, respectively. The WC-Fe system was shown to exhibit higher mechanical properties compared to WC-Ni. The obtained results indicate the promise of combining mechanical activation and SPS for producing cobalt-free hard alloys, but require further optimization of consolidation parameters.

INTRODUCTION

Tungsten carbide (WC) based hard alloys occupy a leading position in the modern tooling industry. Their high hardness, wear resistance, and ability to maintain performance at elevated temperatures make them indispensable for the production of cutting inserts, drill bits, and die tooling (Kurlov & Gusev, 2013; Lassner & Schubert, 1999; Mukhopadhyay & Basu, 2011). Cobalt is the classic binder component, providing excellent wetting of WC grains and thus enabling the formation of a dense composite with a good combination of mechanical properties (Armstrong, 2011). However, since the 2000s, the economic and environmental drawbacks of cobalt have become increasingly evident: its market price is highly volatile, resources are limited, and the inhalation of cobalt containing dust is associated with carcinogenic risks (Chang & Chen, 2014; He & Schoenung, 2002; Yang et al., 2020).

These circumstances drive researchers to search for alternative binder metals. Iron and nickel are considered the most justified candidates to replace Co. Both elements have melting points close to that of cobalt, are chemically compatible with WC, and can form a ductile γ phase that binds the carbide grains together (Voitovich et al., 1996; Zhong et al., 2015). Iron attracts attention due to its low cost and high carbon solubility, while nickel provides enhanced corrosion resistance and ductility. The literature reports that, under appropriately selected sintering conditions, WC-Fe and WC-Ni alloys can achieve mechanical properties comparable to those of

commercial WC-Co (Cai et al., 2017; García et al., 2019; Shichalin et al., 2022). At the same time, replacing cobalt with Fe or Ni demands more precise control of the technological parameters because of somewhat poorer wetting of carbide grains and a narrower temperature range for effective densification (Uazyrkhanova et al., 2025).

Powder mixture preparation plays a significant role in improving the quality of cobalt free composites. High energy mechanical activation in planetary ball mills has long proven to be a tool that sharply increases the homogeneity and reactivity of the charge (Suryanarayana, 2001). During repeated collisions, the WC, Fe and Ni particles are severely deformed, fragmented and locally welded together. The result is a uniform distribution of the binder, a reduction of crystallite size to the nanometer range, accumulation of defects, and consequently a marked lowering of the sintering temperatures (Gao et al., 2018; Lima et al., 2024; Zhang et al., 2024).

Nevertheless, the achievements obtained at the activation stage are easily nullified by conventional sintering methods. Long holding at high temperatures inevitably triggers recrystallization and uncontrolled grain growth, which cancels out the advantages of the nanostructured state (Munir, Anselmi-Tamburini, & Ohyanagi, 2006; Tokita, 2013). An effective way to solve this problem is spark plasma sintering (SPS). In SPS, heating is achieved by passing high density pulsed current through the graphite tooling and the powder, generating Joule heat directly inside the material. This arrangement allows heating rates as high as 1000 °C/min and shortens the holding time at the maximum temperature to a few minutes (Munir et al., 2006; Shichalin et al., 2020). As a result, grain coalescence can be almost completely suppressed, and the ultrafine structure formed during mechanical activation can be preserved (Genga et al., 2013; Lima et al., 2020).

The efficiency of combining SPS with prior mechanical activation has already been demonstrated for several carbide based compositions. For WC based systems, specimens with submicron grains have been obtained at temperatures 200-300 °C lower than those required in conventional sintering. It has been shown that an almost pore free state can be achieved while keeping the crystallite size at the nanometer level (Boukantar et al., 2020; da Silva et al., 2021; Rong et al., 2012). However, for composites with a low content of iron and nickel binder, systematic data on the combined effect of mechanical activation time and SPS temperature on the final properties are lacking. This is especially true for a direct comparative analysis of the two alternative systems, WC-Fe and WC-Ni, under identical processing conditions - which constitutes the scientific novelty of the present work.

The aim of this study is to establish the regularities of structure formation and the physical-mechanical properties of WC-5 at.% Fe and WC-5 at.% Ni alloys as a function of mechanical activation time and spark plasma sintering temperature.

MATERIALS AND METHODS

Elemental powders of WC (purity > 99.9%, particle size < 30 μm), Fe (purity > 99.9%, particle size < 30 μm), and Ni (purity > 99.9%, particle size < 50 μm) were used as starting materials. The powders were supplied by Hebei Suoyi New Material Technology Co., Ltd. (Handan City, Hebei Province, China).

The morphology of the initial WC, Fe, and Ni powders is shown in Figure 1. Tungsten carbide powder exhibits angular particle shapes with distinct facets and sharp edges, which is typical for brittle ceramic materials. The particles have a relatively wide size distribution and show a slight tendency to agglomerate due to their high specific surface area. Iron powder features more rounded and smoothed particle shapes. Both individual particles and small agglomerates are observed. The particle surface is relatively flat, which is attributed to the ductility of the material and the specifics of its production. Nickel powder is characterized by predominantly rounded or slightly elongated particles with a smooth surface. The particles are distributed rather uniformly, with no pronounced agglomeration.

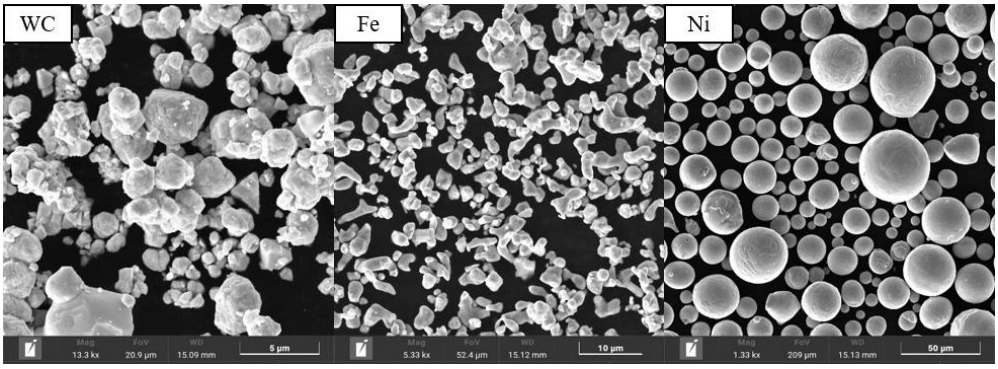

Figure 1. Initial powders

Note – compiled by the author

The initial powders with nominal compositions of $WC_{95}Fe_5$ and $WC_{95}Ni_5$ (at.%) were subjected to high-energy milling in a planetary ball mill Fritsch Pulverisette 7 premium line (Fritsch GmbH, Idar-Oberstein, Germany). Steel balls of 5 mm diameter were used as grinding media, and the volume of the milling vials was 45 mL. The ball-to-powder mass ratio was 10:1. The milling duration was 30 and 60 minutes at a rotation speed of 650 rpm, with 5-minute pauses every 10 minutes of operation to prevent local overheating inside the milling vials. To reduce agglomeration during milling, a small amount of stearic acid (2.5% of the powder mass) was added. The process was carried out in an inert argon atmosphere. The loading and unloading of powder mixtures into and from the planetary mill were performed in a vacuum glove box to prevent oxidation. Powder blending was also carried out for 10 minutes at a rotation speed of 200 rpm without the addition of stearic acid.

The powder mixtures obtained after mechanical activation were sintered by spark plasma sintering using a U-Fast Compact 40 Pro (Genicore, Poland). Sintering was carried out at temperatures of 1300 and 1350 °C under uniaxial pressure of 30 MPa. The heating rate was 100 °C/min, and the holding time at the maximum temperature was 7 min. The process was conducted in a graphite mold with a diameter of 20 mm. The mass of the powder mixture before sintering was 25 g. Sintering was performed in a vacuum atmosphere with a residual pressure of about 5×10^{-2} mbar.

Annealing of the samples was carried out in an atmosphere furnace (model SA2-4-17TP, Hefei Kejing Materials Technology Co., Ltd., China) at 500 °C with a holding time of 60 min to relieve residual stresses. The heating rate was 20 °C/min. The heat treatment was performed under vacuum. After the holding time, the samples were cooled together with the furnace and removed after complete cooling to room temperature. After heat treatment, the samples were ground to prepare the surface for subsequent studies.

Powder morphology was analyzed using a TESCAN MIRA LMS scanning electron microscope (TESCAN, Brno, Czech Republic).

The particle size of the milled powders was determined using a Fritsch Analysette 22 NEXT particle size analyzer (Fritsch GmbH, Idar-Oberstein, Germany).

The crystal structure of the milled powders was investigated using an X'Pert PRO X-ray diffractometer (Malvern Panalytical Empyrean, Almelo, The Netherlands) with a copper anode (CuKα1, λ = 1.5406 Å). The measurement range was 20-90°, the X-ray tube voltage was 40 kV, and the current was 30 mA. The scanning step was 0.02°, with a counting time of 1 s per step. A fixed divergence slit of 1/2°, a distance of 91 mm from the divergence slit to the tube focus, a fixed incident mask of 15 mm, and an anti-scatter slit of 2° were used. All measurements were carried out at a temperature of 25 °C. Diffractogram processing was performed using HighScore software (version 4.9a, 2021). Phase analysis was carried out using the PDF 5 database (2025).

The average crystallite size and microstrain were determined using the classical Williamson-Hall method, which takes into account the contribution of finite crystallite size and microstrains to the broadening of X-ray peaks. The full width at half maximum (FWHM, β) of the diffraction peaks was corrected for instrumental broadening. The Williamson-Hall equation is as follows:

$$\beta(2\theta) = k\lambda/D\cos\theta + 4\varepsilon\tan\theta \quad (1)$$

The relative density of the sintered samples was determined by the Archimedes method using hydrostatic weighing.

The microhardness of the samples was determined by the Vickers method using a DuraScan 20 (EMCO-TEST Prüfmaschinen GmbH, Austria). The tests were carried out at a load of 1 kg and a holding time of 10 s.

RESULTS AND DISCUSSION

The microstructure of $WC_{95}Fe_5$ and $WC_{95}Ni_5$ powder mixtures at various stages of mechanical activation is shown in Figures 2 and 3.

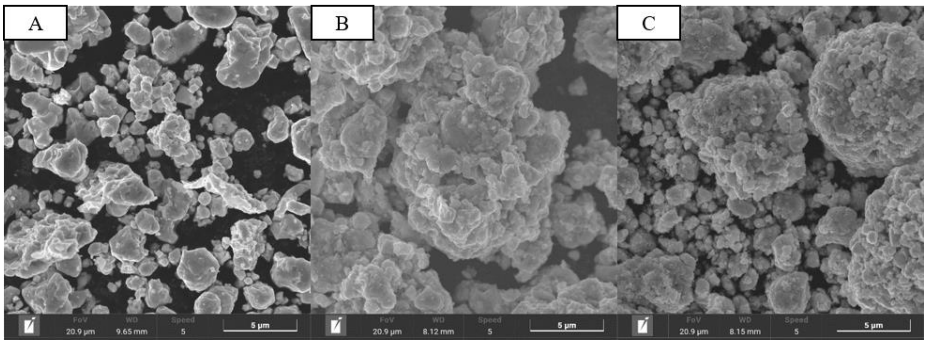

Figure 2. $WC_{95}Fe_5$ powder mixture: a) after mixing, b) after 30 min of mechanical activation, c) after 60 min of mechanical activation (magnification ×10000)

Note – compiled by the author

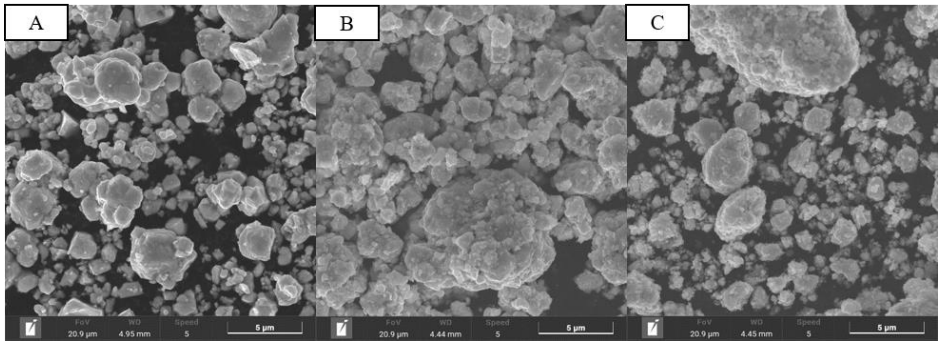

Figure 3. $WC_{95}Ni_5$ powder mixture: a) after mixing, b) after 30 min of mechanical activation, c) after 60 min of mechanical activation (magnification ×10000)

Note – compiled by the author

For both systems after the mixing stage (Figures 2a, 3a), the retention of the initial powder morphology is characteristic: angular tungsten carbide grains are uniformly distributed throughout the volume, and particles of the metallic binder (Fe or Ni) are located between them. Agglomeration is weak, and the structure is relatively homogeneous and dispersed.

After 30 minutes of mechanical activation (Figures 2b, 3b), a significant change in morphology is observed in both systems. Large, irregularly shaped agglomerates are formed due to the intensive occurrence of cold welding processes. Moreover, for the WC95Ni5 system, this effect is more pronounced, which is associated with the higher ductility of nickel compared to iron, promoting more effective particle bonding and the formation of dense conglomerates. As a result, the structure becomes inhomogeneous and characterized by a wide particle size distribution.

Upon increasing the mechanical activation duration to 60 minutes (Figures 2c, 3c), the destruction of previously formed agglomerates is observed in both systems. The particles acquire a more compact shape, the proportion of large conglomerates decreases, and the structure becomes more homogeneous. For the $WC_{95}Ni_5$ system, this process proceeds more efficiently, which is manifested in the formation of a finer structure compared to $WC_{95}Fe_5$. This indicates the transition of the mechanical activation process to the stage of dynamic equilibrium between cold welding and particle fracture.

Table 1. Average particle size of $WC_{95}Fe_5$ and $WC_{95}Ni_5$ depending on the mechanical activation time

Powder mixture	Average particle size, μm		
	as-mixed	30 min	60 min
$WC_{95}Fe_5$	2,737±0,0324	19,045±0,4830	5,817±0,4492
$WC_{95}Ni_5$	2,467±0,0301	20,699±0,1563	3,803±0,2860
Note – compiled by the author			

The observed morphological changes are consistent with the evolution of the mean particle size (Table 1). For the $WC_{95}Fe_5$ system, the mean particle size after mixing is about 2.7 μm; after 30 minutes of mechanical activation it increases to ~19.0 μm due to agglomeration; and upon increasing the time to 60 minutes it decreases to ~5.8 μm because of agglomerate disintegration. A similar trend is observed for the $WC_{95}Ni_5$ system: after mixing the mean particle size is about 2.5 μm, then it increases to ~20.7 μm after 30 minutes of mechanical activation and decreases to ~3.8 μm after 60 minutes of processing. The lower mean particle size for the $WC_{95}Ni_5$ system indicates more efficient comminution, which is consistent with the SEM analysis results.

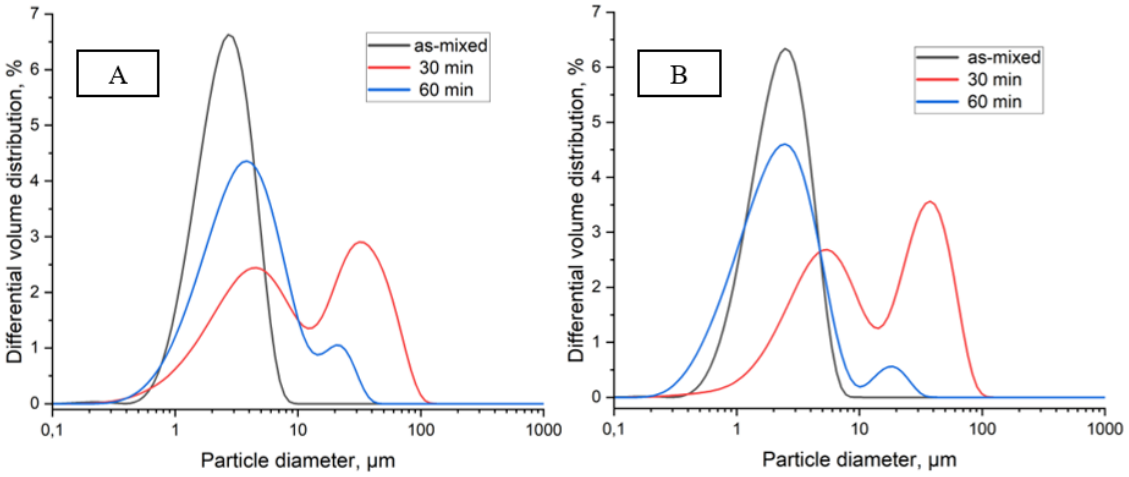

Figure 4. Particle size distribution of the (a) $WC_{95}Fe_5$ and (b) $WC_{95}Ni_5$ powder mixtures after different mechanical activation times

Note – compiled by the author

The particle size distribution analysis (Fig. 4) confirms the revealed trends. For both systems after mixing, the distributions are narrow and concentrated in the fine size range, indicating high powder homogeneity. After 30 minutes of mechanical activation, the distributions broaden substantially and shift toward larger sizes, acquiring a polymodal character, which is associated with the formation of agglomerates. Upon increasing the time to 60 minutes, the distributions narrow again and shift toward smaller sizes, indicating the disintegration of agglomerates and an improvement in structural homogeneity. Moreover, for the $WC_{95}Ni_5$ system, a narrower distribution is observed compared to $WC_{95}Fe_5$, pointing to a higher degree of powder dispersion and homogenization.

Thus, it has been established that increasing the mechanical activation duration to 60 minutes leads to the formation of a more homogeneous and fine-grained structure in both systems, while the use of nickel as a binder phase provides more efficient comminution and a narrower particle size distribution.

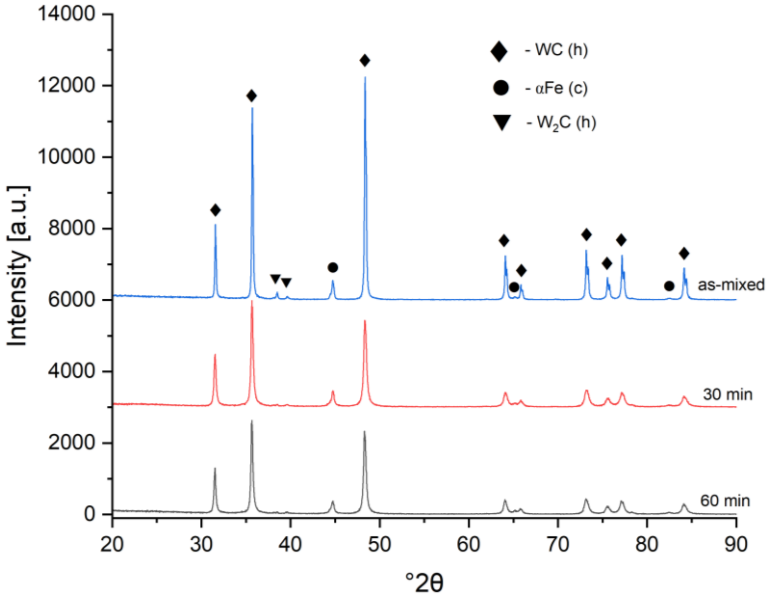

Figure 5. X-ray diffraction patterns of $WC_{95}Fe_5$ powder mixtures after different mechanical activation times

Note – compiled by the author

On the X-ray diffraction patterns of the $WC_{95}Fe_5$ powder mixture (Fig. 5) after the mixing stage, intense and narrow diffraction peaks corresponding WC, W_2C and Fe are observed, indicating a high degree of crystallinity of the initial powders. The average crystallite size is 86.8 nm, and the microstrain value is 0.052%, which points to a low level of structural defectiveness.

After 30 minutes of mechanical activation, a noticeable broadening of the diffraction peaks and a decrease in their intensity are observed. This is associated with a reduction in crystallite size to 37.8 nm and an increase in microstrains to 0.163% (Fig. 7) due to intensive plastic deformation and defect accumulation. A decrease in the intensity of the iron peaks is also noted, which may be related to its more uniform distribution within the WC matrix.

Upon increasing the mechanical activation time to 60 minutes, the peak broadening becomes more pronounced, and their intensity continues to decrease. The average crystallite size decreases to 32.0 nm, while microstrains increase to 0.198% (Fig. 7). This indicates further structural refinement and accumulation of crystal lattice defects.

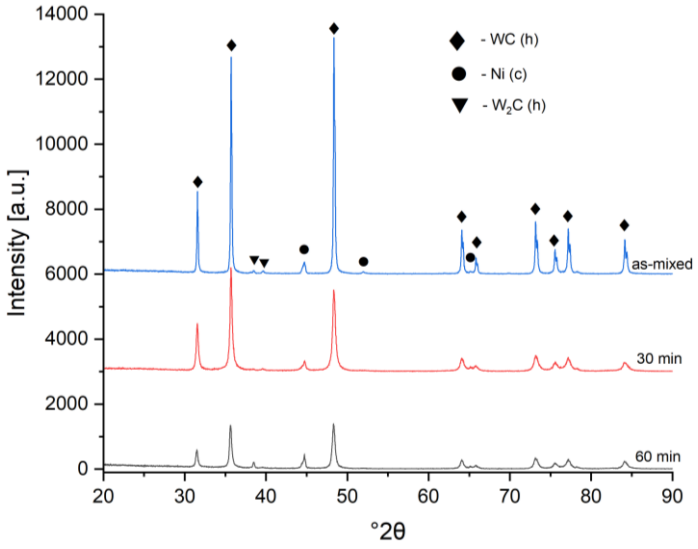

Figure 6. X-ray diffraction patterns of $WC_{95}Ni_5$ powder mixtures after different mechanical activation times

Note – compiled by the author

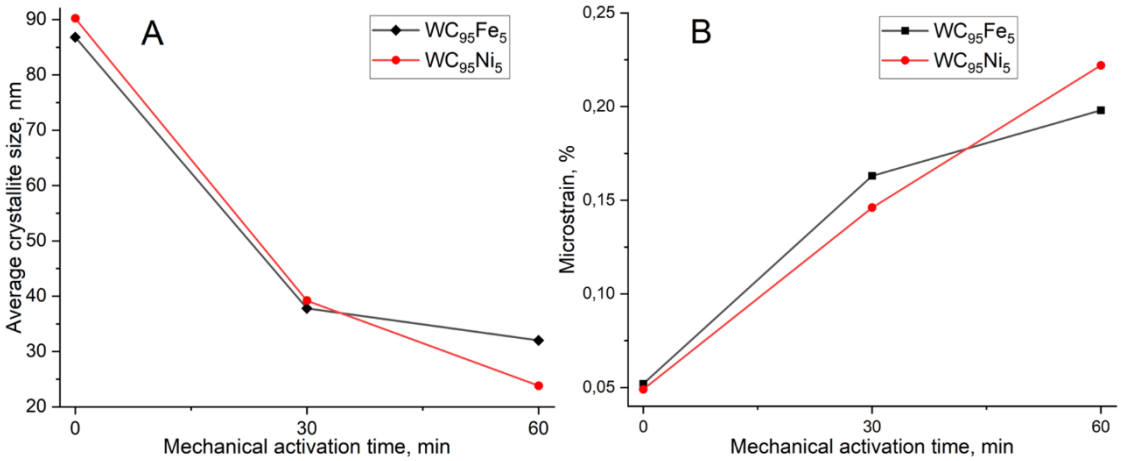

Figure 7. Average crystallite size and microstrain of $WC_{95}Fe_5$ and $WC_{95}Ni_5$ powder mixtures after different mechanical activation times: (a) average crystallite size, (b) microstrain

Note – compiled by the author

For the $WC_{95}Ni_5$ system (Fig. 6) after mixing, narrow and intense peaks of WC, W_2C and Ni, characteristic of crystalline starting powders, are also observed. The average crystallite size is 90.2 nm, and the microstrains are 0.049% (Fig. 7), corresponding to a low level of internal stresses.

After 30 minutes of mechanical activation, peak broadening and a decrease in their intensity occur, which is more pronounced compared to the $WC_{95}Fe_5$ system. The crystallite size decreases to 39.2 nm, and microstrains increase to 0.146% (Fig. 7). The more intensive structural change is due to the high ductility of nickel, which promotes defect accumulation.

After 60 minutes of mechanical activation, significant broadening of the diffraction peaks and a further decrease in their intensity are observed. The average crystallite size decreases to 23.8 nm, and microstrains increase to 0.222% (Fig. 7). This indicates more intensive structural refinement and a higher level of defectiveness compared to the $WC_{95}Fe_5$ system.

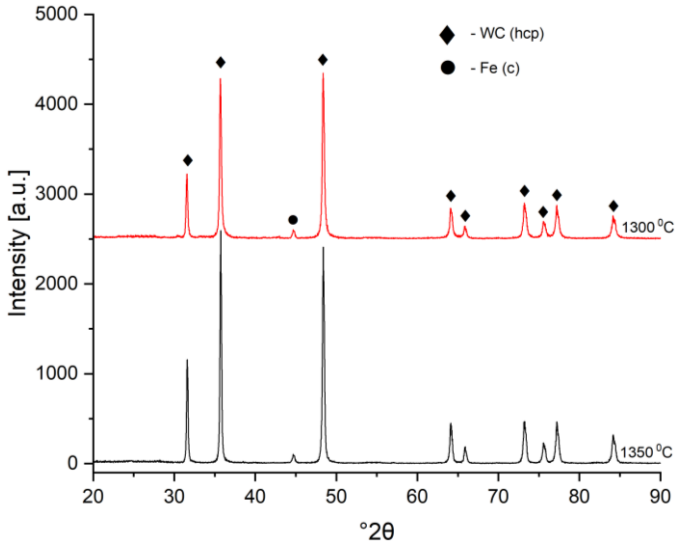

Figure 8. X-ray diffraction patterns of $WC_{95}Fe_5$ after sintering
Note – compiled by the author

In the X-ray diffraction patterns of sintered samples of the $WC_{95}Fe_5$ system (Fig. 8), characteristic peaks of hexagonal WC and the face-centered cubic Fe phase are observed. Compared to the state after mechanical activation, these peaks exhibit a noticeable narrowing and an increase in intensity. These changes indicate a partial recovery of the crystalline structure during spark plasma sintering and a reduction in the degree of structural defectiveness. As the sintering temperature increases from 1300 to 1350 °C, further narrowing of the diffraction peaks occurs, reflecting an increase in the average crystallite size from 56.8 to 67.8 nm, according to the data in Fig. 10a. Simultaneously, a decrease in the microstrain level from 0.092% to 0.079% (Fig. 10b) is observed, which is attributed to the relaxation of crystal lattice defects accumulated during mechanical activation and the reduction of internal stresses. Thus, for the $WC_{95}Fe_5$ system, an increase in sintering temperature is accompanied by pronounced recrystallization and grain growth processes, along with a decrease in structural defectiveness.

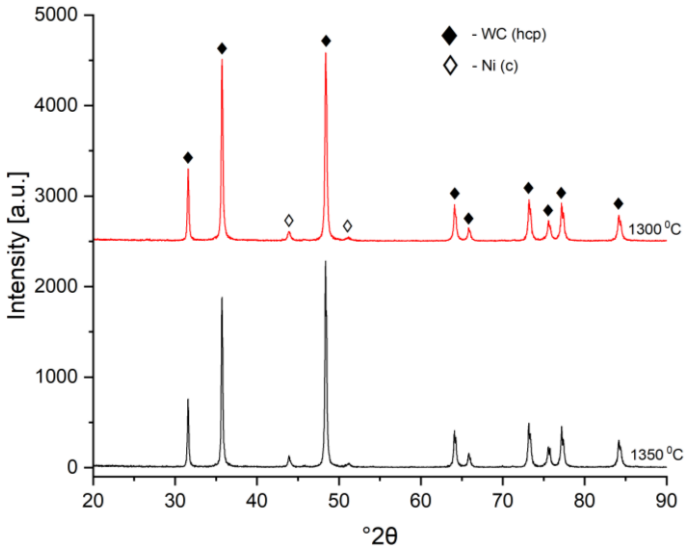

Figure 9. X-ray diffraction patterns of $WC_{95}Ni_5$ after sintering
Note – compiled by the author

For the $WC_{95}Ni_5$ system (Fig. 9), similar trends in the evolution of X-ray diffraction characteristics after sintering are observed, although their magnitude is somewhat different. The diffraction peaks of hexagonal WC and the face-centered cubic Ni phase also become narrower and more intense compared to the powder state, indicating the restoration of crystalline order. As the sintering temperature increases from 1300 to 1350 °C, the average crystallite size increases from 58.2 to 63.2 nm (Fig. 10a); however, the increase is less significant than that for the $WC_{95}Fe_5$ system. Concurrently, the microstrain level decreases from 0.089% to 0.083% (Fig. 10b), indicating partial relaxation of defects, although this process proceeds less intensively. The retention of a lower crystallite growth rate in the WC95Ni5 system may be associated with the more ductile nature of the nickel binder phase, which hinders intensive grain coalescence and promotes the retention of a more dispersed structure.

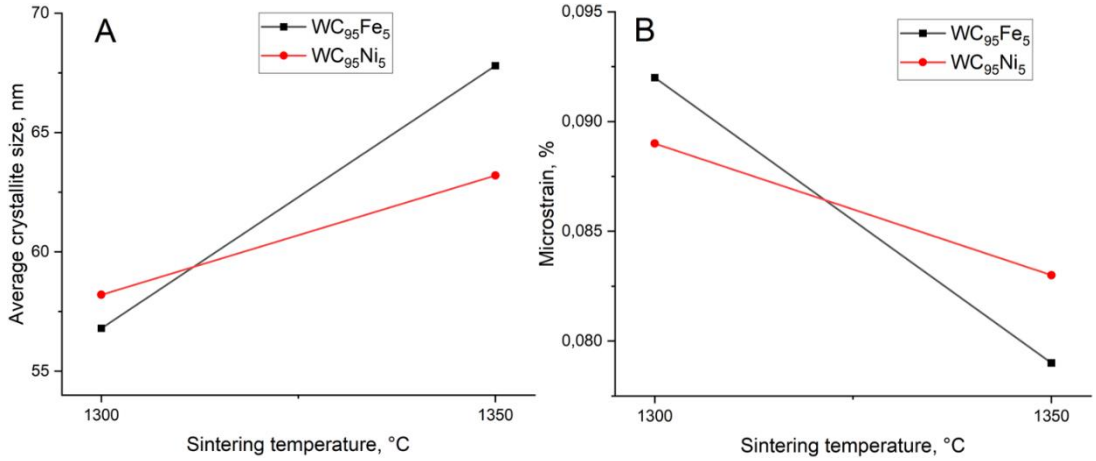

Figure 10. Average crystallite size and microstrain of sintered $WC_{95}Fe_5$ and $WC_{95}Ni_5$ samples: (a) average crystallite size, (b) microstrain

Note – compiled by the author

Table 2. Microhardness (Vickers) and relative density values of sintered $WC_{95}Fe_5$ and $WC_{95}Ni_5$ samples.

Sintering temperature	Microhardness, HV		Relative density, %	
	$WC_{95}Fe_5$	$WC_{95}Ni_5$	$WC_{95}Fe_5$	$WC_{95}Ni_5$
1300 °C	1180	950	86	85
1350 °C	1320	1080	90	89
Note – compiled by the author				

Analysis of the data presented in Table 2 reveals a correlation between the relative density and microhardness of the sintered samples. For the $WC_{95}Fe_5$ system, at a sintering temperature of 1300 °C, the relative density is 86%, while the microhardness reaches 1180 HV. Upon increasing the temperature to 1350 °C, the density increases to 90%, which is accompanied by a rise in microhardness to 1320 HV. A similar dependence is observed for the $WC_{95}Ni_5$ system: at 1300 °C, the relative density is 85% and the microhardness is 950 HV, whereas at 1350 °C, the density increases to 89% and microhardness rises to 1080 HV. These results indicate that an increase in sintering temperature leads to more effective material densification, a reduction in porosity, and consequently, an increase in microhardness. In all cases, the $WC_{95}Fe_5$ system

exhibits higher values of both density and microhardness compared to the $WC_{95}Ni_5$ system, which is attributed to the more rigid nature of the iron binder phase relative to the nickel binder.

It should be noted that the mechanical activation and spark plasma sintering parameters employed in this work are not optimal with respect to achieving maximum density. In particular, the relatively short holding time during SPS (7 min) was deliberately chosen to limit grain growth and preserve the fine-grained structure formed during the mechanical activation stage.

It is known that increasing the temperature and holding time during SPS leads to more complete material consolidation by activating diffusion processes and reducing porosity. However, such conditions are generally accompanied by coarsening of the grain structure, which may negate the advantages obtained from mechanical activation. In this regard, the implemented sintering regime can be considered a compromise between the degree of densification and the retention of a fine-grained state. The obtained values of relative density and microhardness in this case are due to the limited sintering duration and, consequently, the incomplete realization of diffusion-controlled densification processes. Further improvements in density and mechanical properties are possible by increasing the holding time, sintering temperature, or the binder phase content; however, this would likely lead to grain growth. Therefore, optimization of the SPS parameters in the studied systems requires a balance between retaining the fine-grained structure and achieving a high degree of densification.

CONCLUSIONS

It has been established that increasing the mechanical activation time to 60 minutes leads to the formation of a nanostructured state in WC-Fe and WC-Ni powder mixtures. For the system with a nickel binder, the crystallite size decreases to 23.8 nm, and microstrains reach 0.222%, whereas for WC-Fe, these values are 32.0 nm and 0.198%, respectively, with the higher ductility of nickel promoting intensive accumulation of crystal lattice defects. Spark plasma sintering at temperatures of 1300-1350 °C with a short holding time of 7 minutes allows for partial relaxation of the defective structure and preserves the fine-grained state of the materials. Increasing the sintering temperature enhances the relative density: from 86% to 90% for WC-Fe, and from 85% to 89% for WC-Ni. This is accompanied by an increase in microhardness: from 1180 to 1320 HV for WC-Fe, and from 950 to 1080 HV for WC-Ni. The WC-Fe system exhibits higher density and hardness across all regimes due to the specific behavior of the iron binder phase. The obtained density and hardness values are consistent with the selected sintering regimes, which are designed to suppress grain growth and preserve the nanostructure, and do not represent the maximum achievable values.

The scientific novelty of this research lies in demonstrating that the combination of mechanical activation for 60 minutes followed by spark plasma sintering at 1350 °C with a short holding time provides a viable compromise between densification and nanostructure retention in cobalt-free cemented carbides. The theoretical conclusion is that the more rigid iron binder phase promotes higher densification and hardness, while the more ductile nickel binder phase better suppresses grain growth, offering a guideline for binder selection based on the desired microstructure.

The practical significance is that the proposed processing route represents a promising approach for producing cobalt-free WC-Fe and WC-Ni cemented carbides with controlled nanostructure. A limitation identified is that the short holding time prevents full diffusion-controlled densification, and achieving properties comparable to cobalt-based analogues would require further optimization of consolidation parameters.

Prospects for further research include optimizing sintering temperature, holding time, or uniaxial pressure to achieve higher density and hardness while maintaining nanostructure, as well as examining wear resistance, fracture toughness, and hybrid Fe-Ni binder compositions.

CONFLICT OF INTEREST: The authors declare no conflict of interest.

FUNDING: This research is funded by the Committee of Science of the Ministry of Science and Higher Education of the Republic of Kazakhstan under the topic BR24992925 "Development of technology and materials for the innovative development of the manufacturing industry of the Republic of Kazakhstan".

INSTITUTIONAL REVIEW BOARD STATEMENT: Not applicable. This study did not involve humans or animals.

INFORMED CONSENT STATEMENT: Not applicable. This study did not involve human participants.

DATA AVAILABILITY STATEMENT: The data supporting the findings of this study are available from the corresponding author upon reasonable request.

ACKNOWLEDGEMENTS: The authors thank the anonymous reviewers for their constructive comments.

STATEMENT ON THE USE OF ARTIFICIAL INTELLIGENCE TECHNOLOGIES: The authors used artificial intelligence tools – ChatGPT (OpenAI, GPT-4o) and DeepSeek (DeepSeek-R1) - to assist with language editing, text structuring, and improving the clarity of the manuscript. All scientific content, data analysis, and conclusions were developed and verified by the authors, who take full responsibility for the integrity of the work.

REFERENCES

Kurlov, A. S., & Gusev, A. I. (2013). Tungsten Carbides and W-Co Hardmetals. Springer. https://doi.org/10.1007/978-3-319-00524-9

Lassner, E., & Schubert, W. D. (1999). Tungsten: Properties, Chemistry, Technology of the Element, Alloys, and Chemical Compounds. Springer. https://doi.org/10.1007/978-1-4615-4907-9

Mukhopadhyay, A., & Basu, B. (2011). Recent developments on WC-based bulk composites. Journal of Materials Science, 46(3), 571-589. https://doi.org/10.1007/s10853-010-5046-7

Armstrong, R. W. (2011). The Hardness and Strength Properties of WC-Co Composites. Materials, 4(7), 1287-1308. https://doi.org/10.3390/ma4071287

He, J., & Schoenung, J. M. (2002). A review on nanostructured WC-Co coatings. Surface and Coatings Technology, 157(1), 72-79. https://doi.org/10.1016/S0257-8972(02)00141-X

Yang, Y., Zhang, C., Wang, D., Nie, L., Wellmann, D., & Tian, Y. (2020). Additive manufacturing of WC-Co hardmetals: a review. The International Journal of Advanced Manufacturing Technology, 108(5-6), 1653-1673. https://doi.org/10.1007/s00170-020-05389-5

Chang, S.-H., & Chen, S.-L. (2014). Characterization and properties of sintered WC-Co and WC-Ni-Fe hard metal alloys. Journal of Alloys and Compounds, 585, 407-413. https://doi.org/10.1016/j.jallcom.2013.09.188

Voitovich, V. B., Sverdel, V. V., Voitovich, R. F., & Golovko, É. I. (1996). Oxidation of WC-Co, WC-Ni and WC-Co-Ni hard metals in the temperature range 500-800 °C. International Journal of Refractory Metals and Hard Materials, 14(4), 289-295. https://doi.org/10.1016/0263-4368(96)00009-1

Zhong, L., Xu, Y., Hojamberdiev, M., & Liu, J. (2015). Microstructural and Mechanical Properties of In Situ WC-Fe/Fe Composites. Journal of Materials Engineering and Performance, 24(11), 4561-4568. https://doi.org/10.1007/s11665-015-1742-4

Shichalin, O. O., Buravlev, I. Yu., Papynov, E. K., et al. (2022). Comparative study of WC-based hard alloys fabrication via spark plasma sintering using Co, Fe, Ni, Cr, and Ti binders. International Journal of Refractory Metals and Hard Materials, 102, 105725. https://doi.org/10.1016/j.ijrmhm.2021.105725

García, J., Collado Ciprés, V., Blomqvist, A., & Kaplan, B. (2019). Cemented carbide microstructures: a review. International Journal of Refractory Metals and Hard Materials, 80, 40-68. https://doi.org/10.1016/j.ijrmhm.2018.12.004

Cai, X., Xu, Y., Zhong, L., & Liu, M. (2017). Fracture toughness of WC-Fe cermet in W-WC-Fe composite by nanoindentation. Journal of Alloys and Compounds, 728, 788-796. https://doi.org/10.1016/j.jallcom.2017.09.070

Uazyrkhanova, G., Kozhakhmetov, Y., Aidarova, M., Rutkowska-Gorczyca, M., & Tabiyeva, Y. (2025). Combined Approach to the Synthesis of WC-(Fe, Ni) Hard Alloys: Mechanical Activation and Spark Plasma Sintering. Crystals, 15(8), 724. https://doi.org/10.3390/cryst15080724

Suryanarayana, C. (2001). Mechanical alloying and milling. Progress in Materials Science, 46(1-2), 1-184. https://doi.org/10.1016/S0079-6425(99)00010-5

Zhang, Z., et al. (2024). Effect of W-to-C atomic ratio on microstructure and properties of in-situ synthesized WC/Fe composites by spark plasma sintering. International Journal of Refractory Metals and Hard Materials, 121, 106643. https://doi.org/10.1016/j.ijrmhm.2024.106643

Gao, Y., Luo, B.-H., He, K.-J., Zhang, W.-W., & Bai, Z.-H. (2018). Effect of Fe/Ni ratio on the microstructure and properties of WC-Fe-Ni-Co cemented carbides. Ceramics International, 44(3), 3291-3296. https://doi.org/10.1016/j.ceramint.2017.10.148

Lima, M. J. S., Silva, F. E. S., Raimundo, R. A., et al. (2024). Enhanced properties of hard metal WC-Ni processed from nanostructured powders. Ceramics International, 50(22, Part B), 47445-47455. https://doi.org/10.1016/j.ceramint.2024.09.096

Zhang, Z., et al. (2017). The effect of volume fraction of WC particles on wear behavior of in-situ WC/Fe composites by spark plasma sintering. International Journal of Refractory Metals and Hard Materials, 69, 196-208. https://doi.org/10.1016/j.ijrmhm.2017.08.009

Guillon, O., et al. (2014). Field-Assisted Sintering Technology/Spark Plasma Sintering: Mechanisms, Materials, and Technology Developments. Advanced Engineering Materials, 16(7), 830-849. https://doi.org/10.1002/adem.201300409

Munir, Z. A., Anselmi-Tamburini, U., & Ohyanagi, M. (2006). The effect of electric field and pressure on the synthesis and consolidation of materials: A review of the spark plasma sintering method. Journal of Materials Science, 41(3), 763-777. https://doi.org/10.1007/s10853-006-6555-2

Tokita, M. (2013). Spark Plasma Sintering (SPS) Method, Systems, and Applications. In Handbook of Advanced Ceramics (2nd ed., pp. 1149-1177). Academic Press. https://doi.org/10.1016/B978-0-12-385469-8.00060-5

Munir, Z. A., Ohyanagi, M., Tokita, M., Khor, M., Hirai, T., & Anselmi-Tamburini, U. (Eds.). (2006). Pulse Electric Current Synthesis and Processing of Materials (Ceramic Transactions, Vol. 194). American Ceramic Society; Wiley-Interscience.

Shichalin, O. O., et al. (2020). SPS hard metal alloy WC-8Ni-8Fe fabrication based on mechanochemical synthetic tungsten carbide powder. Journal of Alloys and Compounds, 816, 152547. https://doi.org/10.1016/j.jallcom.2019.152547

Lima, M. J. S., Silva, F. E. S., Lima, H. D., Souto, M. V. M., Oliveira, A. G. F., Raimundo, R. A., Souza, C. P., & Gomes, U. U. (2020). Spark plasma sintering of nanostructured powder composites (WC-Ni) prepared by carboreduction reaction. Materials Chemistry and Physics, 254, 123439. https://doi.org/10.1016/j.matchemphys.2020.123439

Genga, R. M., Cornish, L. A., & Akdogan, G. (2013). Effect of Mo_2C additions on the properties of SPS manufactured WC-TiC-Ni cemented carbides. International Journal of Refractory Metals and Hard Materials, 41, 12-21. https://doi.org/10.1016/j.ijrmhm.2013.01.008

Rong, H., Peng, Z., Ren, X., Peng, Y., & Wang, C. (2012). Ultrafine WC-Ni cemented carbides fabricated by spark plasma sintering. Materials Science and Engineering: A, 532, 543-547. https://doi.org/10.1016/j.msea.2011.10.119

da Silva, E. N., dos Santos, A. A. A., do Nascimento, R. M., Alves, S. M., da Silva Guimarães, R., & Filgueira, M. (2021). Investigation of characteristics and properties of spark plasma sintered ultrafine WC-6.4Fe3.6Ni alloy as potential alternative WC-Co hard metals. International Journal of Refractory Metals and Hard Materials, 101, 105669. https://doi.org/10.1016/j.ijrmhm.2021.105669

Boukantar, A.-R., Djerdjare, B., Guiberteau, F., & Ortiz, A. L. (2020). Spark plasma sinterability and dry sliding-wear resistance of WC densified with Co, Co+Ni, and Co+Ni+Cr. International Journal of Refractory Metals and Hard Materials, 92, 105280. https://doi.org/10.1016/j.ijrmhm.2020.105280

Information about authors

Yerkezhan Tabiyeva – Center of Excellence "VERITAS", D. Serikbayev East Kazakhstan Technical University, Ust-Kamenogorsk, Kazakhstan. PhD in Technical Physics.
Powder metallurgy, alloys, mechanical alloying
E-mail: etabieva@edu.ektu.kz
ORCID: https://orcid.org/0000-0002-9726-7187

Dias Yerbolat – Center of Excellence "VERITAS", D. Serikbayev East Kazakhstan Technical University, Ust-Kamenogorsk, Kazakhstan
Education: PhD student at the S. Amanzholov East Kazakhstan University (EKU) Ust-Kamenogorsk, Kazakhstan 2023 - Present. M.Sc. in Technical Sciences: D. Serikbayev East Kazakhstan Technical University (EKTU) 2021 - 2023. B.Sc.in automation and management: Al-Farabi Kazakh National University Almaty, Kazakhstan 2018 - 2021.
Powder metallurgy, alloys, ceramics, composite materials, XRD, spark plasma sintering, mechanical alloying
E-mail: dyerbolat@edu.ektu.kz
ORCID: https://orcid.org/0000-0002-2072-4212

Azamat Urkunbay – Center of Excellence "VERITAS", D. Serikbayev East Kazakhstan Technical University, Ust-Kamenogorsk, Kazakhstan. M.Sc. in Physics in Technical Physics Sarsen Amanzholov East Kazakhstan University, Ust-Kamenogorsk, Kazakhstan 2025 - Present. Bachelor's degree: Graduated with a bachelor's degree from the Kazakh University of Ways and Communications, majoring in Automation and Control
Powder metallurgy, alloys, spark plasma sintering, mechanical alloying
E-mail: aurkunbay@edu.ektu.kz
ORCID: https://orcid.org/0000-0002-7868-2393

Madina Aidarova – Center of Excellence "VERITAS", D. Serikbayev East Kazakhstan Technical University, Ust-Kamenogorsk, Kazakhstan. PhD student at the East Kazakhstan Technical University named after D. Serikbaev, Ust-Kamenogorsk, Kazakhstan. 2012-2016 - Bachelor's degree in 5B072300 Technical Physics, Shakarim State University of Semey. 2016-2018 - Master's degree in 6M072300 Technical Physics, Shakarim State University of Semey. Powder metallurgy, alloys, mechanical alloying
E-mail: maidarova@edu.ektu.kz
ORCID: https://orcid.org/0009-0000-9200-8058

Sayat Zakerov – Center of Excellence "VERITAS", D. Serikbayev East Kazakhstan Technical University, Ust-Kamenogorsk, Kazakhstan. M.Sc. in Technical Physics at the D. Serikbayev East Kazakhstan Technical University (EKTU), Ust-Kamenogorsk, Kazakhstan 2024 - Present. B.Sc. in Physics D. Serikbayev East Kazakhstan Technical University (EKTU), Ust-Kamenogorsk, Kazakhstan 2020 – 2024. Powder metallurgy, alloys, spark plasma sintering, mechanical alloying
E-mail: szakerov@edu.ektu.kz
ORCID: https://orcid.org/0009-0000-9470-9018

Małgorzata Rutkowska-Gorczyca – Department of Automotive Engineering, Wrocław University of Science and Technology, Wrocław, Poland
PhD in Mechanics, Associate Professor.
Microstructure, material characterization, advanced materials, alloys
E-mail: malgorzata.rutkowska-gorczyca@pwr.edu.pl
ORCID: https://orcid.org/0000-0003-2712-5914

https://doi.org/10.51885/3134-7983_CATMSP_2026_2_9
SRSTI 31.17.29

PRODUCTION OF AGGLOMERATED COKE FROM INDUSTRIAL WASTE AND CHARACTERIZATION OF COKING PRODUCTS

Lyazat Tolymbekova [1], **Almat Aubakirov** [2], **Saule Abdulina** [3]*, **Bauyrzhan Kelamanov** [4], **Khamit Temirtas** [2]
[1]L.N. Gumilyov Eurasian National University, Astana, Kazakhstan
[2]Toraighyrov University, Pavlodar, Kazakhstan
[3]D. Serikbayev East Kazakhstan Technical University, Ust-Kamenogorsk, Kazakhstan
[4]Aktobe Regional University named after K. Zhubanov, Aktobe, Kazakhstan
*Corresponding author: Abdulina Saule Amangeldievna, e-mail: sabdulina@ektu.kz

Keywords:
coke, coal, spent anode residue, coal pitch, Fourier transform infrared (FTIR), man-made waste.

ABSTRACT
The relevance of the work is due to the need to conserve resources and involve man-made waste from the coal and aluminum industries in the production of carbonaceous materials for metallurgy. The aim of the study was to obtain agglomerated coke from the coal fines of the Ekibastuz basin and the spent anode residue of aluminum production with an assessment of its mechanical, structural and chemical properties. The study employed briquetting, coking at 1150 °C in a reducing atmosphere, chemical analysis, strength testing, and FTIR spectroscopy. It was found that the optimal composition of the charge (50% coal, 20% anode cinder and 30% coal pitch) provides compressive strength up to 3.2 MPa, impact resistance of up to 8 drops without fracture. FTIR analysis showed the formation of a predominantly aromatic carbon structure with a high degree of carbonization. The practical significance of the work lies in the possibility of using the obtained coke in sintering production, and the theoretical one is to expand the understanding of the structural transformations of carbon-containing compositions during coking.

INTRODUCTION

Currently, ferrous metallurgy is showing rapid development due to the high demand for cast iron and steel in various sectors of the economy. The main task of the industry is to provide the domestic and foreign markets with metal products of the required range, quality and volume, using the best available technologies in the implementation of the State Industrial Policy and sustainable provision of raw materials resources (Sun W. et al., 2020; He K. et al., 2020; Holappa L. 2021).

Coke is the main fuel for ferrous metallurgy. Prospects for the development of the coke industry and forecasts of coke production are directly related to the expansion of metallurgical production focused on domestic and foreign markets. The increase in the demand for coke is due to an increase in production rates, as well as an increase in the price of raw materials, which, in turn, leads to an increase in the price of coke on the world market (Babich A. et al., 2019; Persistence Market Research. Metallurgical Coke Market Size & Growth Analysis, 2031. Persist. Mark. Res. 2023).

The problem of resource conservation is highly relevant, as it is necessary to develop and implement technologies that ensure the production of products with minimal consumption of energy and material resources, rational use of mineral raw materials, and the search for alternative carbon reducing agents. Such reducing agents should meet the technological requirements of metal and alloy production while reducing production costs through the use of secondary carbon resources. In this regard, research in this area is of particular importance and requires efficient approaches to the utilization of secondary carbon resources (Kuatbay, Y. et al., 2024; Aubakirov, A. et al., 2020; Holappa, L., 2023). In Kazakhstan, the accumulation of industrial waste remains an important environmental and technological issue related to the sustainable use of mineral resources. According to national environmental statistics, the total volume of accumulated industrial waste in the country exceeds 29 billion tons, while approximately 0.8 billion tons of new waste are generated annually. The largest share is associated with mining and mineral-processing activities (about 65%), whereas manufacturing industries account for roughly 12%, and the remaining portion is formed by energy production and other industrial sectors. Coal mining and beneficiation processes generate significant amounts of coal fines, slurry materials, and carbon-containing residues, which can be considered secondary raw materials for producing carbon products. The thermochemical processing of such technogenic materials, including agglomeration followed by coking, provides opportunities for obtaining carbon materials suitable for metallurgical applications such as sintering fuel (Bureau of National Statistics of the Republic of Kazakhstan, 2023; UNECE, 2022; Aubakirov et al., 2023).

Thus, the processing of coal industry waste into coke will not only reduce the environmental burden, but also provide an additional source of valuable products for the metallurgical industry of Kazakhstan.

In this regard, the development of advanced thermal processing technologies for coal treatment is of great practical importance for producing environmentally friendly, energy-efficient coke and reducing agents for industrial use (Nurgaliyev, N., et al., 2024). The need for further improvement of these methods determined the implementation of a complex of research, experimental and experimental-industrial work on the development of scientific foundations and the development of new technological solutions in the field of heat treatment of coal, ensuring the receipt of high-quality products for technological and energy purposes.

The paper presents the results of theoretical and experimental studies aimed at determining the optimal technological parameters for producing metallurgical coke for sintering production from man-made waste, such as coal fines from coal waste from Bogatyr Coal LLP (Ekibastuz, Kazakhstan) and waste from the anode production of the electrolysis plant of Kazakhstan Electrolysis Plant JSC.

In the course of research and analysis of Ekibastuz coal, we found that about 17% of the main volume of coal produced is coal fines with a particle size of 0–3 mm, which is a by-product of crushing coal is significantly cheaper, since in conventional use such fine material requires additional preparation (briquetting/granulating), which reduces its market price. In our process, a fine grain of Ekibastuz coal (0–3 mm) is used "as is" without additional crushing, which further reduces energy costs and operating costs and facilitates dosing and granulation. Previous studies demonstrated that the addition of coal fines to the ore, coke charge is possible through the use of ignition additives in order to improve its agglomeration (Nonaka H., et al. 2023; Guo Z. et al. 2023).

Adding spent anode residue to Ekibastuz coal during coke production leads to a significant increase in the amount of carbon in the final product. Spent anode residue is a carbon-rich by-product of aluminium electrolysis and contains up to 95–98% carbon, mainly in graphitized form (Li, B., et al. 2021; Bhardwaj S. et al. 2025).

In the case of mixing with ekibastuz coal, which itself has a high ash content and relatively low carbon content (about 70–75% carbon in the form of dry ash-free basis), the addition of spent anode residue allows you to significantly improve the quality composition of the charge. For example, with the introduction of a 10% spent anode residue, the carbon content of the mixture can increase by about 2–4% in absolute terms, depending on the initial Ash of coal and the ratio of other components. With a further increase in the composition of spent anode residue, carbon growth can reach 6–10%, but at the same time, due to non-carbon waste components (oxides, fluorides, salts), there may be negative technological effects such as bond destruction, deterioration of mechanical properties and ash growth (Kai, Y. et al. 2020; Biao, K. 2022).

Purposes of adding anode residue:

1) to increase the carbon content of the charge. It is important in metallurgical processes (reduction of oxides, reduction processes) to obtain coke with a high fixed carbon content, which improves its reactivity.

2) to disposal of man-made waste. Spent anode residue is a byproduct of the aluminum industry, and its reuse can reduce the environmental burden and save resources.

3) to reduce the need for expensive primary carbon materials. Partial replacement of expensive primary carbon materials with spent anode residue reduces the cost of coke.

4) to improve heat resistance and electrical conductivity. Partially graphitized carbon improves the conductive and heat-resistant properties of coke, which can be useful in special sintering options, especially in the presence of current-conducting or induction systems.

Previous studies by the authors have already demonstrated the possibility of producing carbon materials from coal fines and spent anode residue using briquetting and subsequent heat treatment, with evaluation of the physicomechanical properties of the resulting coke products (Tolymbekova et al., 2025). These results showed that technogenic carbon-containing materials can partially replace traditional carbon raw materials in metallurgical processes. The present work continues this research direction and focuses on the structural and chemical characteristics of coke obtained from real charge compositions containing coal fines, spent anode residue, and coal pitch.

The purpose of this work is to obtain coke from man-made waste that meets the requirements for use in the sintering process with an assessment of its mechanical and structural-chemical properties. As part of this study, the main attention is paid to the structural and chemical characteristics of the coke obtained using IR-Fourier spectroscopy methods and the mechanical properties of the obtained samples.

The scientific novelty of this work lies in the FTIR analysis of coke obtained from real technogenic waste compositions containing coal fines, spent anode residue, and coal pitch.

In recent years, FTIR spectroscopy has been widely used to study the structure of carbon-containing materials, including coal, semi-coke, and coke, in order to detect chemical changes occurring in the heat treatment process. Studies have shown that this method is effective in identifying functional groups, assessing the degree of aromaticity, residual content of binders, as well as in studying the transformation of hydrocarbon structures during coking. In particular, FTIR analysis was used to determine the amount of carbonyl, hydroxyl and aromatic fragments in coal of different degrees of enrichment and to identify microstructural differences between the primary and heat-treated material. This made it possible to establish a correlation between the chemical composition and quality of the resulting coke (Mishra, S. 2023; Wang 2023; Yang L. 2025).

MATERIALS AND METHODS

Laboratory experiments on coke production were carried out in the laboratory of the Department of Metallurgy of the NJSC Toraighyrov University (Tolymbekova et al., 2025).

Table 1 and Table 2 show, respectively, the content of the components and their chemical composition.

Table 1. The composition of the components in the charge, %

Samples	The composition of the components in the charge, %		
	Ekibastuz coal	Spent anode residue	Coal pitch
1	50	10	40
2	50	20	30
3	50	30	20
4	50	40	10
Note – compiled by the authors based on their own research			

Table 2. Chemical composition of charge materials

Indicator	Ekibastuz Coal	Spent anode residue	Coal pitch
Carbon (C), %	70–75	98	92–93
Hydrogen (H), %	5.2	–	4.3–4.7
Oxygen (O), %	9.2	–	0.8–1.0
Nitrogen (N), %	1.6	–	1.7–1.8
Sulfur (S), %	0.4–1.0 (avr. 0.7)	2.0	0.3–0.5
Humidity (Wr), %	3.8–7.0 (avr. 5.4)	–	–
Ash (Ad), %	37–41 (avr. 39)	0.3–0.4	0.2–0.3
Volatile substances (Vdaf), %	24–40 (avr. 32)	–	–
Qi^r, kcal/kg	3800–4200 (avr. 4000)	–	–
Melting point of ash, °C	1490–1500	–	–
SiO_2, %	56.9–67.3 (avr. 62.1)	–	–
Al_2O_3, %	24.4–31.6 (avr. 28.0)	–	–
Fe_2O_3, %	4.4–7.26 (avr. 5.83)	–	–
CaO, %	0.68–3.29 (avr. 1.98)	–	–
MgO, %	0.19–1.26 (avr. 0.72)	–	–
TiO_2, %	1.09–1.65 (avr. 1.37)	–	–
SO_3, %	0.55–2.31 (avr. 1.43)	–	–
Density, g / cm^3	–	1.56	1.2–1.3
Softening temperature, °C	–	–	110–125
Note – compiled by the authors based on their own research			

The charge with a fraction of 0–3 mm was weighed on Techprom electronic scales, mixed with heating up to 150 °C in a laboratory mixer LS-AB-10, the duration of heating was determined by the physico-chemical properties of the binder and the mixing intensity. Heat transfer to the mixed volume provided heating of the mixture particles, melting of coal pitch particles and coating of coal particles and spent anode residue. The consistency of the mass was controlled according to technological features: the absence of fineness, a viscous, but not liquid structure, the formation of a lump of a specific shape when compressed. The mixing time was 10 minutes, and the coal pitch softened and bound the charge into a homogeneous mass. Coal pitch is characterized by a relatively high coking value and good binding properties, the resulting coke

binds the carbon graphite product into a single monolith, at the same time the mass subjected to molding acquires the necessary elasticity. The resulting mass was pressed in a hydraulic press.

The resulting coal briquettes are shown in Figure 1.

Figure 1. Coal briquettes

Note – compiled by the authors based on their own research

The strength of the briquettes was tested in accordance with GOST 24707–81, "Solid Fuel. Method for Determining the Drop Strength of Briquettes," and according to the laboratory procedures used at Toraighyrov University.

Equipment:

- Hydraulic Laboratory Press PGL–25 to determine the strength limit during compression (maximum force of 25 MPa);
- Impact test apparatus with a fall height of 2 m (Fall method);
- Techprom analytical scale (error ± 0.01 g).
- Digital Mitutoyo caliper (accuracy ± 0.02 mm) to control the geometry of the samples.

Briquettes had a diameter of 50 mm and a height of 50 mm. Before testing, the samples were conditioned for 24 h at a temperature (20 ± 2) °C and humidity no more than 60%.

Further, briquette samples were subjected to the determination of compressive strength.

The compressive strength was calculated by the formula σ (1):

$$\sigma = \frac{P}{S}, \quad (1)$$

where: P is load at sample failure, N;

S is cross-sectional area, m².

For a cylindrical briquette, the cross-sectional area was calculated as follows: $S = \pi \cdot \frac{d^2}{4}$.

The test results are presented in the table.

Also, samples of coal briquettes were subjected to the determination of impact strength. The impact strength was assessed by lowering the samples from a height of 2 m onto a steel plate. Impact resistance was expressed as the number of drops sustained before failure.

The resulting briquettes were then placed in a coking container with a split tube with a rubber nipple valve for the release of gases (Figure 2).

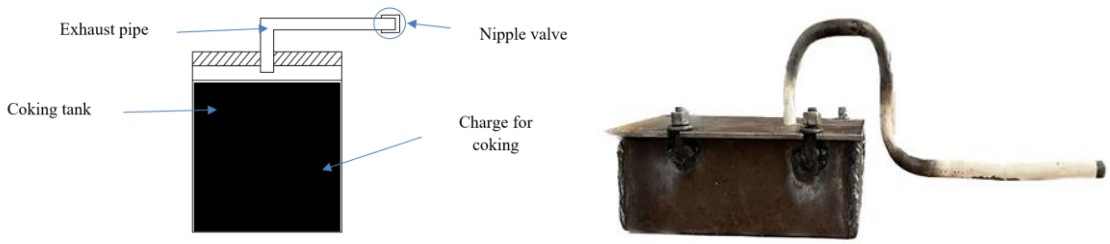

Figure 2. Laboratory coking vessel

Note – compiled by the authors based on their own research

The coking vessel was made of heat-resistant steel and is designed to operate at high temperatures in a reducing atmosphere without access to oxygen. The prepared charge batch is placed inside, the top cover is tightly fixed with bolted connections, ensuring the tightness of the volume. The lid has a fitting to which a curved metal tube is attached – an outlet line for gases and vapors formed during the coking process. At its end, a rubber nipple valve is installed, which allows volatile products to escape, but prevents air from entering the vessel.

When heated in an electric muffle furnace to the required temperature, the process of thermal decomposition of the organic components of the mixture occurs, which releases gaseous and liquid products in the container. Volatile products are discharged through the exhaust tube, and a solid carbon residue remains in the volume – coke.

This design simulates the industrial coking process on a reduced scale, ensures the stability of the heating mode, prevents the entry of oxygen and ensures the safe release of pyrolysis gases. The coking vessel was placed in a SNOL electric muffle furnace and heated according to a programmed schedule up to 1150 °C. After reaching the required temperature and subsequent cooling, the vessel was removed from the furnace.

The resulting coke has a porous structure, has sufficient strength, the average size is 3-5 mm, which meets the requirements of coke for sintering production.

Coke samples with different percentages of the resulting components were studied in detail using FTIR spectroscopy.

The FTIR method was used to analyze functional groups in the resulting coke structure. The main purpose of this analysis is to determine the degree of destruction of organic compounds and binder residues during the coking process.

Infrared spectroscopy (IR) is an analytical method that uses light from the infrared part of the spectrum to analyze a sample. Peaks in the IR spectrum represent the selective absorption of a part of the radiation that coincides in frequency with the oscillations of atoms in the molecule, that is, it corresponds to the oscillation frequencies of chemical bonds in the sample. Spectra can be recorded in transmittance or absorbance mode; in transmittance, absorption bands appear as minima, while in absorbance they appear as peaks (Al-Amin, K., Rahman, M., & others, 2024; Shimadzu Corporation, 2020)

The Shimadzu IRTracer-100 Fourier transform infrared spectrometer is designed to measure the optical spectra of full internal reflection, conduction, absorption, diffusion and mirror reflection in the infrared (IR) range; determination of the concentration of various organic and inorganic substances in solid, liquid and gaseous states (Figure 3).

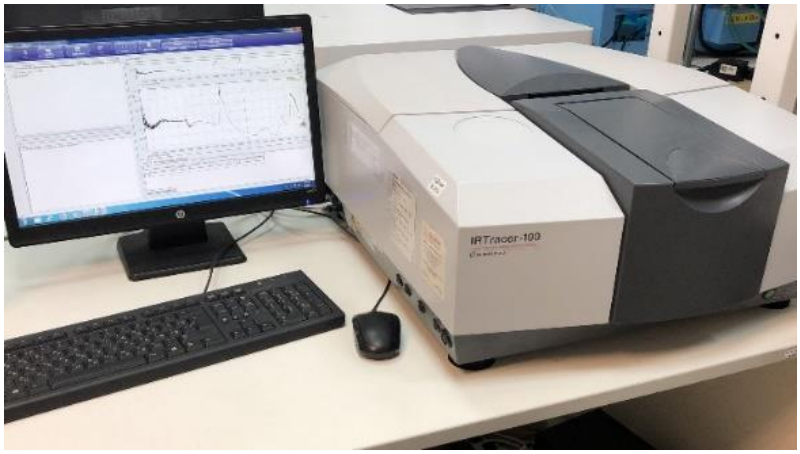

Figure 3. Shimadzu irtracer-100 Fourier spectrometer

Note – compiled by the authors based on (Shimadzu Corporation, 2020)

The principle of action of spectrophotometers is based on determining the stroke difference between the interference rays when moving mirrors in a two-beam interferometer. At the heart of the spectrophotometer is the Michelson interferometer (LibreTexts, 2023)

RESULTS AND DISCUSSION

This section presents and analyzes the results of experimental studies on the production and characterization of coke samples.

The chemical composition of the resulting coke is presented in Table 3.

Table 3. Chemical composition of coke

Carbon (C), %	Sulfur (S), %	Ash composition (Ash), %	Volatile substances, %	Humidity (Wr), %
85	0.9–1.1	19.0	1.5–2.5	≤ 1
Note – compiled by the authors based on their own research				

The resulting coke is characterized by high carbon content (85%) and low humidity (<1%), which confirms its suitability as a fuel. Despite the increased content of ash (19%) and sulfur (0.9–1.1%), this composition is suitable for use in sintering production. The increased ash and sulfur content is associated with the use of high-ash Ekibastuz coal and spent anode residue as waste from electrolysis production of aluminum (spent anode residue) containing sulfur compounds.

Table 4. Strength of compression briquettes

№ sample	Charge composition (coal : spent anode residue : coal pitch,%)	Average diameter, mm	Destructive load, N	Strength σ, MPa
1	50 : 10 : 40	50	5200	2.8
2	50 : 20 : 30	50	5700	3.2
3	50 : 30 : 20	50	5100	2.9
4	50 : 40 : 10	50	4710	2.4
Note – compiled by the authors based on their own research				

As the coal pitch content decreased, increasing the proportion of spent anode residue to 20% improved the strength of the briquettes due to the formation of a stable contact network and enhanced carbonization. However, a further increase in the spent anode residue content, accompanied by a decrease in coal pitch, reduced the strength because of insufficient binder content.

Table 5. Results of impact tests

№ sample	Composition of the charge	Number of falls before breaking	Fracture character
1	50 : 10 : 40	6	Cracks on the sides, broken edges
2	50 : 20 : 30	8	Small traces without destruction
3	50 : 30 : 20	7	Small cracks, without separation
4	50 : 40 : 10	5	Separation of the edge, division into fragments
Note – compiled by the authors based on their own research			

Briquettes containing 20% spent anode residue showed the highest impact resistance and a stable structure.

The results indicate that the optimal charge composition is 50% coal, 20% spent anode residue, and 30% coal pitch. This ratio provides sufficient plasticity, uniform particle bonding, and relatively low porosity.

The compressive strength reached 3.2 MPa, which meets the requirements for metallurgical briquettes intended for further coking.

Thus, increasing the proportion of spent anode residue to 20% was found to improve the strength of the briquettes by 15–20%.

Coal-tar pitch supplied by Kazakhstan Electrolysis Plant JSC proved to be an effective binder due to its high coke yield and suitable softening temperature.

The FTIR spectra of the coke samples prepared according to the compositions listed in Table 1 are presented below.

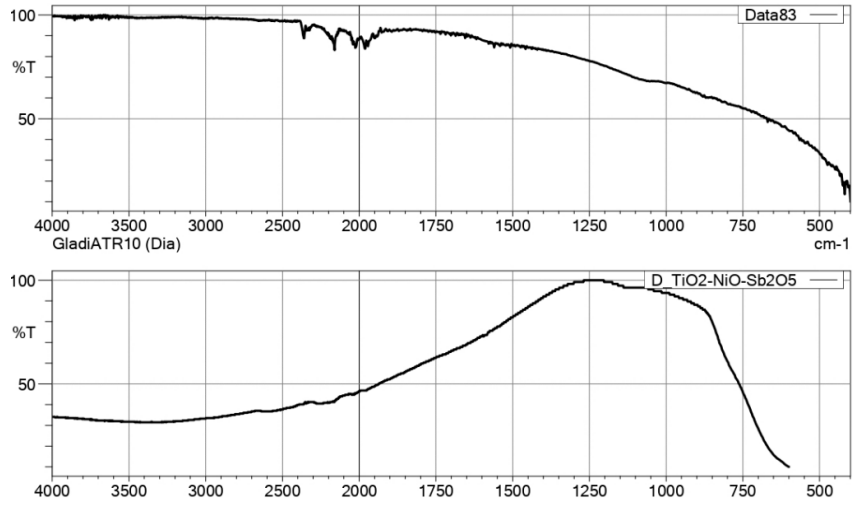

Figure 4. 1st sample

Note – compiled by the authors based on their own research

FTIR analysis of the coke spectrum of Sample 1 (Figure 4) made it possible to identify the following main functional groups:

1. Aromatic compounds (C=C, ~1600 cm^{-1}): a pronounced absorption band was observed in the region of 1580–1620 cm^{-1}, indicating the presence of aromatic carbon structures. These signals are characteristic of graphite-like structures and confirm the high degree of aromatization of the product.
2. Hydroxyl groups (O–H, 3200–3600 cm^{-1}): a broad band in the region of 3200–3600 cm^{-1} indicates the presence of hydroxyl or phenolic groups. The intensity of this band suggests the presence of residual moisture or oxygen-containing compounds after coking.
3. Carbonyl compounds (C=O, 1700–1750 cm^{-1}): the absorption peak in this region indicates the presence of carbonyl fragments, such as ketones or carboxylic acids, which may result from incomplete thermal decomposition of oxygen-containing compounds.
4. Aliphatic C–H bonds (2800–3000 cm^{-1}): weak peaks corresponding to C–H stretching vibrations in aliphatic fragments indicate a low content of volatile hydrocarbons, confirming a high degree of carbonization.
5. Ether and phenolic groups (C–O, 1050–1150 cm^{-1}): the presence of a signal corresponding to C–O vibrations indicates the presence of oxygen-containing fragments, including phenols and esters.

6. Mineral components (500–900 cm^{-1}): peaks in this region are characteristic of bending vibrations associated with metal oxides, including TiO_2, Fe_2O_3, and Al_2O_3, originating from ash components.

Sample 1 demonstrates a high degree of aromatization and a low content of volatile substances. The moderate amount of oxygen-containing functional groups indicates a sufficient level of coking. However, due to the relatively low proportion of spent anode residue, the degree of carbonization is lower than that of the other samples. Therefore, this composition can be considered acceptable, but not optimal for metallurgical applications. In addition, the increased content of ash components requires further control when the material is used in metallurgical processes.

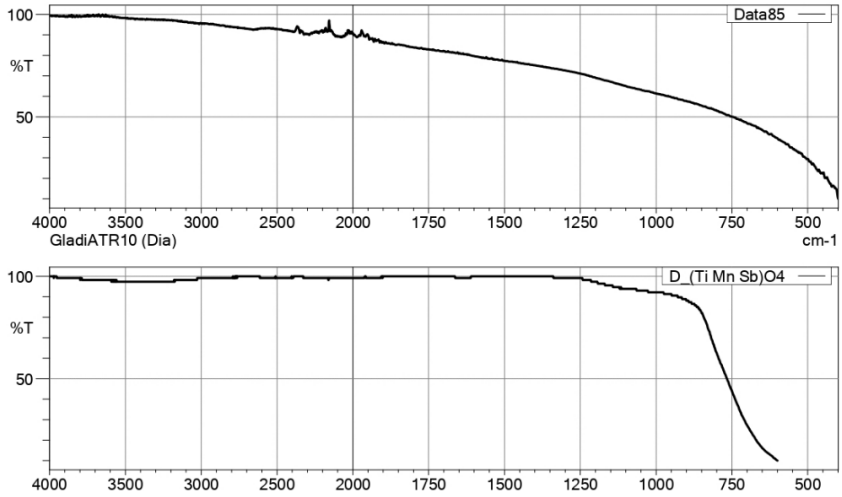

Figure 5. 2nd sample

Note – compiled by the authors based on their own research

FTIR analysis of the coke spectrum of Sample 2 revealed the following spectral features:

1. Aromatic compounds (C=C, ~1600 cm^{-1}): an intense peak in this region indicates the presence of aromatic carbon structures, confirming a high degree of aromatization.

2. Hydroxyl groups (O–H, 3200–3600 cm^{-1}): a broad high-intensity band indicates the presence of hydroxyl or phenolic groups, which may be associated with residual moisture or incomplete decomposition of oxygen-containing compounds.

3. Carbonyl compounds (C=O, 1700–1750 cm^{-1}): compared with Sample 1, a more pronounced band in this region indicates the presence of carbonyl compounds, such as quinones or residual acids, which may be associated with the oxidation of residual organic fragments.

4. Aliphatic C–H bonds (2800–3000 cm^{-1}): very weak peaks confirm a high degree of carbonization and the decomposition of volatile compounds during heat treatment.

5. Ether and phenolic groups (C–O, 1050–1150 cm^{-1}): peaks in this range are more intense than those observed in Sample 1, which may indicate a higher proportion of residual resinous substances due to the increased content of spent anode residue.

6. Mineral components (500–900 cm^{-1}): more pronounced peaks indicate the presence of metal oxides, including Fe_2O_3 and TiO_2.

Sample 2 demonstrates a high degree of aromatization and carbonization while retaining a moderate amount of functional groups that contribute to structural integrity. Although oxygen-containing compounds and ash components may adversely affect coke quality, the balance between graphitization and structural bonding makes this sample promising for further application.

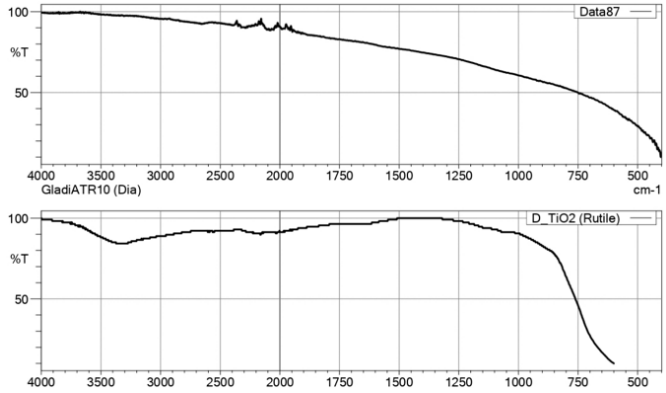

Figure 6. 3rd sample

Note – compiled by the authors based on their own research

FTIR analysis of the coke spectrum of Sample 3 revealed the following main functional groups:

1. Aromatic compounds (C=C, ~1600 cm^{-1}): an intense absorption band was observed in the range of 1580–1620 cm^{-1}, indicating the presence of aromatic structures characteristic of graphitized carbon. This confirms a high degree of aromatic structure formation.
2. Hydroxyl groups (O–H, 3200–3600 cm^{-1}): a broad absorption band in this region indicates the presence of hydroxyl or phenolic groups. This may be associated with residual moisture and the partial decomposition of oxygen-containing compounds during the coking process.
3. Carbonyl compounds (C=O, 1700–1750 cm^{-1}): the presence of carbonyl groups, such as ketones or carboxylic acids, is confirmed by an intense peak in this region, which may indicate residual organic fragments and oxidative transformations.
4. Aliphatic C–H bonds (2800–3000 cm^{-1}): weak bands corresponding to C–H stretching vibrations indicate a small amount of aliphatic fragments, confirming an advanced stage of carbonization.
5. Ether and phenolic groups (C–O, 1050–1150 cm^{-1}): the presence of a C–O signal indicates residual oxygen-containing compounds.
6. Mineral components (500–900 cm^{-1}): peaks in this range are associated with spent anode residue and ash compounds characteristic of Ekibastuz coal, including Fe_2O_3, TiO_2, CaO, and Al_2O_3.

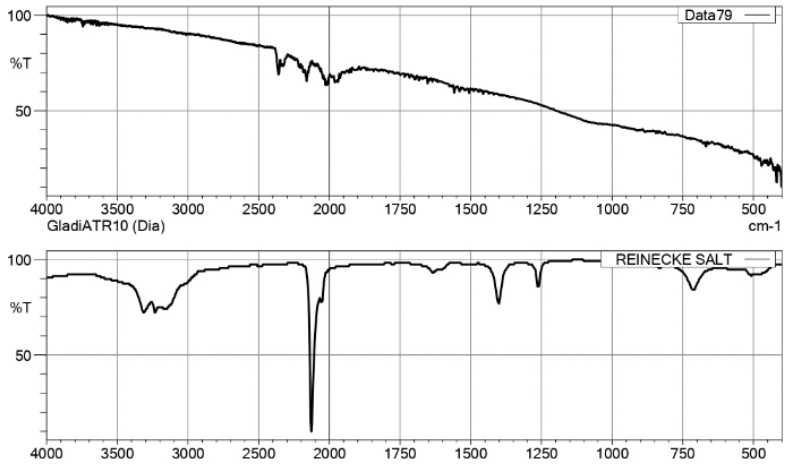

Figure 7. 4th sample

Note – compiled by the authors based on their own research

Sample 3 is characterized by a pronounced aromatic structure, good thermal stability, and a relatively high degree of carbonization. However, the reduced coal pitch content may limit the structural stability of the coke compared with Sample 2.

FTIR analysis of the coke spectrum of Sample 4 revealed the following characteristic features:

1. Aromatic compounds (C=C, ~1600 cm^{-1}): the intense absorption band indicates the presence of aromatic carbon structures, including graphite-like structures, confirming a high degree of carbonization.

2. Hydroxyl groups (O–H, 3200–3600 cm^{-1}): a broad absorption band in this region indicates the presence of hydroxyl and/or phenolic groups, as well as residual moisture associated with the spent anode residue.

3. Carbonyl compounds (C=O, 1700–1750 cm^{-1}): a distinct peak in this region indicates the presence of carbonyl compounds, possibly quinones or oxidation products.

4. Aliphatic C–H bonds (2800–3000 cm^{-1}): weakly defined peaks indicate the partial preservation of aliphatic structures, possibly originating from coal pitch.

5. Ether and phenolic groups (C–O, 1050–1150 cm^{-1}): the intensity of the bands in this range confirms the presence of oxygen-containing functional groups, such as esters and phenols.

6. Mineral components (500–900 cm^{-1}): the spectrum shows distinct peaks characteristic of metal oxides, including Fe_2O_3, TiO_2, and Al_2O_3, which indicates a relatively high content of ash impurities.

Sample 4 is characterized by a high degree of aromatization, as well as an increased amount of oxygen-containing groups. This may affect the reactivity of coke and deteriorate its mechanical properties, thereby reducing its technological suitability for sintering production.

Comparative analysis based on FTIR spectroscopy showed that all samples contained the main functional groups characteristic of carbon-containing and oxygen-containing compounds: aromatic C=C bonds (~1600 cm^{-1}), alkyl C–H bonds (~2850–2950 cm^{-1}), hydroxyl O–H groups (~3200–3600 cm^{-1}), carbonyl C=O groups (~1700 cm^{-1}), as well as ether and phenolic C–O and C–O–C groups (~1000–1300 cm^{-1}). The intensity of the bands associated with aliphatic groups generally decreased as the proportion of spent anode residue increased and the coal pitch content decreased, whereas the intensity of oxygen-containing groups varied depending on the ash content and residue composition.

This indicates a high degree of carbonization and the formation of graphite-like structures in coke with an increased proportion of spent anode residue in the charge, especially in Sample 4. In addition, samples with a lower coal pitch content showed a decrease in the functional groups involved in the formation of bonds between carbon fragments, which may reduce the mechanical strength of the resulting coke.

Samples 2 and 3, containing 50% Ekibastuz coal, 20–30% spent anode residue, and 20–30% coal pitch, showed an optimal balance between the high degree of carbonization required for the formation of a strong carbon structure and the preservation of a sufficient amount of oxygen-containing functional groups. Therefore, these samples can be considered promising compositions for metallurgical applications.

Despite its maximum degree of carbonization, Sample 4, containing 40% spent anode residue and 10% coal pitch, showed signs of excessive destruction of binding functional groups. This may lead to a decrease in coke strength during handling, transportation, and use in sintering production.

Thus, Samples 2 and 3 can be considered the most promising compositions. However, Sample 2 demonstrated the best balance between carbonization and mechanical strength. Based on the results obtained, these samples can be recommended for further investigation regarding their application in sintering production.

Comparison with industrial sintering coke

A comparative analysis of the obtained coke and typical industrial sintering coke was carried out to assess the suitability of the developed material for sintering production (Table 6).

The obtained coke demonstrates physicochemical characteristics generally comparable to those of industrial sintering coke. The carbon and sulfur contents fall within the typical ranges reported for industrial applications, whereas the ash content remains relatively high due to the use of high-ash Ekibastuz coal. Nevertheless, the obtained mechanical strength and degree of carbonization indicate the potential suitability of the produced coke for use in sintering production.

Table 6. Comparison of the obtained coke properties with typical industrial sintering coke characteristics

Parameter	Obtained coke	Industrial sintering coke*
Carbon content, %	85	80–90
Ash content, %	19	10–18
Sulfur content, %	0.9–1.1	0.5–1.2
Compressive strength, MPa	3.2	comparable range
Note – compiled by the authors based on Babich and Senk (2019), Wang et al. (2023), and own experimental data		

*Typical values according to published data for industrial sintering coke.

CONCLUSION

The study demonstrated the feasibility of producing sintering coke from technogenic waste generated by the coal and aluminum industries without relying on scarce primary carbon resources. The use of Ekibastuz Basin coal fines with a particle size of 0–3 mm without additional crushing made it possible to reduce energy consumption and improve the resource efficiency of the process. The introduction of high-carbon spent anode residue with a carbon content of 98% increased the carbon content of the charge and promoted carbonization during coking.

The optimal charge composition was 50% coal, 20% spent anode residue, and 30% coal pitch. For this composition, the compressive strength of the briquettes reached 3.2 MPa, and the impact resistance was up to 8 drop cycles without failure, which meets the requirements for carbon materials intended for sintering production. With a simultaneous decrease in coal pitch content, increasing the proportion of spent anode residue above 30% led to a deterioration in mechanical properties due to insufficient binder content and disruption of structural bonding.

Chemical analysis of the obtained coke showed a carbon content of 85%, an ash content of about 19%, and a sulfur content of 0.9–1.1%, which are acceptable for use in the sintering process, taking into account the initial ash content of Ekibastuz coal. FTIR spectroscopy revealed the predominance of aromatic carbon structures and a decrease in the intensity of aliphatic and oxygen-containing functional groups with an increase in the proportion of spent anode residue, indicating a high degree of carbonization and the formation of graphite-like structures in the material.

Thus, the results obtained confirm the feasibility of involving spent anode residue and coal fines in the technology for producing sintering coke. The proposed approach provides a simultaneous solution to the tasks of resource conservation, technogenic waste utilization, and production of a carbon material with the required mechanical, structural, and chemical characteristics for use in metallurgical production.

CONFLICT OF INTEREST: The authors declare no conflict of interest.

FUNDING: This article was prepared within the framework of the project of grant funding for scientific research of the Ministry of Science and higher education of the Republic of Kazakhstan on the topic AP19679492 "Research and development of technology for obtaining metallurgical coke for sintering production from anode production waste and coal briquettes".

INSTITUTIONAL REVIEW BOARD STATEMENT: Not applicable. This study did not involve human participants, animals, or any procedures requiring approval by an Institutional Review Board or equivalent ethics committee.

INFORMED CONSENT STATEMENT: Not applicable. This study did not involve human participants; therefore, informed consent was not required.

DATA AVAILABILITY STATEMENT: The data supporting the findings of this study are available from the corresponding author upon reasonable request.

ACKNOWLEDGEMENTS: The authors express their gratitude to the laboratory of the Department of Metallurgy of the NJSC Toraighyrov University for providing the experimental base, technical support and valuable assistance in research work.

STATEMENT ON THE USE OF ARTIFICIAL INTELLIGENCE TECHNOLOGIES: Artificial intelligence tools were used only for language editing and text improvement. All scientific analysis, interpretation of results, and conclusions were performed by the authors.

REFERENCES

Sun, W., Wang, Q., Zhou, Y., & Wu, J. (2020). Material and energy flows of the iron and steel industry: Status quo, challenges and perspectives. Applied Energy, 268, 114946. https://doi.org/10.1016/j.apenergy.2020.114946

He, K., Wang, L., & Li, X. (2020). Review of the energy consumption and production structure of China's steel industry: Current situation and future development. Metals, 10(3), 302. https://doi.org/10.3390/met10030302

Holappa, L. (2021). Challenges and prospects of steelmaking towards the year 2050. Metals, 11(12), 1978. https://doi.org/10.3390/met11121978

Babich, A., & Senk, D. (2019). Coke in the iron and steel industry. In S. Suárez-Ruiz (Ed.), New trends in coal conversion: Combustion, gasification, emissions, and coking (pp. 367–404). Woodhead Publishing. https://doi.org/10.1016/B978-0-08-102201-6.00013-3

Persistence Market Research. (2023). Metallurgical coke market size & growth analysis, 2031. Retrieved December 10, 2025, from https://www.persistencemarketresearch.com/market-research/metallurgical-coke-market.asp

Kuatbay, Y., Kelamanov, B., Aitkenov, N., & Uakhitova, B. (2024). Thermodynamic and experimental studies on the influence of high-ash coal in the production of high-carbon ferrochrome. Acta Metallurgica Slovaca, 30, 178–182. https://doi.org/10.36547/ams.30.4.2088

Aubakirov, A., Kaliakparov, A., & Tolymbekova, L. (2023). Determination of the quality of special coke as a result of heat treatment of coal from the Shubarkolskoye field. Complex Use of Mineral Resources, 327, 96–106. https://doi.org/10.31643/2023/6445.33

Bureau of National Statistics of the Republic of Kazakhstan. (2023). Environmental statistics of Kazakhstan. Retrieved December 10, 2025, from https://stat.gov.kz

United Nations Economic Commission for Europe. (2022). Environmental performance reviews: Kazakhstan. Retrieved December 10, 2025, from https://unece.org/environmental-policy/environmental-performance-reviews/kazakhstan

Nurgaliyev, N., Kolpek, A., Iskakova, S., Glazyrin, R., Safarov, Zh., & Aibuldinov, Y. (2024). Low-temperature pyrolysis of coal with determination of physicochemical properties of coal and its thermal decomposition products. E3S Web of Conferences, 545, 03004. https://doi.org/10.1051/e3sconf/202454503004

Nonaka, H., et al. (2023). Preparation of formed coke for blast furnace using kraft lignin as a binder. ISIJ International, 63(9), 1515–1525. https://doi.org/10.2355/isijinternational.ISIJINT-2023-046

Guo, Z., et al. (2023). Clean preparation of formed coke from semi-coke by the hot briquetting method. ACS Omega, 8(26), 23504–23515. https://doi.org/10.1021/acsomega.3c02519

Li, B., et al. (2021). Advances in the safe disposal and comprehensive utilization of spent carbon anode from aluminum electrolysis: Prospects for extraction and application of carbon resources from hazardous waste. Frontiers in Energy Research, 9, 779476. https://doi.org/10.3389/fenrg.2021.779476

Bhardwaj, S., & Daniel, B. S. S. (2025). Green initiatives in aluminium production: Implementing sustainable processes and effective waste management. Journal of Material Cycles and Waste Management, 27(5), 3100–3120. https://doi.org/10.1007/s10163-025-02310-8

Tolymbekova, L. B., et al. (2025). Sustainable production of metallurgical coke from technogenic wastes: A circular approach to waste utilization. International Journal of Innovative Research and Scientific Studies, 8(4), 2763–2776. https://doi.org/10.53894/ijirss.v8i4.8554

Tolymbekova, L. B., et al. (2025). Optimization of charge composition for coke production with spent anode material and evaluation of agglomerate properties. International Journal of Innovative Research and Scientific Studies, 8(6), 2491–2501. https://doi.org/10.53894/ijirss.v8i6.10131

Kai, Y., et al. (2020). Purifying spent carbon anode (SCA) from aluminum reduction industry by alkali fusion method to apply for Li-ion batteries anodes: From waste to resource. Journal of the Taiwan Institute of Chemical Engineers, 116, 121–127. https://doi.org/10.1016/j.jtice.2020.10.034

Al-Amin, K., Rahman, M., et al. (2024). Fourier transform infrared spectroscopic technique for functional group analysis of carbon materials. Applied Spectroscopy Reviews. https://pmc.ncbi.nlm.nih.gov/articles/PMC12426772/

Shimadzu Corporation. (2020). IRTracer-100 Fourier transform infrared spectrophotometer. https://www.shimadzu.com/an/products/molecular-spectroscopy/ftir/ftir-spectroscopy/irtracer-100/index.html

LibreTexts. (2023). How an FTIR spectrometer operates. Chemistry LibreTexts. https://chem.libretexts.org/Bookshelves/Physical_and_Theoretical_Chemistry_Textbook_Maps/Supplemental_Modules_%28Physical_and_Theoretical_Chemistry%29/Spectroscopy/Vibrational_Spectroscopy/Infrared_Spectroscopy/How_an_FTIR_Spectrometer_Operates

Biao, K., & Fengxia, Z. (2022). Co-treatment of spent carbon anode and copper slag for reuse and the solidification of the constituent fluorine and heavy metals. Journal of Cleaner Production, 135418. https://doi.org/10.1016/j.jclepro.2022.135418

Mishra, S., Prasad, A. K., Shukla, A., Vinod, A., Preety, K., & Varma, A. K. (2023). Estimation of carbon content in high-ash coal using mid-infrared Fourier-transform infrared spectroscopy. Minerals, 13(7), 938. https://doi.org/10.3390/min13070938

Wang, X., He, X., & Wang, X. (2023). FTIR analysis of the functional group composition of coal tar residue extracts and extractive residues. Applied Sciences, 13(8), 5162. https://doi.org/10.3390/app13085162

Yang, L., & Yuan, Y. (2025). Functional group characteristics of coal treated with clean biomass surfactant via FTIR spectroscopy. Scientific Reports, 15(1), 18676. https://doi.org/10.1038/s41598-025-03769-z

Information about authors

Tolymbekova Lyazat Baigabylovna – L.N. Gumilyov Eurasian National University, Astana, Kazakhstan, Candidate of Technical Sciences, Metallurgy, metallurgical processes, ferroalloy production, recycling of technogenic waste, coke production, agglomeration technologies.
E-mail: tolymbekova_lb@enu.kz
ORCID: https://orcid.org/0000-0002-3785-7943

Aubakirov Almat Mukanovich – Toraighyrov University, Pavlodar, Kazakhstan, PhD, Senior Lecturer, Metallurgy, carbon materials, coke production, agglomeration processes, industrial waste utilization.
E-mail: almataubakirovpsu@gmail.com
ORCID: https://orcid.org/0000-0003-3775-655X

Abdulina Saule Amangeldyevna – East Kazakhstan Technical University named after D. Serikbaev, Ust-Kamenogorsk, Kazakhstan, PhD, Professor, Materials science, metallurgy, resource-saving technologies, industrial waste processing, carbon-containing materials.
E-mail: abdulina.saule@mail.ru
ORCID: https://orcid.org/0000-0001-6328-8652

Kelamanov Bauyrzhan Satybaldyuly – Aktobe Regional University named after K. Zhubanov, Aktobe, Kazakhstan, Candidate of Technical Sciences, Professor, Metallurgy, mineral processing, technogenic raw materials utilization, industrial ecology.
E-mail: bkelamanov@zhubanov.edu.kz
ORCID: https://orcid.org/0000-0001-7646-9153

Temirtas Khamit Baurzhanuly – Toraighyrov University, Pavlodar, Kazakhstan, Master of Technical Sciences, Metallurgy, coke production, thermal processing of raw materials, carbon-containing materials.
E-mail: xamit1797@gmail.com
ORCID: https://orcid.org/0000-0002-6580-2085

CONTENT

CENTRAL ASIAN TRANSACTIONS
ON MATERIALS STRUCTURE AND PROPERTIES

Scientific journal
Published since 2026
Registered with the Ministry of Culture and Information
of the Republic of Kazakhstan.
Certificate No. KZ93VPY00129402 dated September 16, 2025.

Editors O. Nikolaenko, S. Mamyrazdykova
Copy editors O. Nikolaenko, S. Mamyrazdykova
Head of the editorial and publishing center O. Nikolaenko

Text Layout, lead out production of the original layout S. Mamyrazdykova

Signed to print on June 30, 2026.
Format 84´108/16. Offset paper.
Volume: conventional printing plate 12.81, estimated printing plate 12,85.
Printed version. Circulation 30 copies. Order No. 140-2026.
The price is negotiable.

D. Serikbayev East Kazakhstan Technical University.
070004, Ust-Kamenogorsk, 69 Protozanov Street.